

**Investigation into the Reaction Mechanism
of Molecular Cluster Batteries
by XAFS, NMR, and Magnetic Analysis**

**XAFS、NMR、磁気測定による分子クラスター電池の
反応機構解明**

WANG Heng

王 恒

Department of Chemistry, Graduate School of Science

Nagoya University

2011

Contents

Chapter 1 General introduction.....	1
1.1. Rechargeable batteries.....	1
1.2. Cathode materials for rechargeable lithium ion and lithium batteries.....	3
1.2.1. Lithium metal oxide materials.....	3
1.2.2. Organic cathode materials.....	5
1.3. Molecular cluster batteries.....	7
1.3.1. Molecular clusters.....	8
1.3.2. Mn ₁₂ molecular cluster batteries.....	13
1.4. Methodology to elucidate the battery reaction.....	16
1.4.1. Solid-state NMR.....	17
1.4.2. XAFS.....	18
1.4.3. STM-EELS.....	20
1.5. Scope of this thesis.....	21
References.....	21
Chapter 2 <i>In situ</i> XAFS studies of MCBs.....	27
2.1. Introduction.....	27
2.2. Experimental section.....	30
2.2.1. Materials.....	30
2.2.2. Battery cells for <i>in situ</i> XAFS measurements.....	32
2.2.3. Battery analyses of MCBs.....	32
2.2.4. XAFS measurements.....	32
2.2.5. XAFS data analyses.....	34
2.3. <i>In situ</i> XAFS studies of Mn ₁₂ MCBs.....	35
2.3.1. Charging/discharging curves of Mn ₁₂ MCBs.....	35
2.3.2. <i>In situ</i> XANES analyses.....	36
2.3.3. <i>In situ</i> EXAFS analyses.....	40

2.3.4. Internal redox processes of Mn12 clusters in MCBs.....	42
2.3.5. Conclusions.....	43
2.4. <i>In situ</i> XAFS studies of PMo12 MCBs.....	44
2.4.1. Charging/discharging curves of PMo12 MCBs.....	44
2.4.2. <i>In situ</i> XANES analyses.....	45
2.4.3. <i>In situ</i> EXAFS analyses.....	48
2.4.4. Model structure of the reduced PMo12.....	52
2.4.5. Electron sponge behavior of PMo12.....	54
2.4.6. Conclusions.....	58
2.5. Summary.....	58
References.....	59

Chapter 3 Electrical double layer effect of Mn12 MCBs studied by

cyclic voltammetry and solid-state ⁷Li NMR.....62

3.1. Introduction.....	62
3.2. CV measurements of Mn12 MCBs.....	64
3.2.1. Experimental.....	64
3.2.2. Results and discussion.....	64
3.3. Solid-state ⁷ Li NMR measurements of Mn12 MCBs.....	68
3.3.1. Experimental.....	68
3.3.2. Results and discussion.....	68
3.4. Discussions on the EDL formation in Mn12 MCBs.....	74
References.....	75

Chapter 4 *In situ* magnetic studies of Mn12 MCBs.....78

4.1. Introduction.....	78
4.2. Experimental.....	79
4.2.1. Battery cells for <i>in situ</i> magnetic measurements.....	79

4.2.2. <i>In situ</i> magnetic measurements.....	79
4.3. Results and discussion.....	81
4.4. Conclusions.....	85
References.....	86
Chapter 5 Conclusions and perspectives.....	88
Acknowledgements.....	91

Chapter 1

General introduction

1.1. Rechargeable batteries

Since the first battery *Galvanic cell* was invented two centuries ago, a variety of electrochemical redox couples have been proposed to build rechargeable batteries.^[1] However, only a few kinds of rechargeable batteries, namely lead-acid, nickel-cadmium (Ni-Cd) and nickel-metal hydride (Ni-MH), and so on, continue to be used (Fig. 1.1).^[2-4] The performance of these rechargeable batteries approaches close to their theoretical limit.^[5] In order to meet the demand for high efficiency rechargeable batteries for portable electric devices such as mobile phones, laptops and digital cameras, and for power electric instruments such as hybrid electric vehicles, solar- and wind- energy storage, more advanced rechargeable batteries are required.^[6]

Lithium ion batteries have been the most popular secondary batteries, since they were proposed and commercialized by Sony Corporation in the early 1990s.^[8] The configuration of a conventional Li-ion battery is illustrated in Fig. 1.2. These rechargeable Li-ion batteries typically comprise a carbon/graphite negative electrode (anode), an organic electrolyte, and a layered lithium transition-metal oxide such as

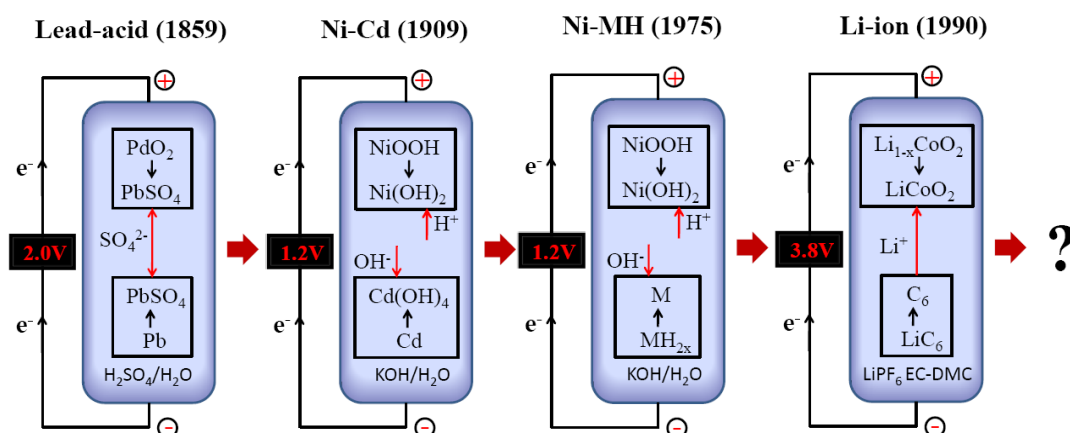


Figure 1.1 Development of the rechargeable battery technologies. The values in red indicate their battery voltage.

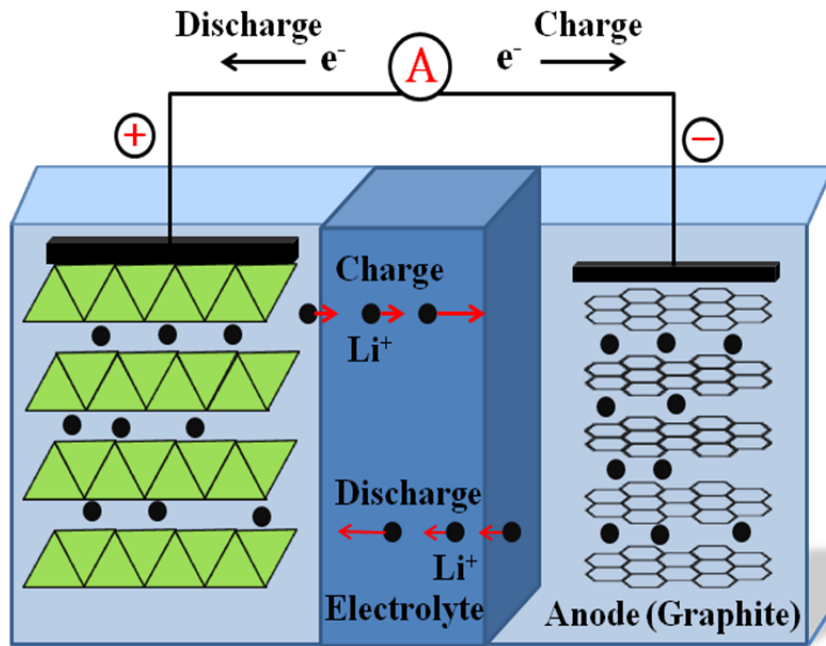


Figure 1.2 Schematic operating principle of rechargeable Li-ion battery.

LiCoO₂ positive electrode (cathode). Upon charging, Li⁺ ions are deintercalated from the layered cathode host, pass through the electrolyte, and inserted into the graphite layers in the anode. During discharging, this process is reversed. During the battery reaction, the electrons pass through the external circuit. The Li-ion battery is based on the rocking chair type intercalation reactions of Li ions between the cathode and anode materials.^[9-11]

Rechargeable Li-ion batteries provide the highest energy density in the present battery technology due to the fact that lithium is the most electropositive (-3.04 V versus standard hydrogen electrode), as well as the lightest metal. However, their charging/discharging rate is slow, because the charging/discharging process includes deintercalation/intercalation of Li⁺ ions from/into the layered cathode-active materials. In addition, cobalt is toxic, and a limited resource, and thus much effort has been devoted to developing low-cost, and environmentally friendly alternatives to the present Li-ion batteries, which realize both high energy density and rapid charging/discharging. Usually, lithium batteries, in which the anode is lithium metal and the other components are the same as Li-ion batteries, are also examined to develop the cathode materials, because the cathode performance can be directly

evaluated, independent of the anode. When synthesizing new electrode materials, two basic questions should be addressed: (1) To what extent can we design and synthesize a new electrode material with a desired property? (2) What is the knowledge of chemistry that would guide the scientist to synthesize a new electrode material with a high performance?

1.2. Cathode materials for rechargeable lithium ion and lithium batteries

The cathode is probably the most important component of Li-ion or Li batteries, which mainly determines their performance.^[12] This electrode stores Li⁺ ions by the simultaneous reduction of the active materials in it. Their desired properties are high and reversible storage capacity for Li⁺ to obtain a large capacity per unit of weight or volume, a long battery life time, and rapid solid-state Li⁺ and electron transport for high rate capability.

1.2.1. Lithium metal oxide materials

Lithium transition-metal oxides are the most matured cathode materials for Li-ion batteries. They can be classified into three major groups: (a) layered materials LiMO₂ (M: Co, Mn, Ni, and their combinations), (b) spinel structural materials LiM₂O₄ (M: Mn, Ni, Ti, and their combinations), (c) olivine structural materials LiFePO₄ (Fig. 1.3).^[13, 14]

Lithium cobalt dioxide (LiCoO₂) is the most famous layered cathode material. Its crystal structure can be described as a regular stacking of CoO₂ layers in which the Co³⁺ cations are sandwiched between two oxygen layers in CoO₆ octahedra. Li⁺ ions are also sandwiched between two CoO₂ layers, and occupy octahedral sites. Owing to the weak ionic bonds between Li⁺ and O²⁻, and to the strong covalency of the Co³⁺ and O²⁻ bonding, Li⁺ ions can diffuse quickly into the two dimensional CoO₂ interlayer, whereas Co³⁺ remains immobile. The charge compensation mechanism can be described as follows:



If $x = 1$, at which Li⁺ ions are completely deintercalated from LiCoO₂, the

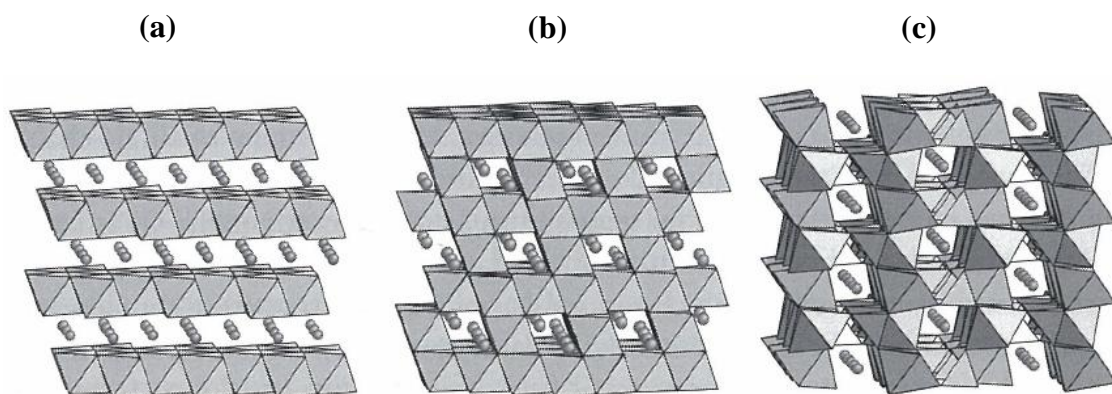


Figure 1.3 The crystal structure of (a) α -NaFeO₂ type layer structure, (b) spinel structure LiMn₂O₄, and (c) olivine structure LiFePO₄. (from Ref. 14)

theoretical capacity is 274 Ah/kg. However, when x exceeds 0.5, the CoO₂ layer breaks down, hence the practical capacity is limited to 140 Ah/kg, that is about a half of the theoretical capacity.^[15, 16] This performance can be improved by doping with trivalent ions (e.g., Al³⁺ or Cr³⁺), due to the suppression of cobalt dissolution in the electrolyte.^[17-20] However, the recognized disadvantages of cobalt, such as high toxicity, high price, and limited abundance, have led to extensive efforts to search for substitutes for this element. Mn, Ni and Fe are attractive alternatives to fully or partially replace Co, because they are much cheaper and safer, and in addition they can produce a higher practical capacity (160 Ah/kg).^[21, 22]

The spinel LiMn₂O₄, and its doped variants, have attracted much attention due to their advantages, such as safety and high charge/discharge rate capability. These properties arise from the chemical stability in the redox reaction of Mn³⁺/Mn⁴⁺, and a three dimensional passage for Li⁺ ions in this material. As such, they are being established as the cathode materials for electric vehicles. Their major drawback is the gradual capacity fading, which is caused by dissolution of Mn ions into the electrolyte.^[23] Much research effort has been focused on increasing their capacity retention by doping Li⁺ ions into the octahedral sites to form Li-rich spinel compounds, and by preparing nanostructured particles.^[23-25]

LiFePO₄, with the olivine structure, is another attractive cathode material, and is regarded as one of the most promising candidates for power tools and hybrid electric

vehicles.^[26-28] The advantages of this compound include its low cost, the low toxicity of iron, relatively high capacity (170 Ah/kg), and high capacity retention. The practical application of LiFePO_4 is mainly hampered by its low electric conductivity and slow lithium diffusion speed.^[26, 29-31]

1.2.2. Organic cathode materials

The metal oxides electrodes of the current Li-ion batteries are made from finite quantity of ores, and both the obtaining of mineral resources, and manufacturing the electrodes consumes large amounts of energy. Additionally, the charge/discharge rate is low in the current Li-ion batteries because of the low diffusion speed of Li^+ ions in the transition metal frameworks. It cannot meet the requirement of new applications, such as electric vehicles, and power backup which need a high energy density, and a fast charging/discharging. Hence, materials with high Li^+ diffusion speed produced from sustainable resources are desirable for new applications.

Organic materials have been developed as promising alternatives to metal oxides for sustainable Li-ion and Li batteries, due to their reversible redox reactions, light weight, environmental friendliness, and processability.^[32, 33] Moreover, organic chemistry offers vast opportunities to synthesize organic electrode materials with the desired structure and electrochemical properties.

Organic radical batteries using an organic nitroxyl radical polymer PTMA (poly (2,2,6,6-tetramethylpiperidinyloxy methacrylate) radical), a p-type redox active radical polymer, as cathode active material, was initially proposed by the NEC Corporation in 2004.^[34, 35] The reaction mechanism of the PTMA cathode is shown in Fig. 1.4. During the battery reaction, a one electron redox reaction occurs in the PTMA polymers which have unpaired electrons. Because of the high reactivity, and reversibility of the radical reaction, and the easy penetration/removal of Li^+ into/from polymers, this organic radical battery exhibits a fast charge/discharge rate (charge up to 80% within 1 minute) , and an extraordinarily long cycle life (over several thousand cycles).

In order to develop totally organic-based batteries, Nishide and his colleagues explored a phenoxyl polymer bearing a robust galvinoxyl radical, an n-type redox

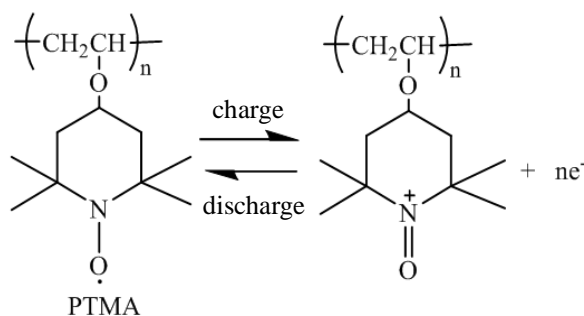


Figure 1.4 Redox process of PTMA.

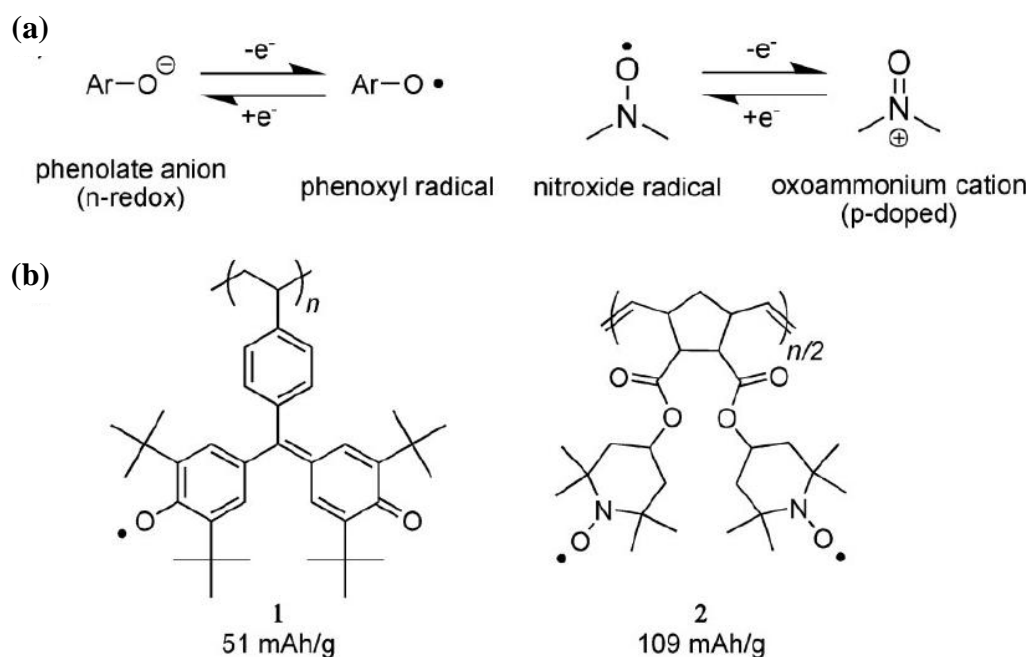


Figure 1.5 (a) Redox reactions of phenoxyl and nitroxide radicals. (b) Radical polymers and their theoretical redox capacities. (from Ref. 37)

active radical polymer, for an anode active material (Fig. 1.5).^[36] The cycle performance of the phenoxyl radical polymer batteries with a Li-metal counter electrode displayed no significant deterioration after 100 cycles (less than 5%). This is related to the fact that the battery reaction is a simple one-electron transfer from the galvinoxyl radical, and that there is no structural change in the amorphous polymer structure during redox cycling. This means that the phenoxyl radical polymer can serve as a Li^+ -ion containing electrode. Finally, they constructed an all organic battery, in which phenoxyl (n-type) and nitroxide (p-type) radicals were used as anode and cathode (Fig. 1.5).^[37-39] This all organic battery exhibited an excellent high rate

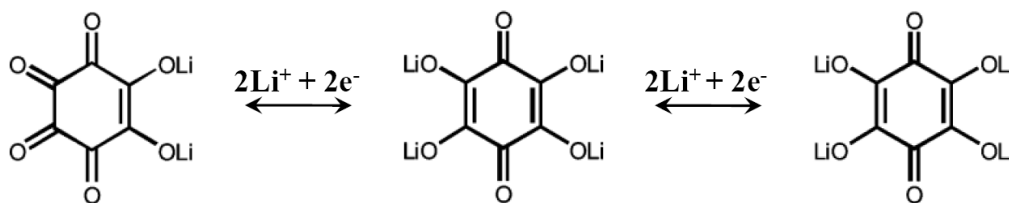


Figure 1.6 Reaction mechanism of $\text{Li}_4\text{C}_6\text{O}_6$ electrode.

capability that allows rapid charging within 10 seconds, with a large charge current. This capability can be ascribed to the rapid redox reaction of the radicals, and the efficient charge diffusion within the polymer layers. However, the typical capacity of the organic radical batteries is 110 Ah/kg, which is less than that of LiCoO_2 (148 Ah/kg), because the radical moiety, with a molecular weight of ca. 200, can store only one or two electrons in the redox reaction.

Recently, a tetralithium salt of tetrahydroxybenzoquinone ($\text{Li}_4\text{C}_6\text{O}_6$), which can be both reduced to $\text{Li}_2\text{C}_6\text{O}_6$, and oxidized to $\text{Li}_6\text{C}_6\text{O}_6$, have attracted much attention (Fig. 1.6).^[40] This salt shows a good rechargeable battery performance, with a reversible experimental capacity of about 200 Ah/kg (2Li^+ ions per molecule).^[41] In addition, this material can be directly synthesized from natural resources (e.g., sugar) in water, and be used to build all organic Li-ion batteries. However, the operating voltage (ca. 2V vs. lithium) of this battery is quite low for practical application. In order to improve upon this, it is necessary to tune the oxidation and reduction potential values by chemical substitutions.

Because of their advantages over the conventional cathode materials, organic materials are expected to be applied in the next generation of rechargeable batteries. However, we cannot neglect the disadvantages of organic materials in terms of limited thermal stability, appreciable solubility in electrolytes, and low capacity.

1.3. Molecular cluster batteries

In order to achieve both high capacity and fast charging/discharging rate, our group has recently suggested molecular clusters, which undergo multi-step redox reactions at room temperature, as possible alternative cathode active materials. These

molecular cluster batteries (MCBs) exhibit an excellent charging/discharging performance.

1.3.1. Molecular clusters

The molecular clusters are the individual molecules which are formed by a limited number of interacting metal ions centers and coordinated organic ligands. They are attracting much attention in several research areas, such as molecular chemistry, magnetism and catalysis.

Employment of the appropriate ligands and reaction conditions allowed us to synthesize a variety of high nuclearity clusters, with interesting structural, spectroscopic, electrochemical and magnetic properties. Among them, most of the metal ion centers possess unpaired electrons. The combination of the high-spin property, and large magnetic anisotropy of easy axis type, produces single-molecule magnets (SMMs), which exhibit a slow magnetization relaxation at low temperatures, to function as nanoscale magnets. Most of the SMMs have been found in transition metal chemistry, such as Mn₉, Mn₁₆, Mn₂₀, Mn₈₄, Fe₆, Fe₉, Fe₂₂, and Ni₅ (Fig. 1.7).^[42-49]

Besides the intrinsic magnetic properties, these clusters also exhibit multi-step redox reactions, in which the redox potentials are controllable by means of chemical modifications.^[50] This electrochemically active property can be harnessed for cathode

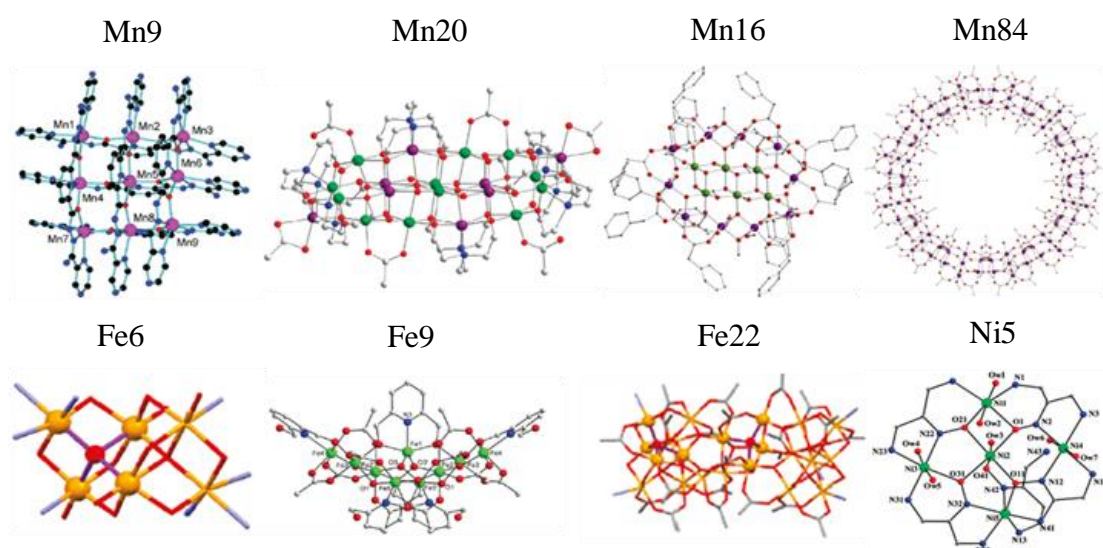


Figure 1.7 The structure of Mn₉, Mn₂₀, Mn₁₆, Mn₈₄, Fe₆, Fe₉, Fe₂₂, Ni₅. (from Ref. 42-49)

active materials in rechargeable batteries. Here, two kinds of molecular clusters, Mn12 and POMs, used in the thesis works, are explained.

Twelve nuclei manganese clusters

High nuclearity manganese carboxylate clusters have attracted much attention as one of the most promising nanoscale magnets, because of their unique structural and electronic properties.^[51, 52] The single molecule magnet Mn12-acetate (referred to as Mn12Ac) $[\text{Mn}_{12}\text{O}_{12}(\text{CH}_3\text{COO})_{16}(\text{H}_2\text{O})_4]$ was firstly synthesized by T. Lis in 1980, using a one-pot reaction of $\text{Mn}(\text{CH}_3\text{COO})_{16} \cdot 2\text{H}_2\text{O}$ and KMnO_4 in acetic acid.^[53] Since 1990, this molecule has been extensively studied as an SMM due to its ease of preparation, stability, and ease of modification in a variety of ways.^[54] Figure 1.8 shows a schematic view of the molecular structure of an Mn12 cluster. The core structure is composed of an inner cubane structure of four Mn^{4+} ions, and an external ring which consists of eight Mn^{3+} ions and eight O^{2-} ions. This core part is ligated to sixteen carboxylate groups and four H_2O ligands that isolate the Mn ions from outside.^[55] The Mn12 derivatives can be synthesized by several methods. Among them, carboxylate substitution is the most useful and convenient. Stirring Mn12Ac and an excess amount of carboxylic acid (RCOOH) in organic solvents generates an exchange reaction between CH_3CO_2^- and RCO_2^- . This method provides benefits such as isotopic labeling, tunable redox potential, and stability in a variety of organic solvents.

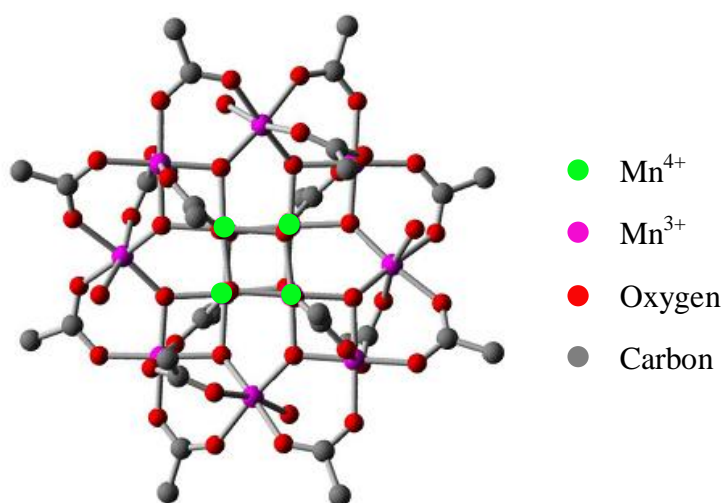


Figure 1.8 Schematic view of Mn12Ac cluster structure.

The Mn12 molecule possesses a large ground-state spin of $S = [8 \times 2 - 4 \times (3/2)] = 10$, because of strong antiferromagnetic interaction between eight Mn^{3+} ($3d^4$, $S = 2$) ions and four Mn^{4+} ($3d^3$, $S = 3/2$) ions in the molecule. This molecule also exhibits a strong uniaxial magnetic anisotropy along the molecular axis, which is caused by the Jahn-Teller distortions at the Mn^{3+} sites. The combination of the high spin and the uniaxial magnetic anisotropy results in an effective potential barrier between the up and down spin states. At low temperatures, the rotation of the high spin magnetic moment is frozen due to this intramolecular potential barrier, and the magnetic relaxation becomes very slow.

Quantum tunneling of the magnetization (QTM), which is observed as a characteristic hysteresis loop in the magnetization curve, is the most remarkable phenomenon found in the Mn12 clusters (Fig. 1.9).^[56] When the magnetic easy axis of Mn12 is oriented along the external field, the magnetization curves exhibit small steps appearing with an nearly constant interval. This feature has been rationalized as the thermally activated resonance tunneling of magnetization because QTM occurs effectively in the thermally excited states.^[56-58]

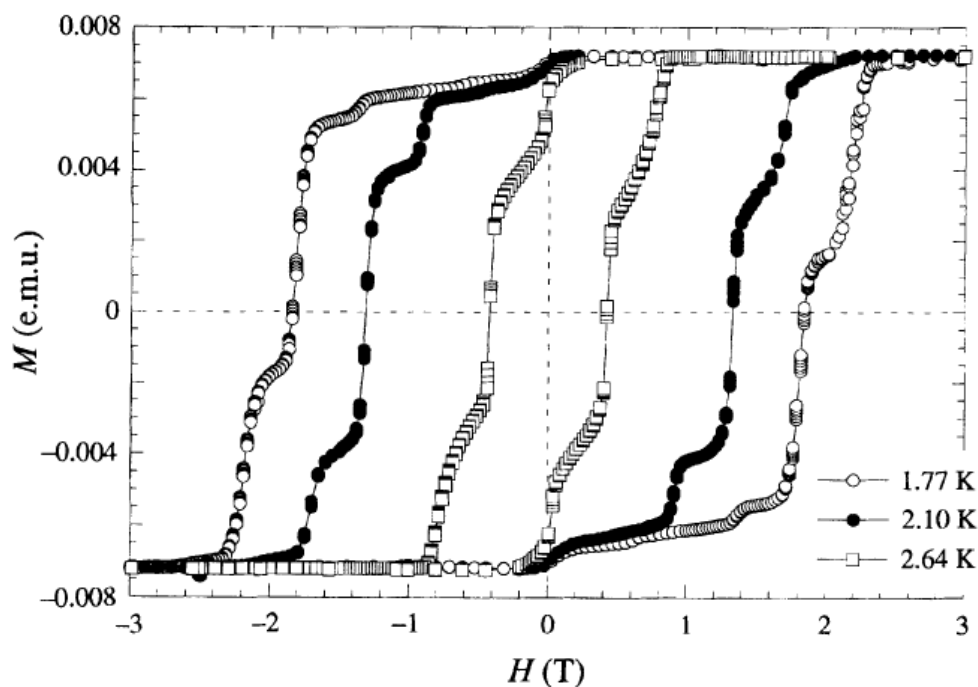
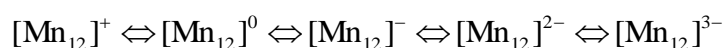


Figure 1.9 Hysteresis loops measured on the single crystal of Mn12Ac in the field parallel to the easy axis at 1.77K, 2.10K and 2.64K. (from Ref. 56)

This molecule also exhibits another interesting aspect besides its magnetic properties. The electrochemical studies of Mn12Ac clusters show stepwise reversible reduction and oxidation processes (Fig. 1.10).^[55] There are several apparent redox couples; the oxidation process at 0.82 V and the first reduction process at 0.19 V appear to be reversible by electrochemical criteria such as CV peak separations and DPV peak sharpness.

The electrochemical processes can be summarized as:



The electrochemical analysis shows that Mn12 is capable of adopting a number of stable oxidation levels and it is possible to change the properties by tuning the oxidation state. Additionally, Mn12Ac is insoluble in common organic electrolytes, in

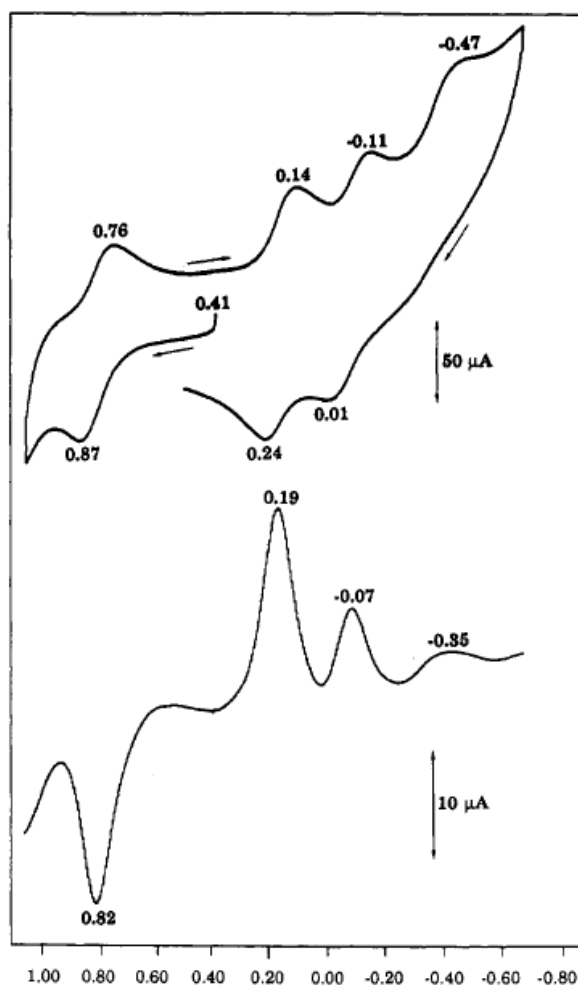


Figure 1.10 Cyclic voltammogram (top) and differential pulse voltammogram (bottom) of $[\text{Mn}_{12}\text{O}_{12}(\text{O}_2\text{CMe})_{16}(\text{H}_2\text{O})_4] \cdot 2\text{MeCOOH} \cdot 4\text{H}_2\text{O}$ in MeCN. (from Ref. 55)

which it is also stable. Thus, Mn12 could serve as a good candidate for cathode active materials for rechargeable batteries.

Polyoxometalate clusters

Polyoxometalate (POM) clusters are considered as molecular metal oxide anions from both structural and electronic points of view; they are formed by a limited number of metal centers (typically six to eighteen W or Mo ions) coordinated by bridging oxygen atoms, with enormous structural varieties. Among various types of POMs, the Keggin anions $[XM_{12}O_{40}]^{n-}$ and the Wells-Dawson (W-D) anions $[X_2M_{18}O_{62}]^{m-}$, where M= W or Mo and X= P, Si or S (Fig. 1.11), have been extensively studied in the research fields of luminescence, catalysis, magnetism, and many others.^[59, 60]

The Keggin acids are widely used as homogeneous and heterogeneous acids, and oxidation catalysts because of their stability, and extensively alterable molecular properties. These POMs can catalyze a variety of reactions in the homogeneous liquid phase, offering strong possibilities for more efficient and cleaner processing, compared to conventional mineral acids. Especially in organic media, the activity of the Keggin acids is often higher than H_2SO_4 by two or three orders of magnitude.^[62]

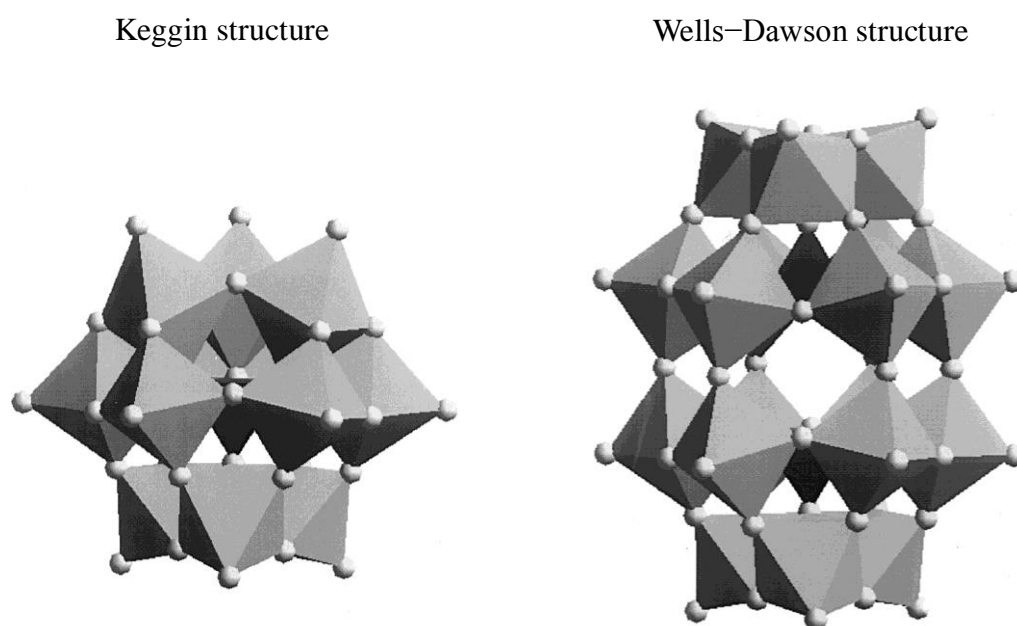


Figure 1.11 The Schematic views of two typical heteropoly anions: Keggin structure anion $[XM_{12}O_{40}]^{n-}$ and Wells-Dawson structure anion $[X_2M_{18}O_{62}]^{m-}$. (from Ref. 61)

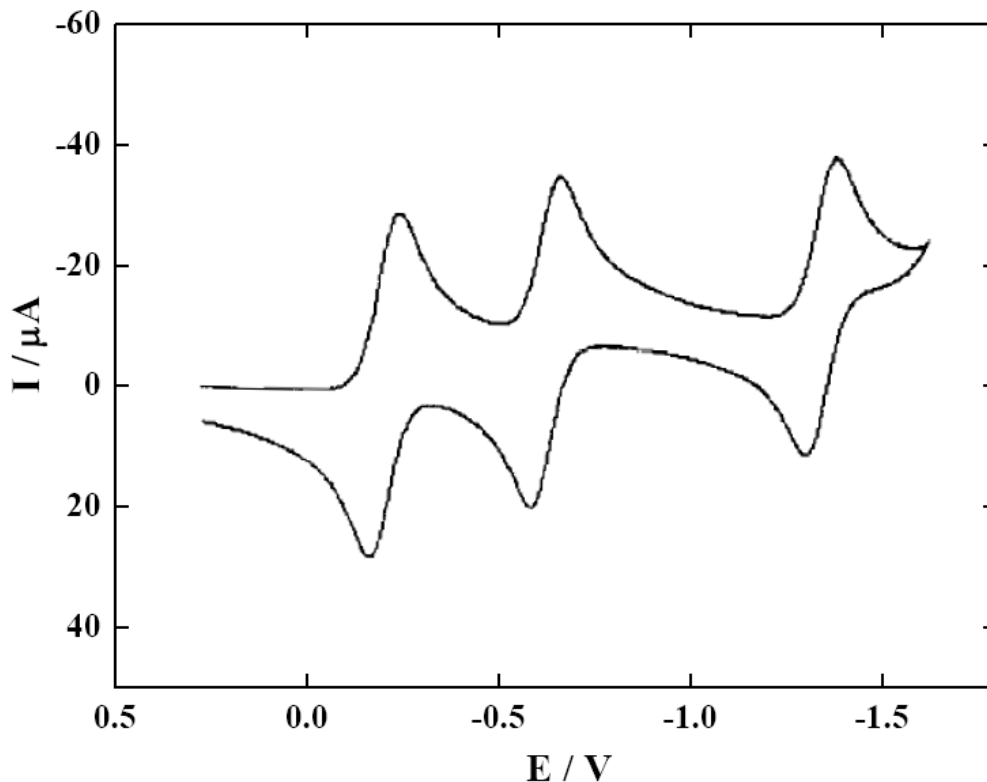


Figure 1.12 Cyclic voltammogram of 0.5 mM $[\text{PMo}_{12}\text{O}_{40}]^{3-}$ in CH_3CN containing 0.05 M $n\text{-Bu}_4\text{NClO}_4$. (from Ref. 63)

POMs also exhibit excellent electrical properties, such as the ability to undergo rapid and reversible multi-electron redox reactions, the possibility to tune their redox potentials by metal ions substitution without affecting their structure, and good ionic and electronic conductivity. For example, the phosphomolybdate anions, $[\text{PMo}_{12}\text{O}_{40}]^{3-}$ (PMo12), which exhibit three electrons reversible redox reactions (Fig. 1.12), have been used as cathode-active materials for lithium batteries, though the details of the battery reaction mechanism remained unclear.

1.3.2. Mn12 molecular cluster batteries

In 2007, the first molecular cluster battery was fabricated by using Mn12Ac molecular clusters that undergo multi-electron redox reactions as a cathode active material in order to achieve both high capacity and fast charging/discharging.^[64] Figure 1.13(a) schematically shows the structure of the Mn12 molecular cluster battery. Since the electronic conductivity of Mn12Ac is not so high, VGCF (Vapor Growth Carbon Fiber) is employed to increase the conductivity of the electrode.

Figure 1.13(b) shows an SEM image of the cathode; it looks as if a microcrystal of Mn12 is electrically wired with VGCF. The anode material is lithium metal foil that is isolated from the cathode by a separator (polyolefin film). The cathode and anode are placed in a coin-type cell (Model: CR2032) with a 1.0 M LiPF₆ electrolyte in a mixed solution of diethyl carbonate (DEC) and ethylene carbonate (EC) (DEC/EC = 7/3) in an inert atmosphere.

The battery cell is cycled galvanostatically in the voltage range of 4.2 – 2.0 V at a constant current density of 0.1 mA. In this case, a positive current causes the oxidation of the cathode, whereas a negative current causes its reduction. Figure 1.14 shows the charge/discharge curves, and cycle performance of Mn12Ac/Li molecular cluster battery. The black curve indicates the first charging; the voltage quickly exceeds 4.0 V from the initial high voltage (3.8 V). It is likely that this battery is already charged in the fabrication process of the coin cell. The red curve shows the

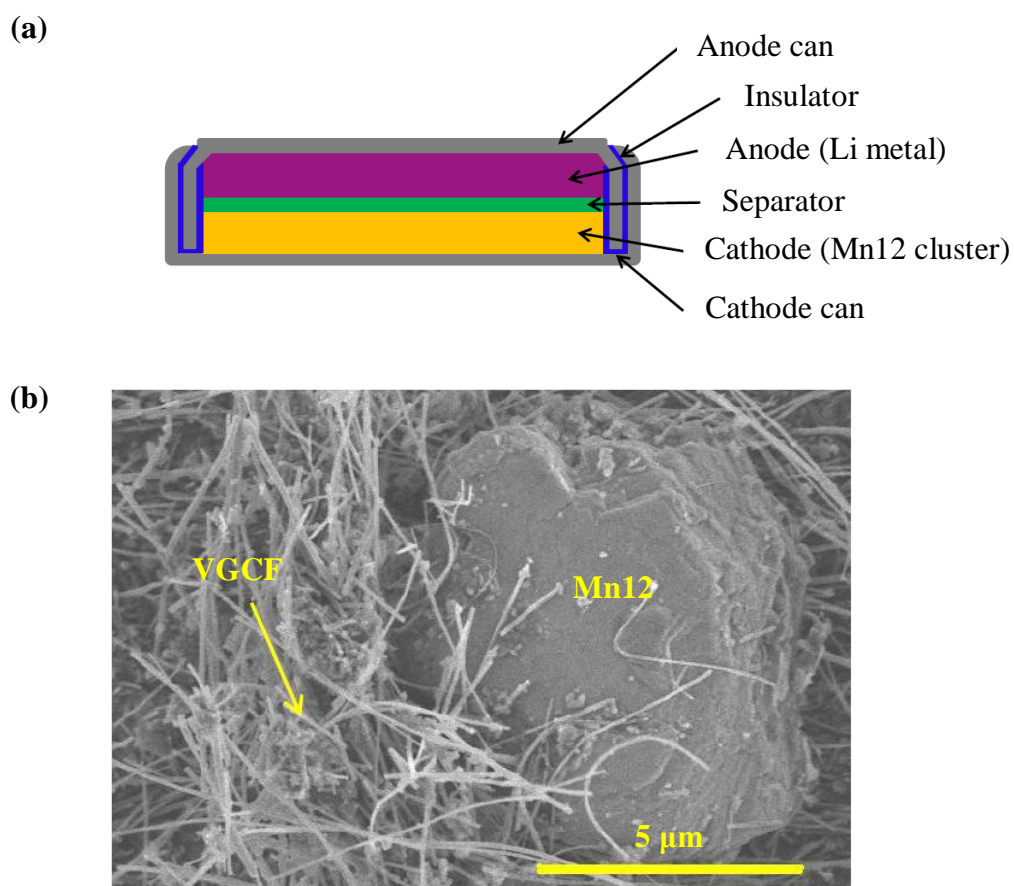


Figure 1.13 (a) Schematic sketch of the Mn12Ac/Li molecular cluster battery. (b) SEM image of the cathode.

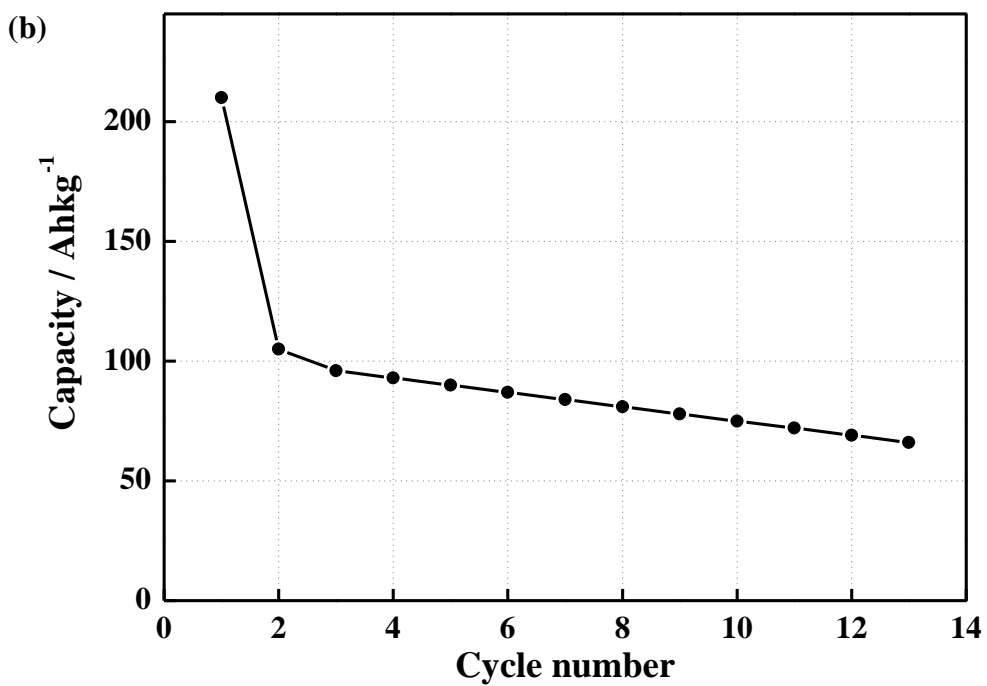
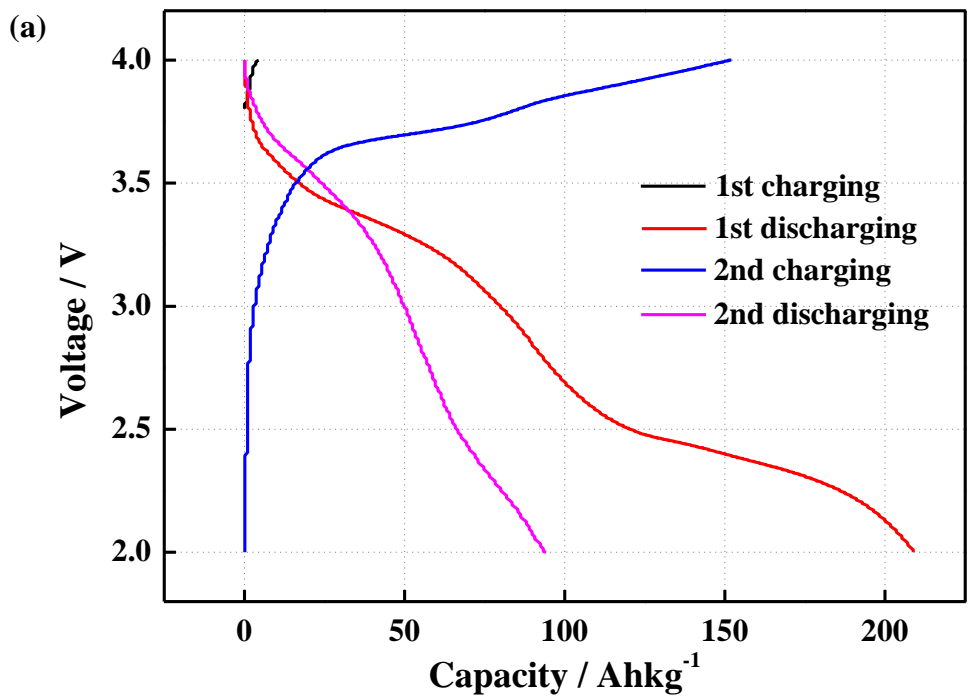


Figure 1.14 (a) Charging/discharging curves, and (b) cycle performance of the Mn₁₂Ac/Li molecular cluster battery. (from Ref. 64)

first discharging process; the voltage exhibits a gradual decrease, making two narrow plateaus at 3.4 V and 2.5 V, indicating a large capacity of ca. 200 Ah/kg. This value is larger than that of the Li-ion battery. The blue and pink curves indicate the second charging and discharging processes, respectively. In charging, the voltage quickly increases to a plateau at 3.7 V, followed by a gradual increase. In discharging, the voltage gradually decreases with a shoulder at 3.5 V, finally indicating a capacity of ca. 90 Ah/kg. This value is much lower than that for the first discharging, but is comparable to those of the organic radical batteries. The cycle performance for the charging/discharging processes indicates that the large capacity in the first run significantly decreases, and finally the capacity is maintained at a constant value of 75 Ah/kg, though it tends to gradually decrease.

The theoretical capacity is calculated for the Mn₁₂Ac/Li battery. If one Mn₁₂Ac cluster molecule stores one electron, the capacity would be 14 Ah/kg. Therefore, the capacity in the second run or later can be explained by a few electrons reduction reactions of Mn₁₂Ac. However, it might be hard to rationalize the large capacity in the first run. When the high rate performance is examined with 1 mA, the capacity decreases rather quickly during the charging/discharging processes. The slow rate of the charging/discharging reactions for the Mn₁₂Ac MCBs is caused by the slow electron diffusion speed in the insulating microcrystals of Mn₁₂Ac. Understanding the cathode reaction mechanism is important for developing molecular cluster batteries, and this motivates us to reveal the reaction mechanism using various physical methodologies.

1.4. Methodology to elucidate the battery reaction

Investigation on the reactions of the cathode materials plays an important role in developing high performance rechargeable batteries. While long-range order structural information is available from X-ray diffraction (XRD), solid-state nuclear magnetic resonance (NMR) and X-ray absorption fine structure (XAFS) are powerful tools for characterizing electronic properties and local structures in the cathode materials, without long-range structural ordering.^[65-69] Recently, some new

technology was developed to study the electronic properties of the cathode materials such as STM-EELS (Scanning Tunneling Microscopy-Electron Energy-Loss Spectroscopy). Here, some of these techniques are explained.^[70]

1.4.1. Solid-state NMR

Lithium solid-state (NMR) is very sensitive to the presence of electron spins, leading to a very precise characterization of the local environments surrounding the probed nuclei, e.g., ${}^6\text{Li}$, ${}^7\text{Li}$, ${}^{31}\text{P}$ and ${}^{29}\text{Si}$.^[71-73] Therefore, in order to understand the mechanism of the Li^+ -ion-insertion reactions, and to improve the electrochemical performance of the LiCoO_2 cathode materials, Delmas *et al.* performed the characterization of the state of Li^+ ions in the LiCoO_2 cathode by solid-state Li NMR.^[74] The *ex situ* ${}^7\text{Li}$ MAS (magic angle spinning) NMR spectra of the deintercalated Li_xCoO_2 ($0.5 < x < 1.0$) reveal that a weak new peak appears at 57 ppm when $x < 0.94$ (Fig. 1.15). This peak grows at the expense of the peak of 0 ppm during $0.94 > x > 0.75$. For $x < 0.75$, the peak at 0 ppm disappears, and

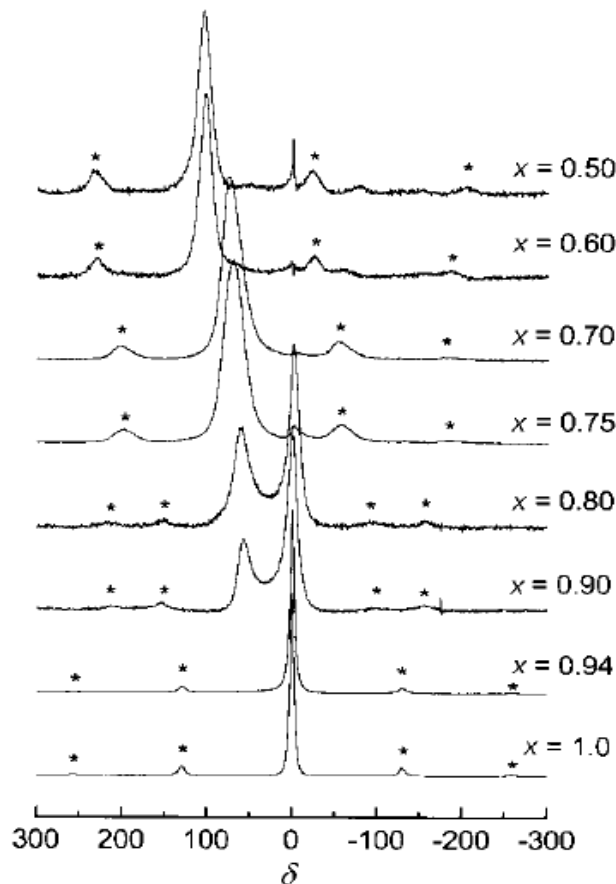


Figure 1.15 ${}^7\text{Li}$ MAS NMR spectra for Li_xCoO_2 cathode materials. (from Ref. 74)

the new one shifts to higher fields. NMR indicates that a drastic change of the electronic interactions, and a phase transition, occurs in this material. Recently, much effort has been devoted to developing *in situ* solid-state NMR experiments to study the details of the battery reaction mechanism under realistic operating conditions.

1.4.2. XAFS

XAFS analysis is an appropriate technique for observing valence and local structure changes of nanoscale or highly disordered compounds, such as battery active materials.^[75] Two different regions of the XAFS absorption spectra are useful: X-ray absorption near edge structure (XANES), and extended X-ray absorption fine structure (EXAFS). XANES yields information on the oxidation states of the absorbing atoms, while EXAFS provides the local environments of the absorbing atoms. They give important insights into the battery reaction mechanisms. Since the time evolution of electrochemical reactions could not be obtained using *ex situ* XAFS measurements, much effort has been devoted to develop *in situ* XAFS measurement systems. Figure 1.16 shows a schematic view of an *in situ* transmission XAFS cell for studying the charge/discharge process of LiMn_2O_4 cathode materials.^[76] The averaged oxidation state of the Mn ions, and the local structure parameters (coordination

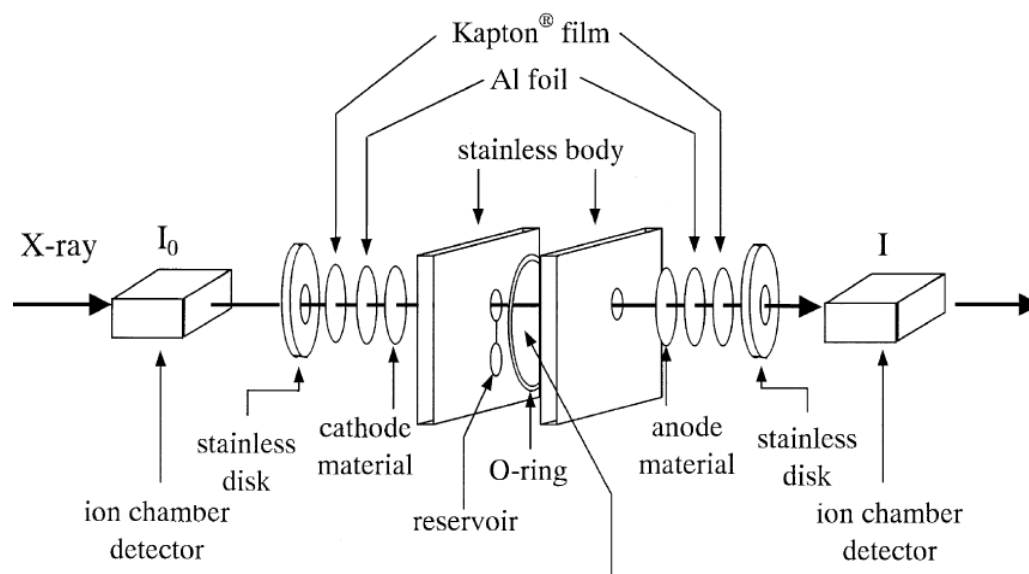


Figure 1.16 A schematic illustration of the *in situ* cell for the transmission XAFS measurements. (from Ref. 76)

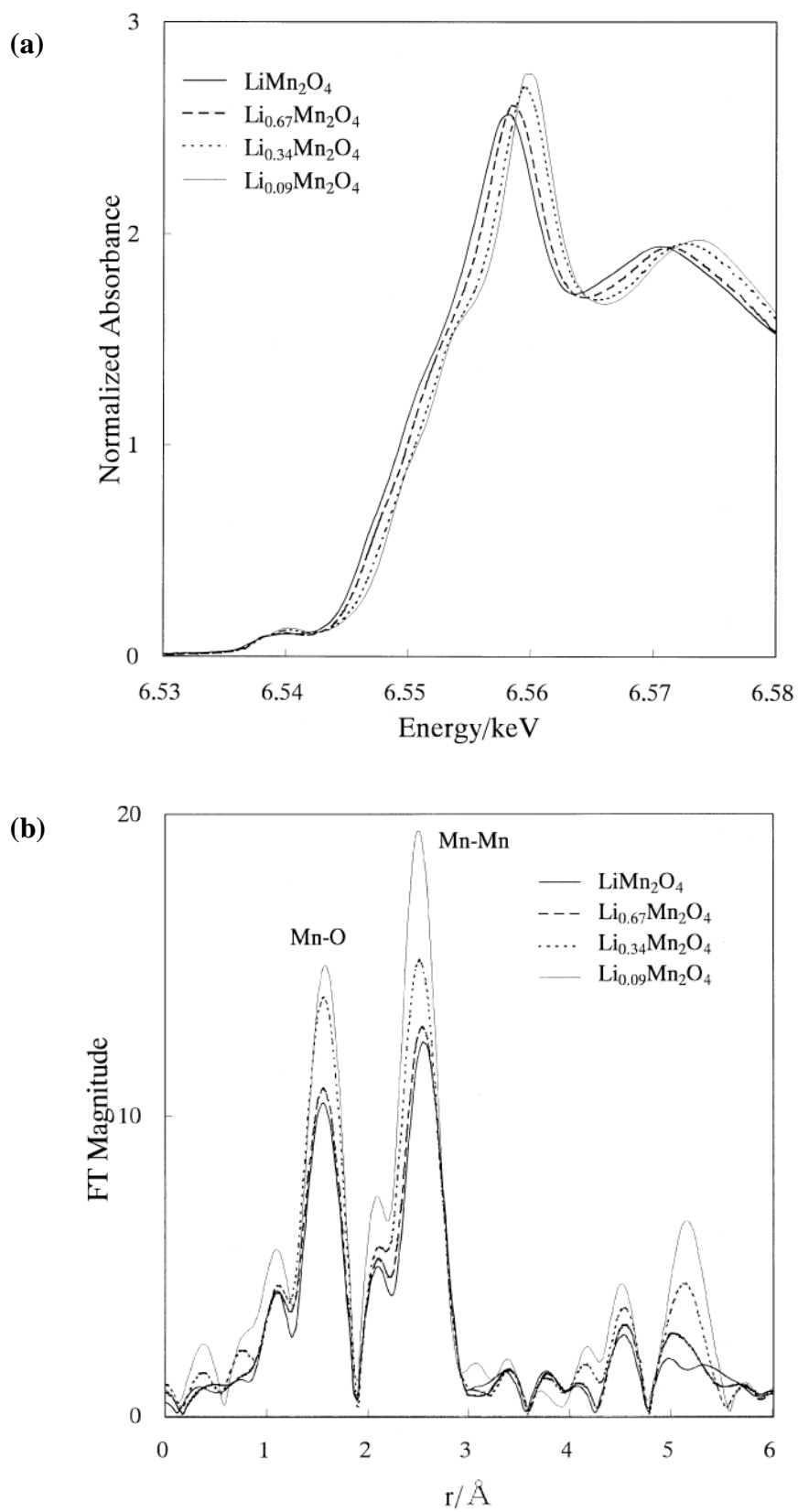


Figure 1.17 *In situ* Mn *K*-edge XANES spectra (a) and EXAFS spectra (b) of $\text{Li}_{1-x}\text{Mn}_2\text{O}_4$. (from Ref. 76)

number, inter-atomic distance, Debye-Waller factor) are obtained from the Mn *K*-edge XANES and EXAFS spectra measured during a discharging process (Fig. 1.17). The results show that addition of excess lithium to LiMn_2O_4 can improve the cyclic reversibility of the Li-ion batteries. Using an *in situ* XAFS cell, it is possible to reveal the electrochemical reactions of the cathode materials during the charging/discharging processes.

1.4.3. STM-EELS

Real-space observation of the locations of Li^+ ions in the cathode materials is important to understand the mechanisms of redox reactions and structural deteriorations. Conventional characterization methods, such as XRD and NMR, are not suitable to clarify the relationship between the position of Li^+ ions and the nanostructure of the cathode. STM-EELS (scanning transmission electron microscopy

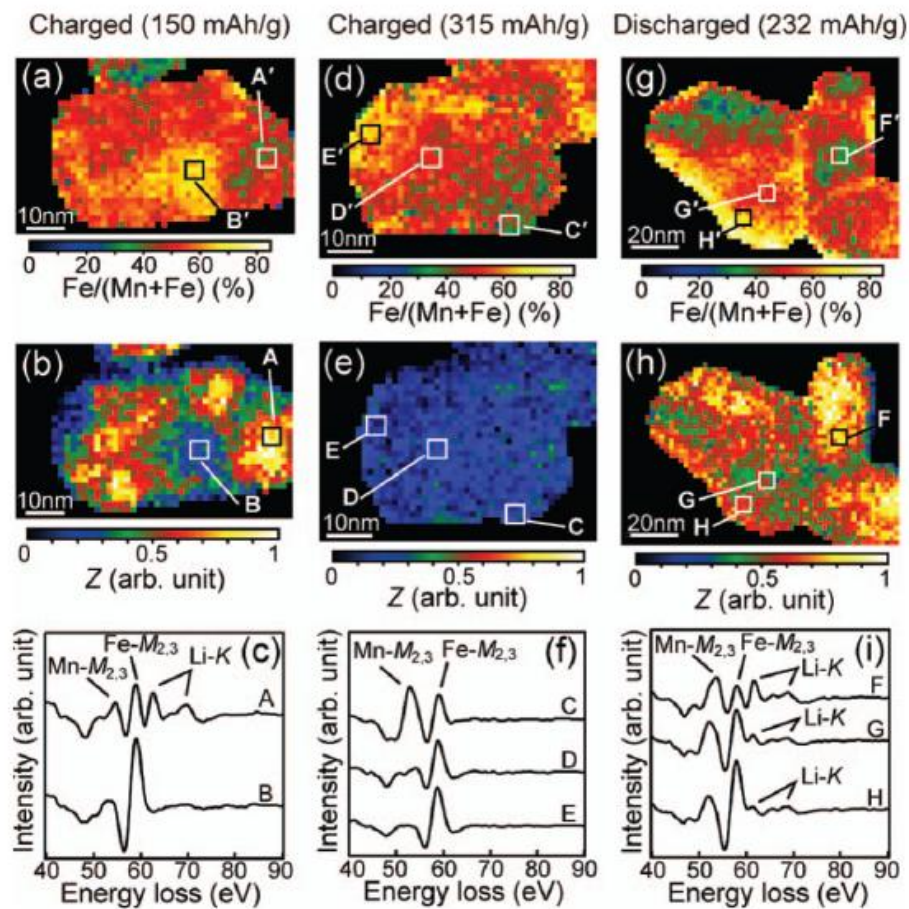


Figure 1.18 Observation of Li^+ extraction and insertion in $\text{Li}_{1.2-x}\text{Mn}_{0.4}\text{Fe}_{0.4}\text{O}_2$ cathode materials. (from Ref. 70)

electron energy-loss spectroscopy) is a powerful method to monitor the distribution of chemical species and the electronic properties of the cathode materials at nanoscale.^[77, 78] Figure 1.18 shows the Li⁺ extraction and insertion processes in a Li_{1.2-x}Mn_{0.4}Fe_{0.4}O₂ cathode material at different charging/discharging states (from left to right: 50% charging, 100% charging and 100% discharging).^[70] The distribution of Li⁺ is inhomogeneous, and has a strong correlation with the transition metal ions. At the beginning of the initial charging, Li⁺ extraction occurs in Fe-rich regions, and Mn-rich regions retain many Li⁺ ions. At the end of the initial charging, Li⁺ ions are extracted from the Mn-rich regions. This method can clarify the Li⁺ ion distribution during charging/discharging in the cathode materials. Real-space observation techniques will become popular in the rechargeable battery technology.

1.5. Scope of this thesis

The present work focuses on revealing the reaction mechanism and fundamental role of the Mn12 molecule and [PMo₁₂O₄₀]³⁻ (PMo12) in MCBs, and helps to derive a guiding principle for new cathode materials. In chapter 2, the valence state and local structure changes of the Mn and Mo ions in Mn12 and PMo12 batteries are investigated by *in situ* XAFS analysis. In chapter 3, the solid-state ⁷Li NMR and cyclic voltammetry for the Mn12 MCBs are studied. In chapter 4, the magnetic properties of Mn12 with various reduction states during discharging are discussed. Finally, in chapter 5, the reaction mechanism is summarized, and a bright prospect of MCBs can be envisioned.

References

- [1] R. A. Huggins, *Advanced Batteries: Materials Science Aspects*, Springer, New York, **2009**.
- [2] M. Winter, J. B. Brodd, *Chem. Rev.* **2004**, *104*, 4245.
- [3] J. -M. Tarascon, M. Armand, *Nature* **2001**, *414*, 359-367.
- [4] D. Linden, T. B. Reddy, *Handbook of Batteries* (3rd Edition), McGraw-Hill,

New York, **2002**.

- [5] M. Armand, J. -M. Tarascon, *Nature* **2008**, *451*, 652-657.
- [6] C. Liu, F. Li, L. P. Ma, H. M. Cheng, *Adv. Mater.* **2010**, *22*, E28-E62.
- [7] Z. G. Yang, J. Liu, S. Baskaran, C. H. Imhoff, J. D. Holladay, *JOM US* **2010**, *62*, 14-23.
- [8] T. Nagaura, K. Tozawa, *Prog. Batt. Sol. Cells.* **1990**, *9*, 209-217.
- [9] P. G. Bruce, B. Scrosati, J. -M. Tarascon, *Angew. Chem. Int. Ed.* **2008**, *47*, 2930-2946.
- [10] P. G. Bruce, *Solid state Ionics.* **2008**, *179*, 752-760.
- [11] F. Y. Cheng, Z. L. Tao, J. Liang, J. Chen, *Chem. Mater.* **2008**, *20*, 667-681.
- [12] F. Y. Cheng, J. Liang, Z. L. Tao, J. Chen, *Chem. Mater.* **2011**, *23*, 1695-1715.
- [13] B. L. Ellis, K. T. Lee, L. F. Nazar, *Chem. Mater.* **2010**, *22*, 691-714.
- [14] K. Ozawa, *Lithium Ion Rechargeable Batteries*, Wiley-Vch, **2002**.
- [15] G. G. Amatucci, J. -M. Tarascon, L. C. Klein, *J. Electrochem. Soc.* **1996**, *143*, A1114-A1123.
- [16] H. Gabrisch, R. Yazami, B. Fultz, *J. Electrochem. Soc.* **2004**, *151*, A891-A897.
- [17] W. B. Luo, J. R. Dahn, *Electrochim. Acta.* **2009**, *54*, 4655-4661.
- [18] Y. S. Jung, A. S. Cavanagh, A. C. Dillon, M. D. Groner, S. M. George, S. H. Lee, *J. Electrochem. Soc.* **2010**, *157*, A75-A81.
- [19] J. Kim, M. Noh, J. Cho, H. Kim, K. Kim, *J. Electrochem. Soc.* **2005**, *152*, A1142-A1148.
- [20] H. Miyashiro, A. Yamanaka, M. Tabuchi, S. Seki, M. Nakayama, Y. Ohno, Y. Kobayashi, Y. Mita, A. Usami, M. Wakihara, *J. Electrochem. Soc.* **2006**, *153*, A348-A352.
- [21] T. Ohzuku, Y. Makimura. *Chem. Lett.* **2001**, *7*, 642-644.
- [22] S. Jouanneau, K. W. Eberman, L. J. Krause, J. R. Dahn, *J. Electrochem. Soc.* **2003**, *150*, A1637-A1642.
- [23] K. Ariyoshi, E. Iwata, M. Kuniyoshi, H. Wakabayashi, T. Ohzuku, *Electrochem. Solid State Lett.* **2006**, *9*, A557-A560.
- [24] D. K. Kim, P. Muralidharan, H. W. Lee, R. Ruffo, Y. Yang, C. K. Chan, H. Peng,

- R. A. Huggins, Y. Cui, *Nano Lett.* **2008**, *8*, 3948-3952.
- [25] E. Hosono, T. Kudo, I. Honma, H. Matsuda, H. S. Zhou, *Nano Lett.* **2009**, *9*, 1045-1051.
- [26] A. K. Padhi, K. S. Nanjundaswamy, K. S. Goodenough, *J. Electrochem. Soc.* **1997**, *144*, 1188-1194.
- [27] H. Huang, S. C. Yin, L. F. Nazar, *Electrochem. Solid State Lett.* **2001**, *4*, A170-A172.
- [28] S. Y. Chung, J. T. Blocking, Y. M. Chiang, *Nat. Mater.* **2002**, *1*, 123-128.
- [29] P. P. Prosini, M. Lisi, D. Zane, M. Pasquali, *Solid State Ionics* **2002**, *148*, 45-51.
- [30] R. Amin, J. Maier, P. Balaya, D. P. Chen, C. T. Lin, *Solid State Ionics* **2008**, *179*, 1683-1687.
- [31] A. V. Churikov, A. V. Ivanishchev, I. A. Ivanishcheva, V. O. Sycheva, N. R. Khasanova, E. V. Antipov, *Electrochim. Acta.* **2010**, *55*, 2939-2950.
- [32] F. Y. Cheng, W. Tang, C. S. Li, J. Chen, H. K. Liu, P. W. Shen, S. X. Dou, *Chem. Eur. J.* **2006**, *12*, 3082-3088.
- [33] X. Y. Han, C. X. Chang, L. J. Yuan, T. L. Sun, J. T. Sun, *Adv. Mater.* **2007**, *19*, 1616-1621.
- [34] M. Satoh, K. Nakahara, J. Iriyama, S. Iwasa, M. Suguro, *IEICE Trans. Electron.*, **2004**, *E87-C*, 2076-2080.
- [35] K. Nakahara, S. Iwasa, M. Satoh, Y. Morioka, J. Iriyama, M. Suguro, E. Hasegawa, *Chem. Phys. Lett.* **2002**, *359*, 351-354.
- [36] H. Nishide, S. Iwasa, Y. J. Pu, T. Suga, K. Nakahara, M. Satoh, *Electrochem. Acta.* **2004**, *50*, 827-832.
- [37] T. Suga, H. Ohshiro, S. Sugita, K. Oyaizu, H. Nishide, *Adv. Mater.* **2009**, *21*, 1627-1630.
- [38] H. Nishide, K. Koshika, K. Oyaizu, *Pure. Appl. Chem.* **2009**, *81*, 1961-1670.
- [39] K. Nakahara, K. Oyaizu, H. Nishide, *Chem. Lett.* **2011**, *40*, 222-227.
- [40] M. Armand, S. Grugeon, H. Vezin, S. Laruelle, P. Ribière, P. Poizot, J. -M. Tarascon, *Nat. Mater.* **2009**, *8*, 120-125.
- [41] H. Y. Chen, M. Armand, M. Courty, M. Jiang, C. Grey, F. Dolhem, J. -M.

- Tarascon, P. Poizot, *J. Am. Chem. Soc.* **2009**, *131*, 8984-8988.
- [42] E.K. Brechin, M. Soler, J. Davidson, D.N. Hendrickson, S. Parsons, G. Christou, *Chem. Commun.* **2002**, *19*, 2252-2253.
- [43] S. M. J. Aubin, M. W. Wemple, D. M. Adams, H.-L. Tsai, G. Christou, D. N. Hendrickson, *J. Am. Chem. Soc.* **1996**, *118*, 7746-7754.
- [44] E. K. Brechin, J. Yoo, M. Nakano, J. C. Huffman, D. N. Hendrickson and G. Christou, *Chem. Commun.* **1999**, *3*, 783-784.
- [45] C. Boskovic, E. K. Brechin, W. E. Streib, K. Folting, D. N. Hendrickson, Christou, *Chem. Commun.* **2001**, *5*, 467-468.
- [46] C. Sangregorio, T. Ohm, C. Paulsen, R. Sessoli, D. Gatteschi, *Phys. Rev. Lett.* **1997**, *78*, 4645-4648.
- [47] A.-L. Barra, A. Caneschi, A. Cornia, F. Fabrizi de Biani, D. Gatteschi, C. Sangregorio, R. Sessoli, L. Sorace, *J. Am. Chem. Soc.* **1999**, *121*, 5302-5310.
- [48] C. Benelli, J. Cano, Y. Journaux, R. Sessoli, G. A. Solan, R. E. P. Winpenny, *Inorg. Chem.* **2001**, *40*, 188-189.
- [49] C. Cadiou, M. Murrie, C. Paulsen, V. Villar, W. Wernsdorfer, R. E. P. Winpenny, *Chem. Commun.* **2001**, *24*, 2666-2667.
- [50] M. Sadakane, E. Steckhan, *Chem. Rev.* **1998**, *98*, 219-237.
- [51] G. Christou, *Polyhedron.* **2005**, *24*, 2065-2075.
- [52] R. Bagai, G. Christou, *Chem. Soc. Rev.* **2009**, *38*, 1011-1026.
- [53] T. Lis, *Acta Crystallogr. Sect. B* **1980**, *36*, 2041-2046.
- [54] R. Sessoli, D. Gatteschi, A. Caneschi, M. Novak, *Nature* **1993**, *365*, 141-143.
- [55] R. Sessoli, H. L. Tsai, A. R. Schake, S. Wang, J. B. Vincent, K. Folting, D. Gatteschi, G. Christou, D. N. Hendrickson, *J. Am. Chem. Soc.* **1993**, *115*, 1804-1816.
- [56] L. Thomas, F. Lioni, R. Ballou, D. Gatteschi, R. Sessoli, B. Barbara, *Nature* **1996**, *383*, 145-147.
- [57] J. M. Hernandez, X. X. Zhang, F. Luis, J. Tejada, J. R. Friedman, M. P. Sarachik, R. Ziolo, *Phys. Rev. B* **1997**, *55*, 5858-5865.
- [58] J. A. A. J. Perenboom, J. S. Brooks, S. Hill, T. Hathaway, N. S. Dalal, *Phys. Rev.*

- B **1998**, 58, 330-338.
- [59] D. E. Katsoulis, *Chem. Rev.* **1998**, 98, 359-387
- [60] V. Kozhevnikov, *Chem. Rev.* **1998**, 98, 171-198.
- [61] M. S. Kaba, I. K. Song, D. C. Duncan, C. L. Hill, M. A. Barteau, *Inorg. Chem.* **1998**, 37, 398-406.
- [62] T. Okuhara, N. Mizuno, M. Misono, *Adv. Catal.* **1996**, 41, 113-252.
- [63] K. Maeda, S. Himeno, T. Osakai, A. Saito, T. Hori, *J. Electroanal. chem.* **1994**, 364, 149-154.
- [64] H. Yoshikawa, C. Kazama, K. Awaga, M. Sato, J. Wada, *Chem. Commun.* **2007**, 30, 3169-3170.
- [65] C. P. Grey, N. Dupre, *Chem. Rev.* **2004**, 104, 4493-4512.
- [66] C. P. Grey, Y. J. Lee, *Solid state Science* **2003**, 5, 883-894.
- [67] W. S. Yoon, N. Kim, X. Q. Yang, J. M. Breen, C. P. Grey, *J. Power. Sources.* **2003**, 5, 649-653.
- [68] J. E. Penner-Hahn, *Coord. Chem. Rev.* **1999**, 190-192, 1101-1123.
- [69] S. Gross, M. Bauer, *Adv. Funct. Mater.* **2010**, 20, 4026-4047.
- [70] J. Kikkawa, T. Akita, M. Tabuchi, M. Shikano, K. Tatsumi, M. Kohyama, *Electrochem. Solid State Lett.* **2008**, 11, 183-185.
- [71] B. Key, R. Bhattacharyya, M. Morcrette, V. sezner, J. -M. Tarascon, C. P. Grey, *J. Am. Chem. Soc.* **2009**, 131, 9239-9249.
- [72] R. Bhattacharyya, B. Key, H. Chen, A. S. Best, A. F. Hollenkamp, C. P. Grey, *Nat. Mater.* **2010**, 9, 504-510.
- [73] N. Yamakawa, M. Jiang, B. Key, C. P. Grey, *J. Am. Chem. Soc.* **2009**, 131, 10525-10536.
- [74] M. Menetrier, I. Saadoune, S. Levasseur, C. Delmas, *J. Mater. Chem.* **1999**, 9, 1135-1140.
- [75] M. S. Islame, B. Ammundsen, D. J. Jones, J. Roziere, *Materials for Lithium-Ion Batteries*, eds. Julien, C. Stoyinov, Z. Academic Publisher, Netherlands, **2000**, 279.
- [76] Nakai, Y. Shiraishi, F. Nishikawa, 1999, *Spectrochimica Acta Part B* **1999**, 54,

143-149.

- [77] K. Suenaga, M. Tenc \acute{e} C. Mory, C. Colliex, H. Kato, T. Okazaki, H. Shinohara, K. Hirahara, S. Bandow, and S. Iijima, *Science* **2000**, *290*, 2280-2282.
- [78] K. Kimoto, T. Asaka, T. Nagai, M. Saito, Y. Matsui, and K. Ishizuka, *Nature* **2007**, *450*, 702-704.

Chapter 2

In situ XAFS studies of MCBs

2.1. Introduction

X-ray absorption fine structure (XAFS) has been recognized as a powerful structural characterization method due to its advantages such as element specificity, sensitivity to short-range order (typically several Å), and chemical state. It can provide a microscopic picture of the local structure surrounding the absorber atom, *i.e.* the oxidation state, the geometric structure, the type, number and distances of coordinated atoms. The sensitivity to the short-range order makes XAFS capable of probing the structural and electronic changes for a variety of systems, no matter whether the studied samples are crystalline or amorphous.^[1-4]

When an incident beam of monochromatic X-ray of energy E passes through a homogeneous sample, the incident intensity decreases according to the Beer-Lambert law:

$$I_t = I_0 e^{-\mu(E)x} \quad (2.1)$$

where I_0 and I_t are the incident and transmitted X-ray intensities, respectively, where x is the sample thickness, and $\mu(E)$ is the linear absorption coefficient.

The absorption coefficient $\mu(E)$ gradually decreases with increasing the energy of the incident photon. When the incoming X-ray photon has a larger energy than the binding energy of a core electron, this electron is excited to a vacant excited state, or to the continuum, and a sharp rise in the absorption intensity appears (Fig. 2.1(a)). This steep rise is named the absorption edge. For atoms in a molecule, or in a condensed phase, the higher energy region above the absorption edge displays a fine structure, which is due to the scattering by the neighboring atoms surrounding the absorbing atom (Fig. 2.1(b)). In XAFS experiments, the intensity of $\mu(E)$ as a function of energy is studied. As the core electrons in an atom have a characteristic binding energy, which depends on the atomic number, we can select the studied element by tuning the X-ray energy to the absorption range.

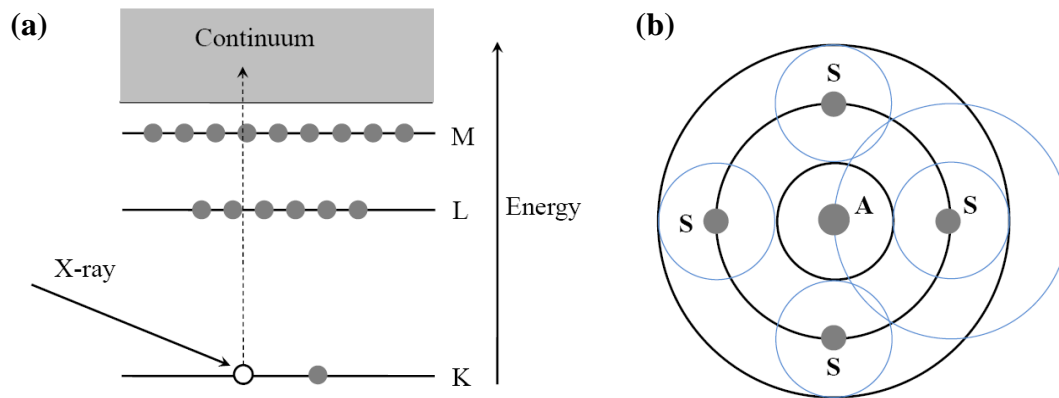


Figure 2.1 (a) Schematic representation of the excitation process of X-ray absorption. (b) Schematic view of the scattering of an outgoing wave by neighboring atoms. A and S refer to the absorbing and scattering atoms, respectively.

A typical XAFS spectrum for an Mn12 cluster is shown in Fig. 2.2. The abrupt rise in $\mu(E)$ is clearly shown above 6540 eV due to the absorption of Mn 1s electrons. XAFS is often divided into two regions, namely the X-ray absorption near edge structure (XANES), covering the edge region, and the extended X-ray absorption fine structure (EXAFS), starting from approximately 30 eV above the absorption edge.^[5,6] The XANES region is dominated by the electronic state of the absorbed atom, in addition to the multiple scatterings of photoelectrons due to their low kinetic energies. In contrast, the EXAFS region is dominated by the single scattering effects of electron waves propagating in a nearly constant electronic potential. The XANES analysis can provide the details regarding the oxidation states of absorber atoms, and the EXAFS study can offer information about the local structures around them.

Many kinds of XAFS measurement methods have been developed using synchrotron radiation light sources: transmission XAFS for usual materials, fluorescence XAFS for dilute impurity elements and thin-film samples, magnetic XAFS for spin-state research, *in situ* XAFS for state-transformation investigation, space- and time-resolved XAFS for dynamics.^[7] Figure 2.3 shows an experimental setup scheme of the transmission XAFS measurement. The absorption coefficient $\mu(E)$ can be directly measured using this. So far, *ex situ* XAFS has been widely utilized to study the local structural changes of the battery cathode materials.^[8] Recently, *in situ*

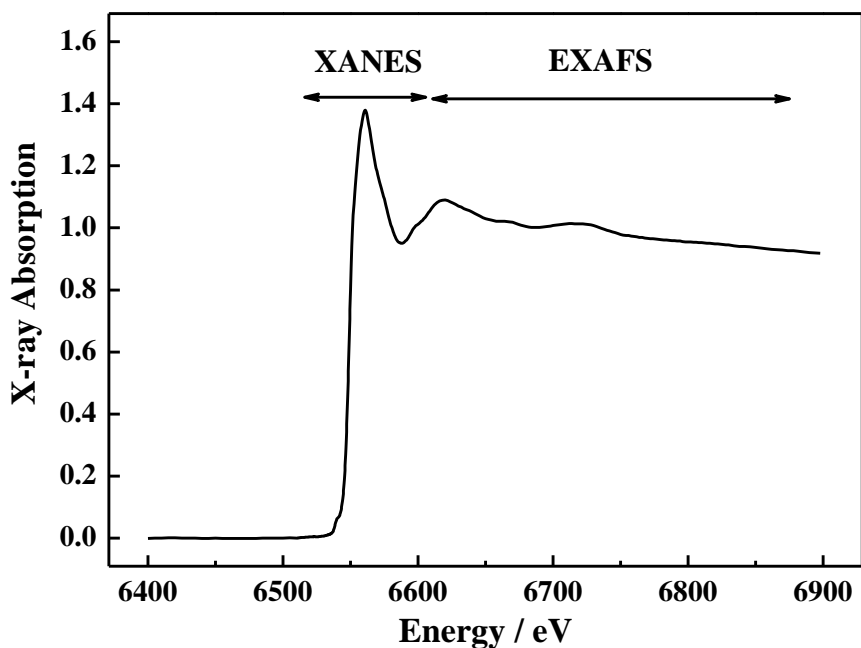


Figure 2.2 Mn *K*-edge XAFS spectrum of Mn12 cluster.

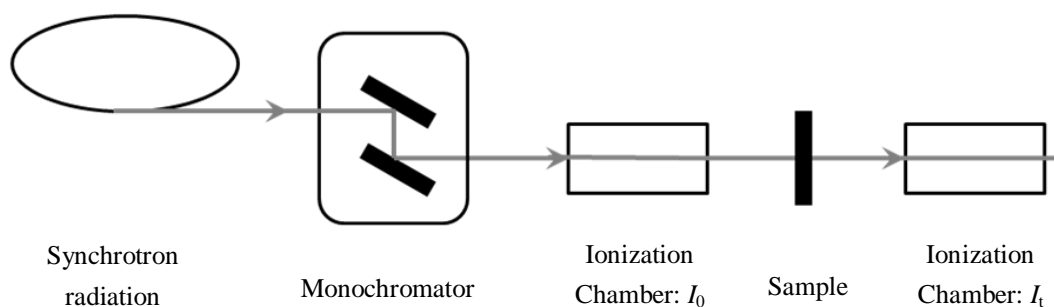


Figure 2.3 Experimental set-up for transmission mode measurement.

XAFS has also been developed, since it allows us to directly monitor the solid-state electrochemical reactions in the batteries, without disassembling the cells, thus avoiding possible air oxidation and moisture attack.^[9-11]

In the present study, we performed *in situ* Mn and Mo *K*-edge XAFS measurements for Mn12- and PMo12-MCBs, respectively. Here, we describe the valence states and local structures of the Mn and Mo ions in these battery reactions.

2.2. Experimental section

2.2.1. Materials

Two kinds of molecular clusters, $\text{Mn}_{12}\text{Pe}^t$ ($[\text{Mn}_{12}\text{O}_{12}(\text{CH}_3\text{CH}_2\text{C}(\text{CH}_3)_2\text{COO})_{16}(\text{H}_2\text{O})_4]$) and $\text{TBA}_3[\text{PMo}_{12}\text{O}_{40}]$ ($\text{TBA} = [\text{N}(\text{CH}_2\text{CH}_2\text{CH}_2\text{CH}_3)_4]^+$), were used as cathode materials. The synthetic methods of these two molecular clusters are described as follows.

Preparation of $\text{Mn}_{12}\text{Pe}^t$ ($[\text{Mn}_{12}\text{O}_{12}(\text{CH}_3\text{CH}_2\text{C}(\text{CH}_3)_2\text{COO})_{16}(\text{H}_2\text{O})_4]$)

$\text{Mn}_{12}\text{Pe}^t$ (Fig. 2.4(a)), containing a bulky *t*-pentyl carboxylate ligand, was used as a cathode-active material for the XAFS studies, because it was more stable than Mn_{12}Ac . $\text{Mn}_{12}\text{Pe}^t$ was prepared by the ligand substitution method for Mn_{12}Ac .^[12] The starting material, Mn_{12}Ac , was prepared as reported.^[13] An acetonitrile solution of Mn_{12}Ac was treated with a solution of HO_2CPe^t in CH_2Cl_2 . The solution was stirred overnight, and the solvent was then removed in vacuo. The residue was dissolved in toluene, and the solution was again evaporated to dryness. This procedure was repeated twice. The residue was then dissolved in CH_2Cl_2 , and treated again with HO_2CPe^t in CH_2Cl_2 . After three more cycles of the addition and removal of toluene, the residue was redissolved in CH_2Cl_2 . After filtration, and the addition of MeNO_2 , the solution was allowed to stand at 4 °C for 4 days. The resulting black crystals of $\text{Mn}_{12}\text{Pe}^t$ were collected by filtration, washed with MeNO_2 , and dried in vacuo. Finally, they were identified by infrared (IR) spectroscopy.

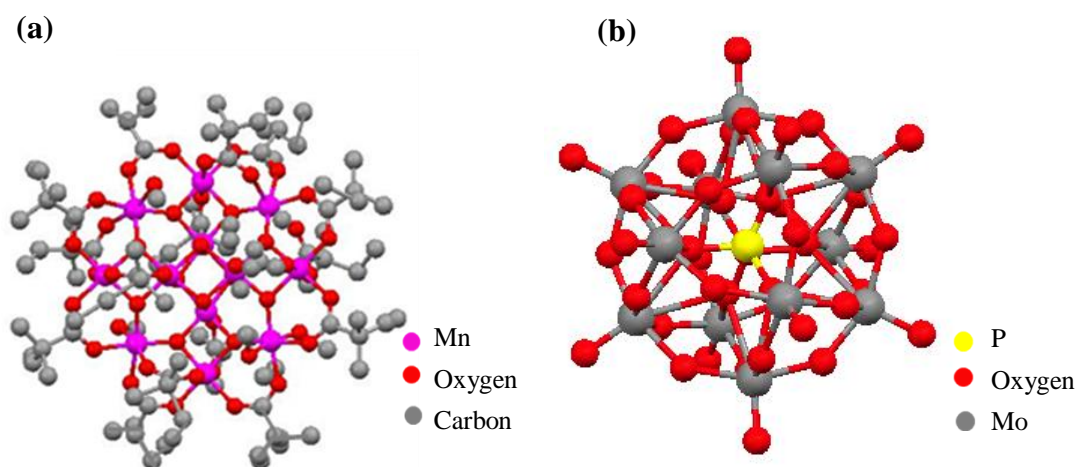


Figure 2.4 (a) Molecular structure of $\text{Mn}_{12}\text{Pe}^t$ (b) Molecular structure of $[\text{PMo}_{12}]^{3-}$.

Preparation of $\text{TBA}_3[\text{PMo}_{12}\text{O}_{40}]$ ($[\text{N}(\text{CH}_2\text{CH}_2\text{CH}_2\text{CH}_3)_4]_3[\text{PMo}_{12}\text{O}_{40}]$)

$\text{TBA}_3[\text{PMo}_{12}\text{O}_{40}]$, with a Keggin-type structure, was synthesized according to a classical preparation method (Fig. 2.4(b)).^[14] $\text{H}_3\text{PMo}_{12}\text{O}_{40}$ (1.83 g) was firstly dissolved in 10 ml of water. Addition of 0.97 g of $(\text{C}_4\text{H}_9)_4\text{NBr}$ in 10 ml water precipitated a crude $\text{TBA}_3[\text{PMo}_{12}\text{O}_{40}]$. After filtration, the obtained yellowish solid was washed with water, ethanol, and ether, and was recrystallized in acetone. The purity was confirmed by IR spectroscopy.

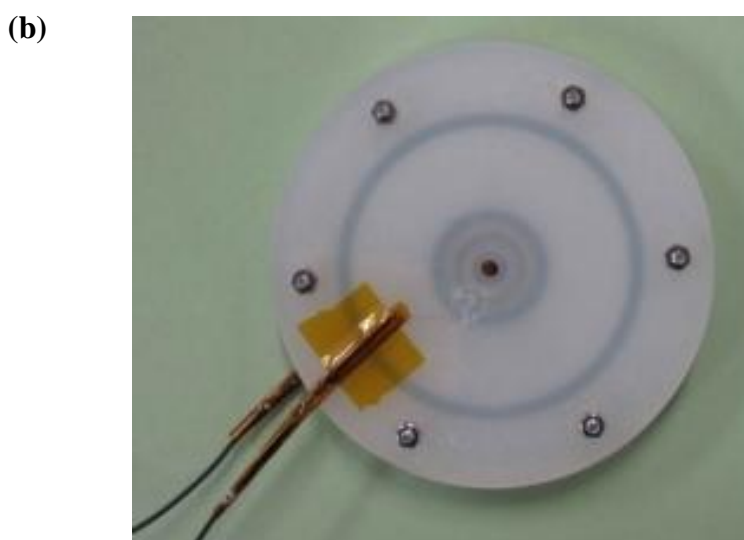
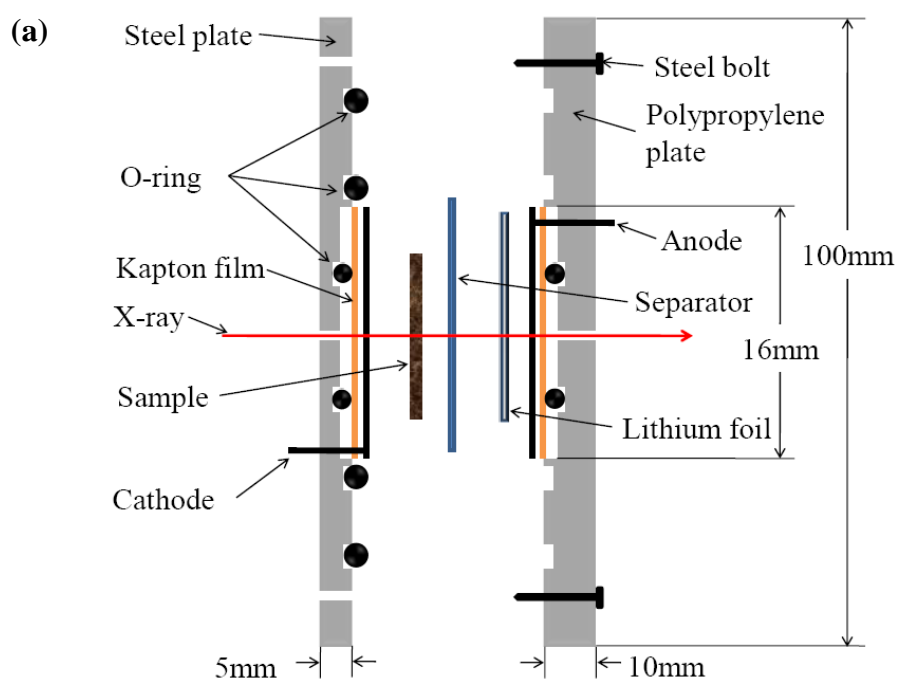


Figure 2.5 Schematic sketch (a) and photograph (b) of the *in situ* cell.

2.2.2. Battery cells for *in situ* XAFS measurements.

We have developed a battery reaction cell for *in situ* XAFS studies, modifying a cell previously reported in the literature.^[15] A sketch of the present cell is illustrated in Fig. 2.5. The battery cell, with a diameter of 16 mm, is formed in-between a stainless steel and a polypropylene plate. These outside plates have an X-ray window in the center, which is made of a Kapton film. The sample space, shielded by two concentric O-rings, includes a cathode and an anode, separated by a separator. This *in situ* electrochemical cell is re-usable and portable, and the O-ring sealing allows the experiments to run for several days without significant degradation of the electrodes.

2.2.3. Battery analyses of MCBs

For the *in situ* XAFS measurements, batteries were prepared using the following assembly procedure. The cathodes were prepared by mixing 10:70:20 weight ratio of Mn12Pe^t, carbon black, and polytetrafluoroethylene suspended in water (60 % PTFE solution) for Mn12Pe^t MCBs. PMo12 MCBs were fabricated, replacing Mn12Pe^t with TBA₃PMo₁₂, and polytetrafluoroethylene with polyvinylidene fluoride (PVDF). The slurry mixture was then spread evenly (0.5 mm thickness, diameter 15 mm) onto an aluminum plate and dried. The anode material was lithium metal foil (0.1 mm thickness). 1 M LiPF₆ dissolved in a 7:3 volumetric mixture of diethyl carbonate (DEC), and ethylene carbonate (EC) was used as electrolyte. A polyolefin film was used as a separator. The cells were assembled in an Ar glovebox, and cycled galvanostatically in the voltage of 2.0 – 4.0 V at a constant current of 0.1 mA for Mn12Pe^t MCBs and in the voltage range of 1.5 – 4.0 V at a constant current of 1 mA for PMo12 MCBs, respectively. The specific charging/discharging capacities were calculated based on the weight of active material (Mn12Pe^t or TBA₃[PMo₁₂O₄₀]) in the cathode.

2.2.4. XAFS measurements

Measurements of Mn12 MCBs

In situ Mn *K*-edge XAFS spectra of Mn12Pe^t MCBs were recorded in the energy range of 6210.0 to 7190.0 eV, with a transmission mode at the beam line BL-12C of the Photon Factory in KEK, Tsukuba, Japan (Fig. 2.6). The *in situ* cell was placed

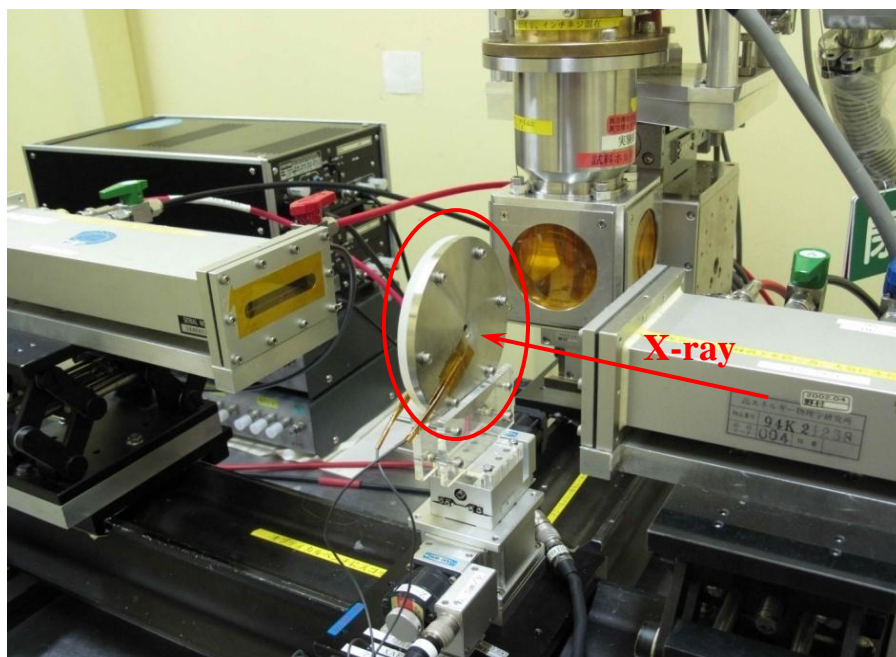


Figure 2.6 Schematic sketch of the *in situ* XAFS measurements (BL-12C).

between two transmission ion chambers. A Si (111) double-crystal monochromator was used to select a specific X-ray energy. The intensities, I_0 and I_t , of incident and transmitted X-rays were measured using ionization chambers filled with a He/N₂ mixture (7:3) for an incident beam, and N₂ (100%) for a transmitted beam. During *in situ* XAFS measurements, the area of the cathode subjected to X-ray, was ca. 1 mm × 1 mm. To avoid chemical decomposition of Mn₁₂Pe^t by X-ray, a Quick-XAFS (QXAFS) method was adapted, by which one spectrum was obtained within 60 sec. During the charging/discharging reactions, we performed the measurements with an interval of 15 mins. The reference materials, MnO, Mn₃O₄, Mn₂O₃, and MnO₂, diluted with boron nitride, also were measured using the same measurement conditions.

Measurements of PMo12 MCBs

In situ Mo *K*-edge XAFS spectra of PMo12 MCBs were recorded in the energy range from 19498.9 to 20003.9 eV with a transmission mode at room temperature, using the beam line BL-NW10A of the Photon Factory Advanced Ring (PF-AR) in KEK, Tsukuba, Japan. An *in situ* battery cell was placed between two transmission ion chambers. A Si (311) monochromator was used to select a specific X-ray energy. The intensities of the incident (I_0) and transmitted X-ray (I_t) were measured with

ionization chambers filled with Ar and Kr, respectively. During *in situ* XAFS measurements, the area of the cathode subjected to X-ray, was ca. 1 mm × 1 mm. To avoid chemical decomposition of PMo12 by X-ray, the QXAFS method was adapted, by which one spectrum was obtained within 60 sec. During the charging/discharging reactions, we performed the measurements with an interval of 60 sec. We also measured QXAFS of the pellet samples of the reference materials, metal Mo, TBA₃PMo12, MoO₂, and Li₂MoO₄, which are diluted with boron nitride, using the same measurement conditions.

2.2.5 XAFS data analysis

Data analysis of Mn12Pe^t MCBs

The software REX2000 (Rigaku Corp.)^[16] was used for analysis of the XANES and EXAFS for Mn12Pe^t MCBs. XANES spectra were obtained by pre-edge background subtraction, with Victoreen-like functions, and subsequent normalization. The EXAFS functions of $k^3(k)$ (k is a photoelectron wave number) were obtained by standard procedures of pre-edge baseline subtraction, edge-energy determination, post-edge background subtraction (cubic spline), and normalization using the atomic absorption coefficients. Subsequently, k^3 -weighted $\chi(k)$ data in the range of 2 – 11.5 Å⁻¹ for Mn *K*-edge were Fourier-transformed to r -space. All possible scattering paths and backscattering amplitudes for curve-fitting were calculated by FEFF (8.2).^[17] EXAFS spectra in r -space over the range of 0 – 6 Å were fitted using theoretically calculated scattering paths to obtain structural parameters, such as the coordination numbers (the number of neighboring atoms), bond distances, Debye-Waller factors, and energy shifts.

Data analysis of PMo12 MCBs

XANES spectra of PMo12 MCBs were analyzed through the same procedure as that for Mn12Pe^t MCBs, using the software REX2000. EXAFS analyses were carried out by standard procedures using the analysis program EXAFSH written by Yokoyama et al.^[18] The EXAFS oscillation functions $k^3\chi(k)$ (k being the photoelectron wave number) were obtained by pre-edge base line subtraction, post-edge background estimation using cubic spline functions, and normalization with the atomic absorption

coefficients. The employed Δk ranges in the Fourier transforms were approximately 2 – 12 \AA^{-1} for Mo *K*-edge. Curve-fitting of the *in situ* EXAFS data were performed by using the backscattering amplitudes, and the phase shifts for the appropriate Mo-O and Mo-Mo shells, which were calculated from the crystal structure of MoO₂ using the *ab initio* multiple scattering code FEFF 8.4,^[19, 20] or were obtained from the experimental EXAFS spectra of the reference materials, TBA₃PMo12 and Li₂MoO₄. Subsequently, the structural parameters, such as the coordination numbers (the number of neighboring atoms), and interatomic distances were determined for Mo-O and Mo-Mo in the PMo12 molecule during charging/discharging.

2.3. *In situ* XAFS studies of Mn12 MCBs

2.3.1. Charging/discharging curves of Mn12 MCBs

Figure 2.7 shows the charging/discharging curves of an Mn12Pe^t/Li battery obtained at a constant current of 0.1 mA/cm² in the voltage range of 2.0 – 4.0 V. These data were recorded during the *in situ* XAFS measurements. The black curve indicates the first charging process of the as-prepared cell; the voltage increases from the initial high value of 3.5 V, and quickly reaches 4.0 V, thus indicating that the battery was already charged in the fabrication process. These voltages roughly agree with the working potential of this battery, namely 3.5 V against Li, calculated from the mono-electron reduction potential of Mn12Pe^t in its cyclic voltammogram.^[21] The red curve shows the first discharging process; the voltage exhibits a gradual decrease, and indicates a large capacity of ca. 210 Ah/kg. The second charging process (green) exhibits a quick voltage increase to ca. 3.5 V, followed by a gradual increase. The second discharging curve (blue) is very similar to the first one (red), without showing an obvious decrease in capacity. This *in situ* cell exhibits a similar cycle performance to the coin cell.

It is notable that, in our previous works of the Mn12Ac MCBs, the battery capacity in the second cycle became smaller by ca. 100 Ah/kg than that of the first cycle.^[22] As described in the next chapter, this decrease would be caused by the disappearance of a capacitance effect, such as formation of electrical double

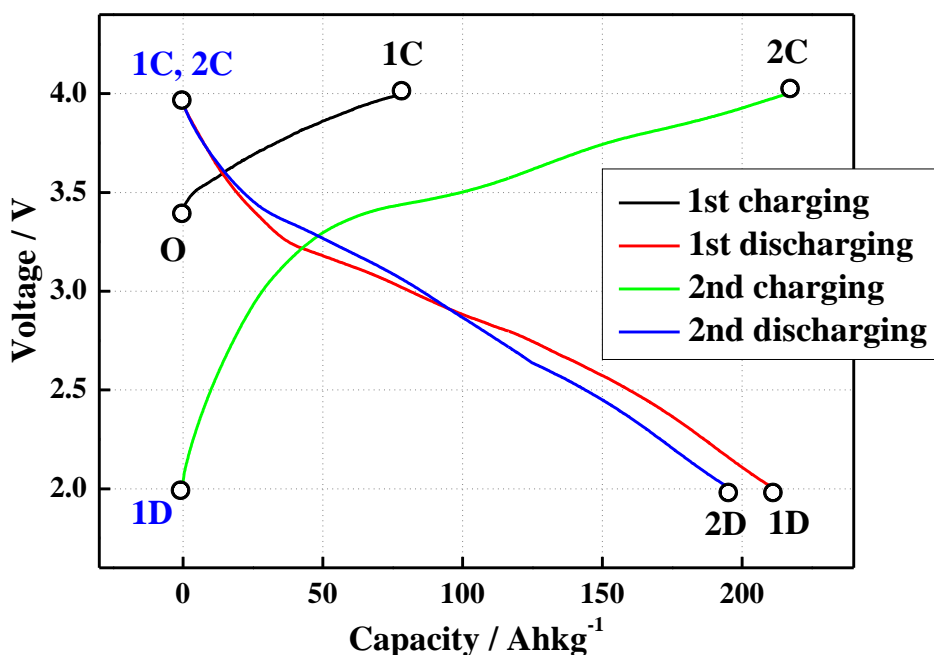


Figure 2.7 Charging/discharging curves of Mn₁₂Pe^t MCBs. The labels, **O**, **1C**, **1D**, **2C** and **2D**, indicate the characteristic samples in the first two cycles of the battery reaction.

layers, in the second cycle or later.

2.3.2. *In situ* XANES analyses

Figure 2.8 shows the normalized Mn *K*-edge XANES spectra in the first charging (black curves), the first discharging (red), the second charging (green), and the second discharging (blue). These data were simultaneously taken during the charging/discharging curve measurements shown in Fig. 2.7. Figure 2.9 shows the XANES spectra for the second charging/discharging processes. They exhibit a systematic change with an isosbestic point at 6555 eV. The neutral Mn₁₂Pe^t molecule consists of eight Mn³⁺ and four Mn⁴⁺ ions, and the presence of the isosbestic point means that only one of the Mn³⁺ or Mn⁴⁺ ions exhibits a valence change in this battery reaction.^[27] It is also notable that every spectrum includes a weak peak at 6540 eV, which is known to indicate that the Mn ions are in an octahedral coordination.^[23]

Figure 2.10 shows a linear relationship between the Mn oxidation state and the X-ray absorption edge energy for the reference materials, MnO, Mn₃O₄, Mn₂O₃, and MnO₂, where the edge energy is defined as the point of the largest gradient on the

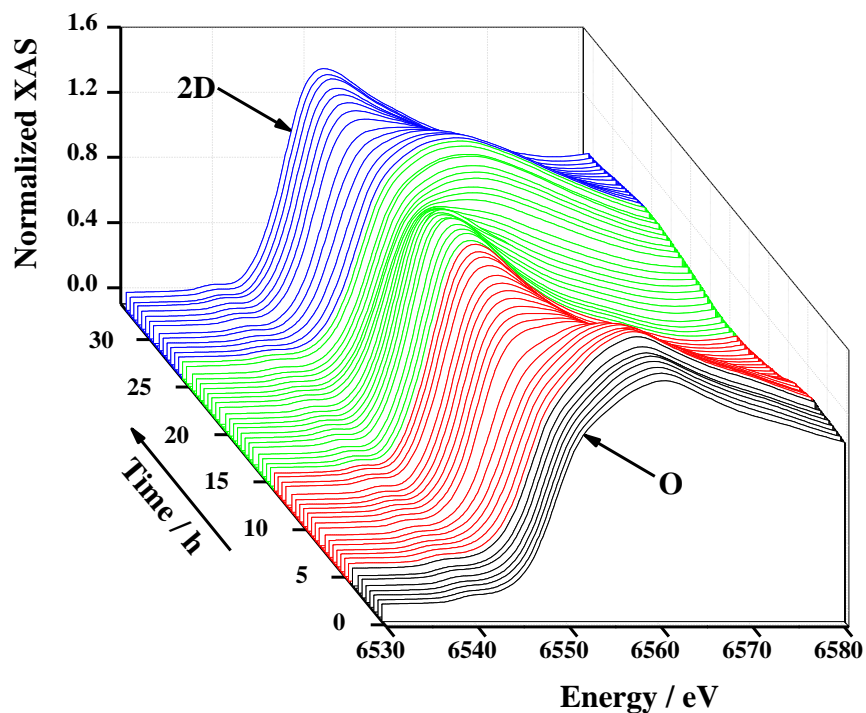


Figure 2.8 Evolution of the normalized *in situ* Mn *K*-edge XANES spectra for Mn12Pe' MCBs during the first two cycles.

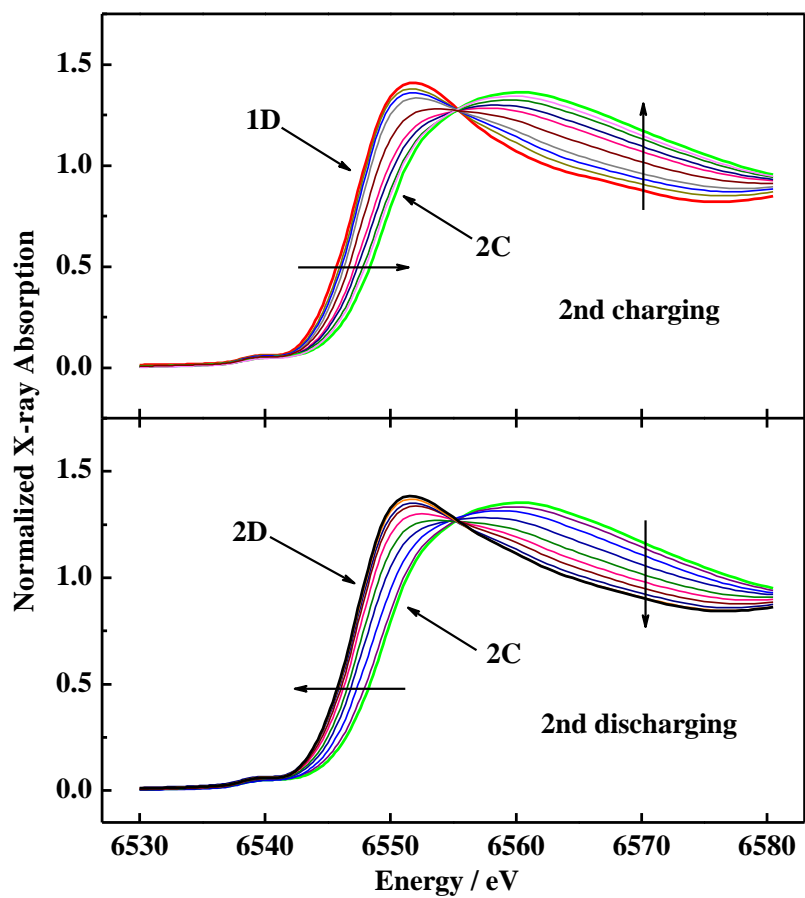


Figure 2.9 Manganese *K*-edge XANES spectra for Mn12Pe' MCBs in the second charging/discharging.

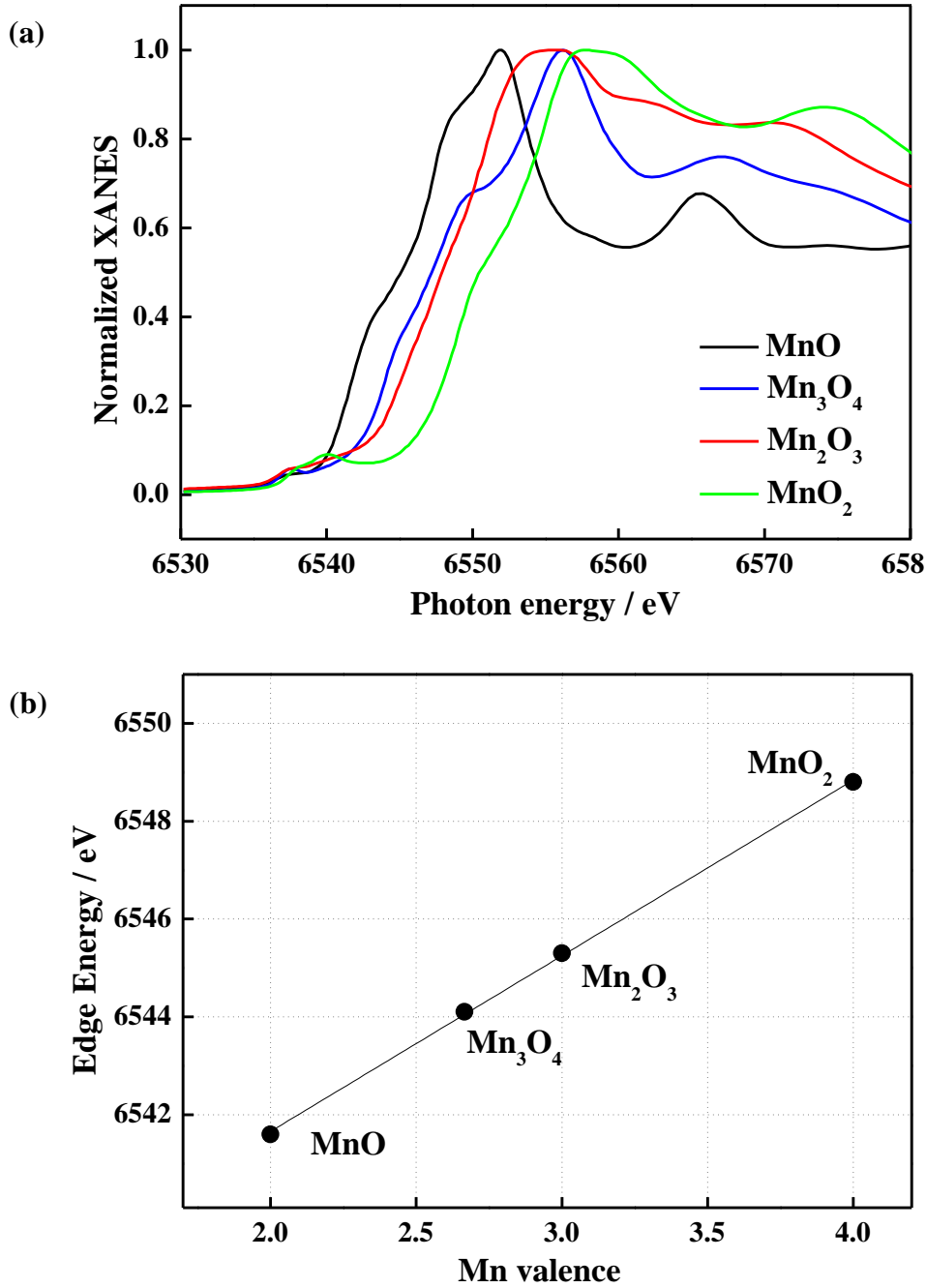


Figure 2.10 Normalized Mn *K*-edge XANES spectra (a) and Mn valence vs. edge energy (b) for the reference materials MnO, Mn₃O₄, Mn₂O₃, and MnO₂.

absorption curve. By using this relation, the averaged valence N_v of the Mn ions in Mn12Pe['] was obtained as $N_v = \text{total Mn valence}/12$. The results are shown in Fig. 2.11, where the values of N_v are plotted as a function of the battery voltage V (see Fig. 2.7). The initial value of N_v before the first charging is 3.3, which agrees with that of the neutral Mn12Pe['] with $N_v = 3.33$. After the first charging, N_v shows only a slight increase to 3.5, which is consistent with the small changes in voltage and capacity in

the first charging. The first discharging brings about a quick decrease in N_v , and the value reaches 2.5 at $V = 2.8$ V. Unexpectedly, N_v becomes constant in the range of 2.8 – 2.0 V, though the discharging curve still exhibits a capacity (see Fig. 2.7). The second charging increases the value of N_v from 2.5 to 3.3 after a plateau in the range of 2.0 – 3.0 V. This behavior is consistent with that in the discharging process. The N_v change by 0.9 during the first discharging indicates an approximately ten-electron reduction per one Mn12 molecule, and corresponds to a battery capacity of ca. 100 Ah/kg. This value is in good agreement with the capacity indicated in the voltage range of 2.8 – 4.0 V (see Fig. 2.6), but is a half of the total value (210 Ah/kg). In the other words, the capacity of ca. 110 Ah/kg obtained in the voltage range of 2.0 – 2.8 V can likely be explained by something other than a redox change of the Mn ions. Since the redox reaction of the organic parts, such as carboxylate ligand in Mn12, is not possible in this voltage range, this capacity likely comes from a capacitance effect, as we will describe in Chapter 3.

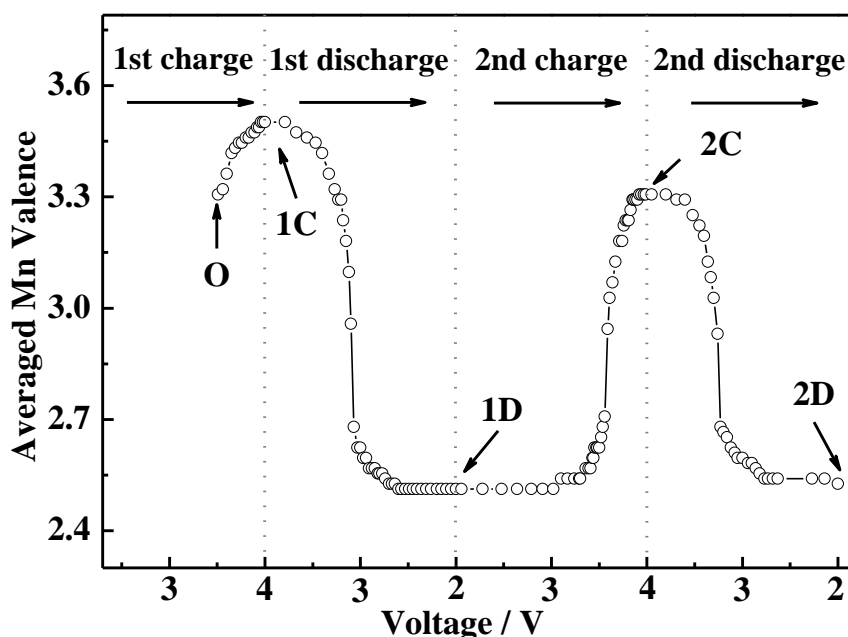


Figure 2.11 Averaged Mn valence of $\text{Mn}_{12}\text{Pe}^I$ in the Mn12 MCBs as a function of cell voltage V (V).

2.3.3. *In situ* EXAFS analyses

EXAFS analyses were performed in order to obtain the structural change of the Mn12Pe^t molecule. The open circles in Fig. 2.12 show the Fourier transform (FT) spectra of the k^3 -weighted data (k range is around 2.5 – 11.0 Å⁻¹) for the samples denoted by **O**, **1C**, **1D**, **2C**, and **2D** in Figs. 2.11. These spectra indicate radial atomic distribution around the manganese centers. Before the first charging, sample **O** exhibits three main peaks at 1.4, 2.4, and 3.1 Å. The peak at 1.4 Å is assigned to the Mn-O distance, while the other two are attributed to short and long Mn-Mn distances. Although this sample is the neutral Mn12Pe^t, which consists of Mn³⁺ and Mn⁴⁺, the Fourier transform exhibits a single Mn-O peak at 1.4 Å. These results indicate that the local structures of Mn³⁺ and Mn⁴⁺ in the skeleton of Mn12 cannot be distinguished by this analysis (see Fig. 2.4(a)). The curve of **1C** is nearly the same as that of **O**. After the first discharging, **1D** exhibits a very different curve; the peak at 1.4 Å becomes very small, and a new peak appears at 1.8 Å. The evolution of the FT spectra in this first discharging (reduction) process from **1C** to **1D** is depicted in Fig. 2.13. It is clear that the peaks at 1.4 and 1.8 Å swap their intensities, as the voltage V decreases from 4.0. The generation of the peak at 1.8 Å is probably caused by an increase in the levels of Mn²⁺ ions, as indicated by the Mn-O distances in MnO₂ and MnO being 1.87 Å and 2.22 Å, respectively. After the second charging, the sample **2C** exhibits an initial three peaks (Fig. 2.12), though their intensities are slightly smaller than those of **1C**. After the second discharging, the curve of **2D** is nearly the same as that of **1D**.

We carried out a quantitative analysis of the EXAFS data in Fig. 2.12. Because the local structures of Mn³⁺ and Mn⁴⁺ in the skeleton of Mn12 cannot be distinguished, we assume the coexistence of two independent Mn-O₆ octahedra, namely Mn³⁺/Mn⁴⁺-O₆ and Mn²⁺-O₆. However, we did not take into account the whole molecular skeleton of Mn12 as a combined structure of the two octahedra, so as to avoid overparameterization, and do not try to fit the peaks for the Mn-Mn distances. The red curves in Fig. 2.12 are the theoretical best fits of the two independent Mn-O₆ octahedra model, to the peaks at 1.4 and 1.8 Å. In this

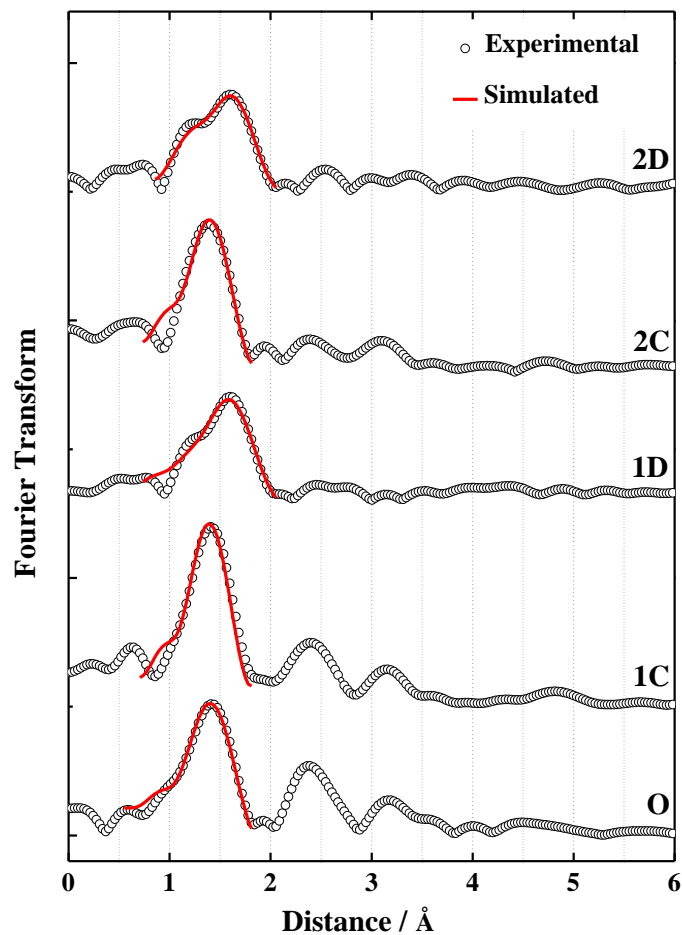


Figure 2.12 The experimental and simulated Fourier transforms of the Mn *K*-edge EXAFS spectra for **O**, **1C**, **1D**, **2C** and **2D**.

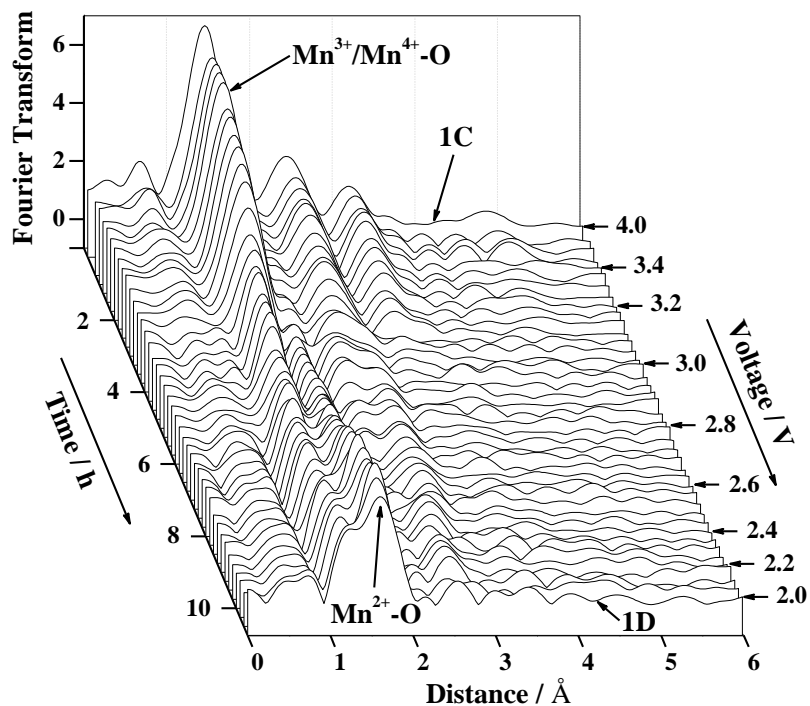


Figure 2.13 Evolution of the fourier transforms of the Mn *K*-edge EXAFS spectra in the first discharging.

analysis, Debye-Waller factors are scaled to the fixed values of 0.065 and 0.089 Å for $\text{Mn}^{3+}/\text{Mn}^{4+}\text{-O}_6$ and $\text{Mn}^{2+}\text{-O}_6$, respectively. This assumption is justified since the relative thermal displacements of $\text{Mn}^{3+}/\text{Mn}^{4+}\text{-O}_6$ and $\text{Mn}^{2+}\text{-O}_6$ atom pairs are not significantly affected by the higher nearest neighbor atoms and, moreover, we considered only the ratio of the coordination numbers for $\text{Mn}^{3+}/\text{Mn}^{4+}\text{-O}_6$ and $\text{Mn}^{2+}\text{-O}_6$. We also fixed the energy shift to an appropriate value of -2 and -3 eV for $\text{Mn}^{3+}/\text{Mn}^{4+}\text{-O}_6$ and $\text{Mn}^{2+}\text{-O}_6$, respectively, because the interatomic distances for $\text{Mn}^{3+}/\text{Mn}^{4+}\text{-O}_6$ and $\text{Mn}^{2+}\text{-O}_6$ are not discussed here. The theoretical curves can explain the curvatures below 2.0 Å fairly well, which strongly suggests that the Mn12 core structure is maintained in the charging/discharging (oxidation/reduction) processes.

2.3.4. Internal redox processes of Mn12 clusters in MCBs

The XANES analysis indicates that either the Mn^{3+} or Mn^{4+} ions in the neutral Mn12 change their oxidation state, and that the super-reduced species of Mn12, with a negative charge of ca. -10 , is obtained after the discharging. The EXAFS analysis suggests that the $\text{Mn}^{3+}/\text{Mn}^{4+}\text{-O}_6$ octahedra are gradually converted into the $\text{Mn}^{2+}\text{-O}_6$ during discharging. Because all the anion species of Mn12 synthesized thus far have structures in which some of the Mn^{3+} are replaced with Mn^{2+} ,^[24, 25] it is reasonable to conclude that the super-reduced species would be $[\text{Mn12}]^{8-}$, possessing eight Mn^{2+} ions.

The open circles in Fig. 2.14 show the evolution of the $\text{Mn}^{3+}/\text{Mn}^{2+}$ numbers in Mn12 as a function of the battery voltage, V , which were calculated from the XANES data in Fig. 2.10. The closed circles in this figure indicate the results from the EXAFS analysis, which shows the coordination numbers of the Mn^{3+} and Mn^{2+} ions. In this analysis, it is assumed that the redox reaction takes place only between Mn^{3+} and Mn^{2+} without changing the Mn^{4+} sites. The V dependencies of the $\text{Mn}^{3+}/\text{Mn}^{2+}$ numbers resulting from XANES and EXAFS analysis are in good agreement with each other. In the range of 4.0 – 3.3 V, the decrease in the Mn^{3+} ions is negligibly small, despite the discharging. This result could be caused by the fully charged species including cation species of Mn12Pe^t . In the narrow range of

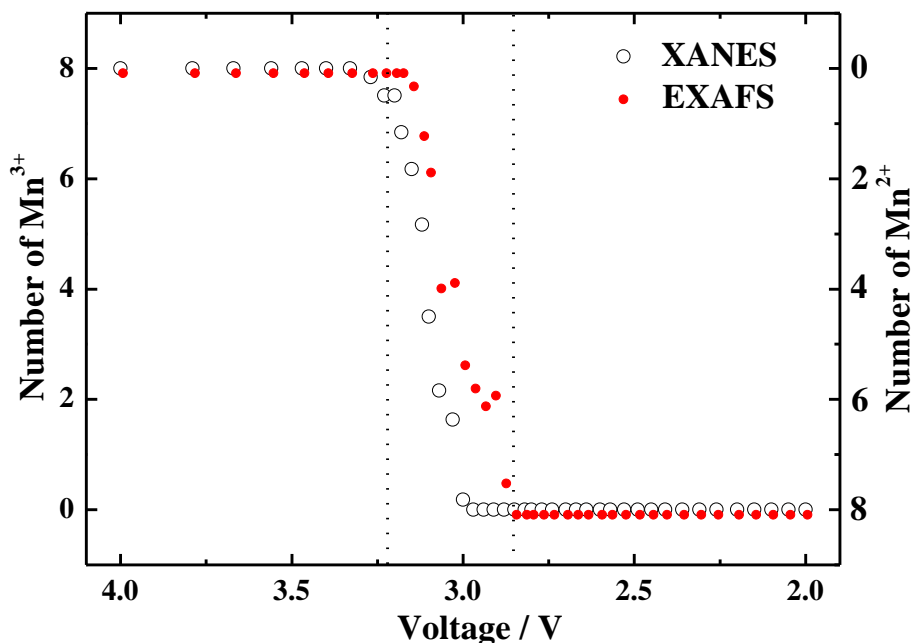


Figure 2.14 Voltage evolution of Mn³⁺ and Mn²⁺ numbers in Mn12 obtained from EXAFS and XANES during the first discharging.

3.3 – 2.8 V, the Mn³⁺ → Mn²⁺ reduction quickly takes place at eight Mn³⁺ sites, while the electrochemical reduction of Mn12 in solution occurs in a stepwise manner over a wide potential range.^[25, 26] This solid-state electrochemical reaction of Mn12 toward the super-reduced species means that the reduction of one Mn³⁺ site does not affect other sites in the solid state.^[26] This type of ‘shielding’ can be rationalized by the presence of close contacts between the reduced sites and the counter cations (Li⁺), in addition to a stabilization of the reduced species in a dielectric field of solids. In the range below 2.8 V, there is no redox change in the Mn ions, though a half of the battery capacity is obtained.

2.3.5. Conclusions

In situ XAFS spectroscopy has revealed the evolution of the oxidation state, and the local structure of Mn ions in the Mn12 molecule in the battery reaction. The source of the large capacity of the Mn12 MCBs is clearly shown; one half is from the redox change in the Mn ions, but the other half is not. We will discuss this in Chapter 3. The valence and structural analysis of Mn12 during charging/discharging indicated a conversion between Mn³⁺ and Mn²⁺ in the Mn12

skeleton. The solid-state electrochemistry was found to prepare the super-reduced species of Mn12 better than the conventional solution electrochemistry.

2.4. *In situ* XAFS studies of PMo12 MCBs

2.4.1. Charging/discharging curves of PMo12 MCBs

Figure 2.15 shows the charging/discharging curves of PMo12 MCBs for *in situ* XAFS measurements at a constant load current of 1 mA in the voltage range of 1.5 – 4.0 V. In the first charging process (black curve), the voltage quickly increases from the initial value (ca. 3.4 V) to 4.0 V. It is likely that these pristine batteries are nearly in the charged state. The first discharging of the PMo12 MCBs (red curve) indicates a gradual voltage decrease, and a high battery capacity of ca. 270 Ah/kg at 1.5 V. This value is similar to the reported one for the POMs previously.^[27, 28] The second charging process (green curve) exhibits a gradual voltage increase up to ca. 4.0 V, indicating a capacity of 230 Ah/kg. The second discharging curve (blue curve) is very similar to the first one (red), although the capacity is slightly decreased. This could be rationalized by a loose packing of the cathode and the anode in the battery cell, so that the capacity of the second discharging decreased. This *in situ* cell shows the same

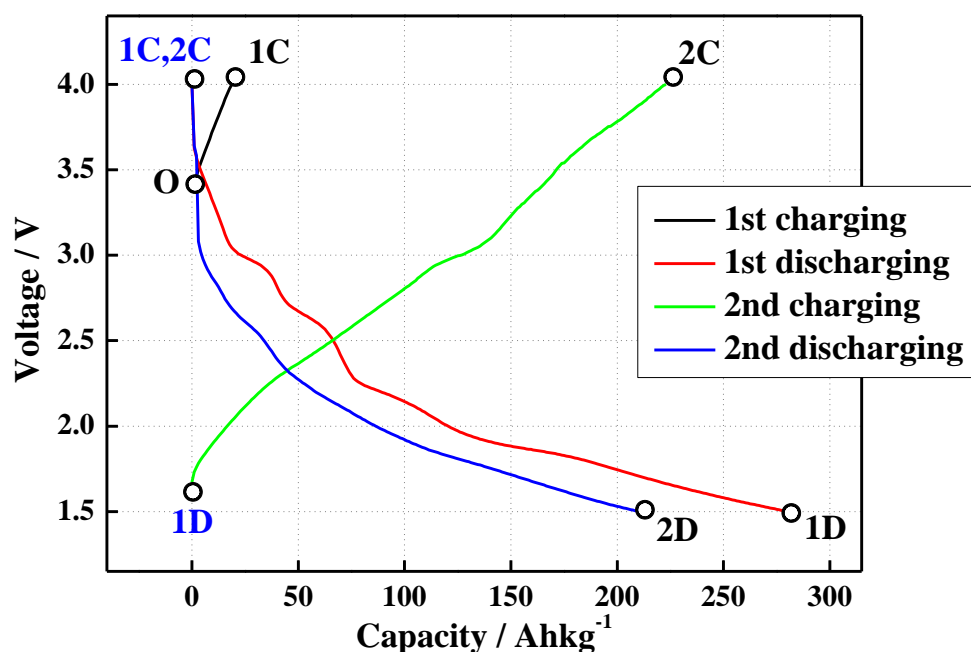


Figure 2.15 Charging/discharging curves of PMo12 MCBs. The labels, **O**, **1C**, **1D**, **2C** and **2D**, indicate the characteristic samples in the first two cycles of the battery reaction.

performance, as is found in the experiments with the coin cells.

2.4.2. *In situ* XANES analyses

Figure 2.16 shows the normalized Mo *K*-edge XANES spectra recorded during the measurements of the first charging (black curves), the first discharging (red), the second charging (green), and the second discharging (blue) (see Fig. 2.15). Figure 2.17 shows the XANES spectra for the first discharging and second charging processes. They exhibit a systematic spectral change; there is a clear shift of the absorption curves to lower energies with discharging, while the curve returns back to the original after charging. It is notable that these spectra indicate a shoulder around 20010 eV in the pre-edge region, which appears/disappears in the charging/discharging processes, respectively. This structure is well known to be characteristic of the presence of a Mo=O bond for a formally dipole forbidden $1s \rightarrow 4d$ excitation to anti-bonding orbitals directed principally along the Mo=O bond, and is ascribable to the Mo=O bonds located outside the PMo12 molecule.^[29, 30] The appearance and disappearance of this structure in the battery reaction indicate the presence and absence of the Mo=O bond, respectively.

Mo *K*-edge XANES absorption edge energies have been utilized to determine the valence of molybdenum.^[31-34] Figure 2.18 shows a linear relationship between the Mo oxidation state and the X-ray absorption edge energy for the reference materials, metal Mo, MoO₂, TBA₃PMo12, where the edge energy is defined as that at which the intensity reaches to 60 % of the absorption peak-top. By using this relation, N_v of the Mo ions in PMo12 was obtained. The results are shown in Fig. 2.19, where the values of N_v are plotted as a function of the battery voltage V (see Fig. 2.15).

Absence of the data in the voltage range of 4.0 – 3.3 V in the second discharging process is caused by interruption of incident X-ray due to a beam injection in PF-AR. The initial value of N_v is ca. 6 before the first charging, which agrees with the assumption that [PMo12]³⁻ consists of twelve Mo⁶⁺. However, this value exhibits no change during the first charging, indicating that the as prepared battery is in the charged state. In the first discharging, N_v exhibits a slight decrease from the initial

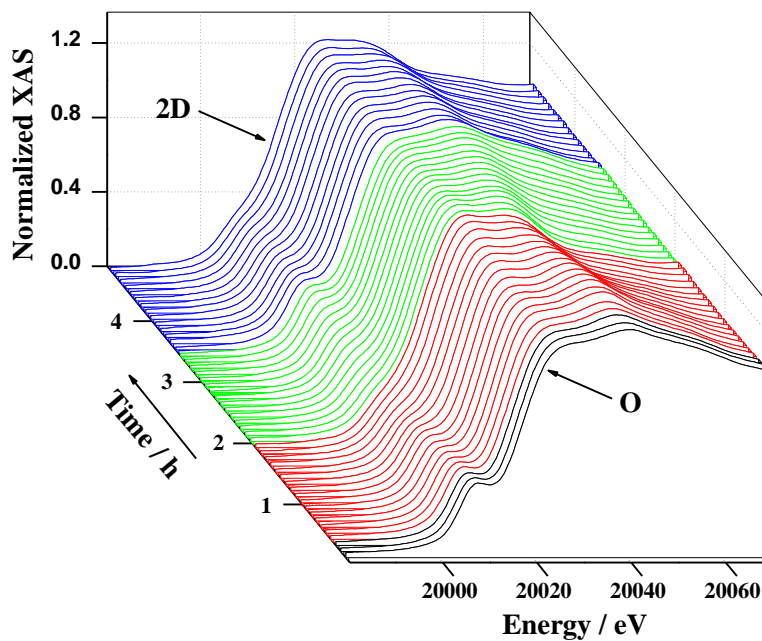


Figure 2.16 Evolution of the normalized *in situ* Mo K-edge XANES spectra for PMo12 MCBs during the first two cycles.

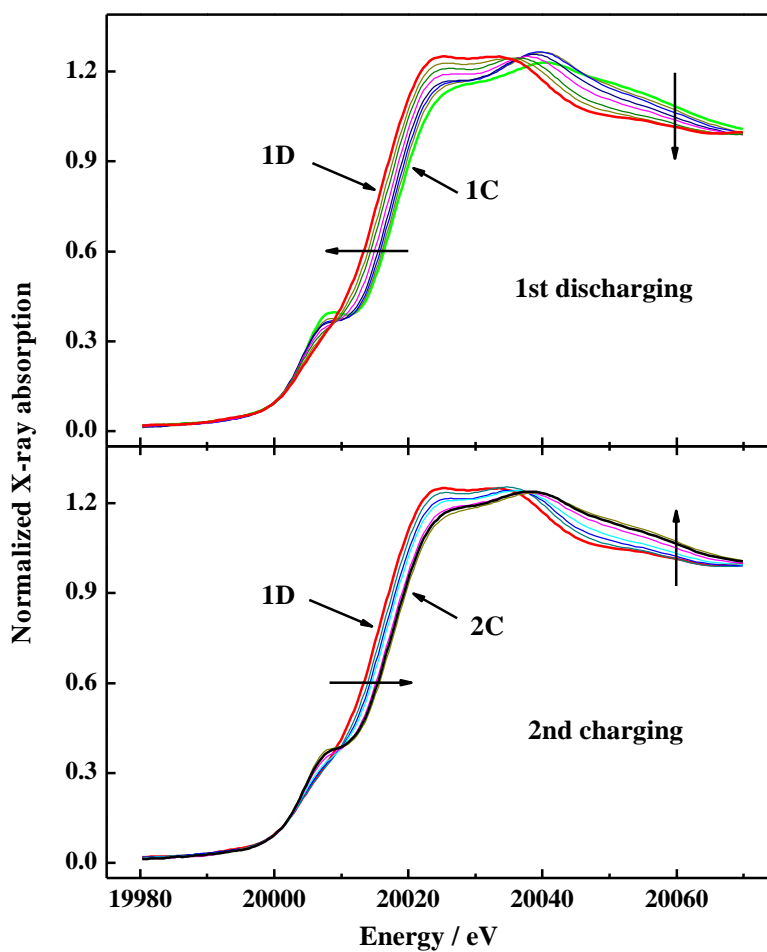


Figure 2.17 Mo K-edge XANES spectra for PMo12 MCBs in the first discharging and second charging.

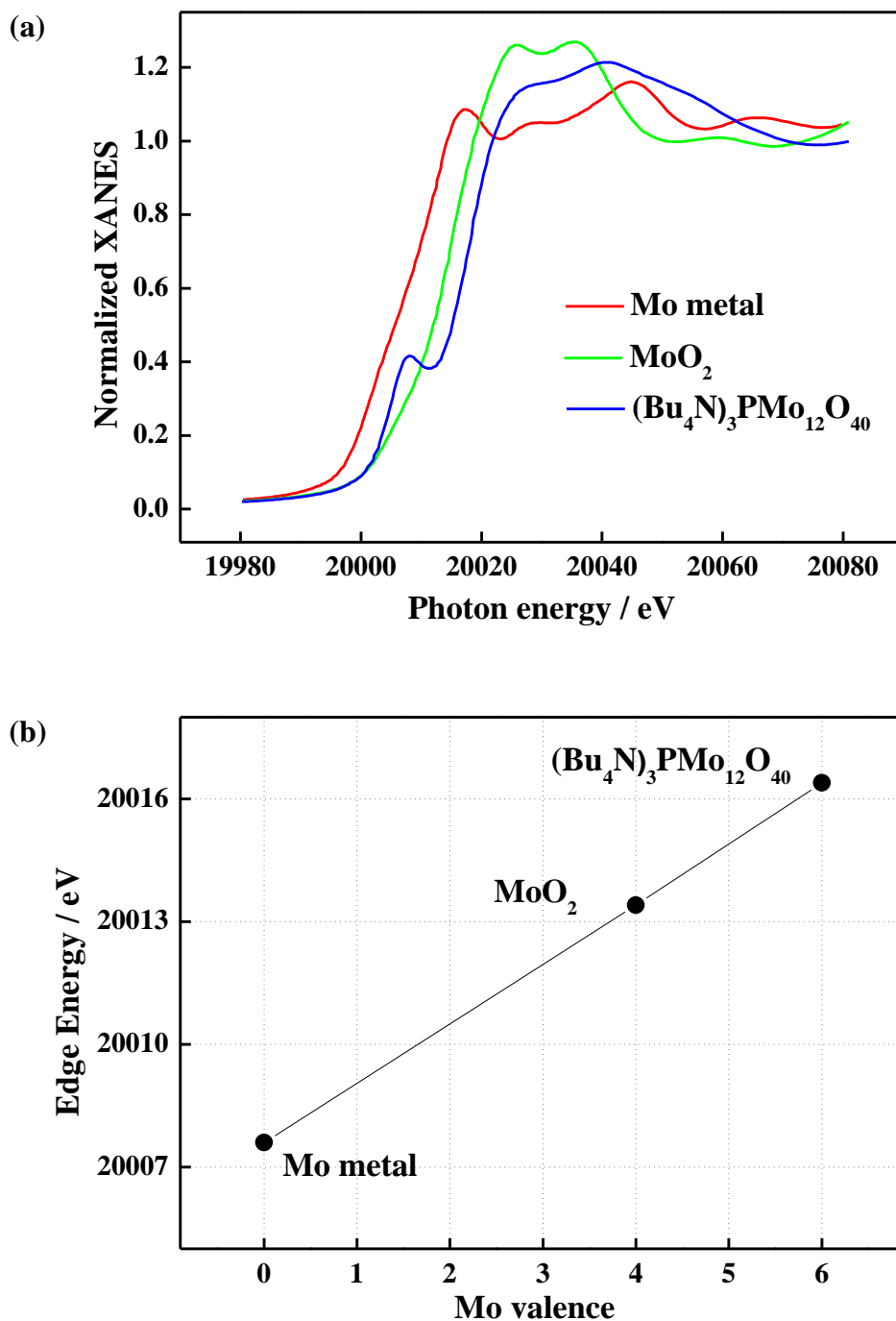


Figure 2.18 Normalized Mo *K*-edge XANES spectra (a) and Mo valence vs. edge energy (b) for the reference materials Mo metal, MoO₂, and (Bu₄N)₃PMo₁₂O₄₀.

value in the range of 4.0 – 3.0 V, which is consistent with a small capacity in this voltage range (see Fig. 2.15). In the range of 3.0 – 1.5 V, N_v shows a quick decrease to 4.0. This voltage range of the valence change roughly agrees with the theoretical value (3.5 – 2.0 V) calculated from the redox potential of PMo₁₂.^[35] The second charging increases the value of N_v from 4.0 to 5.7, and the second discharging

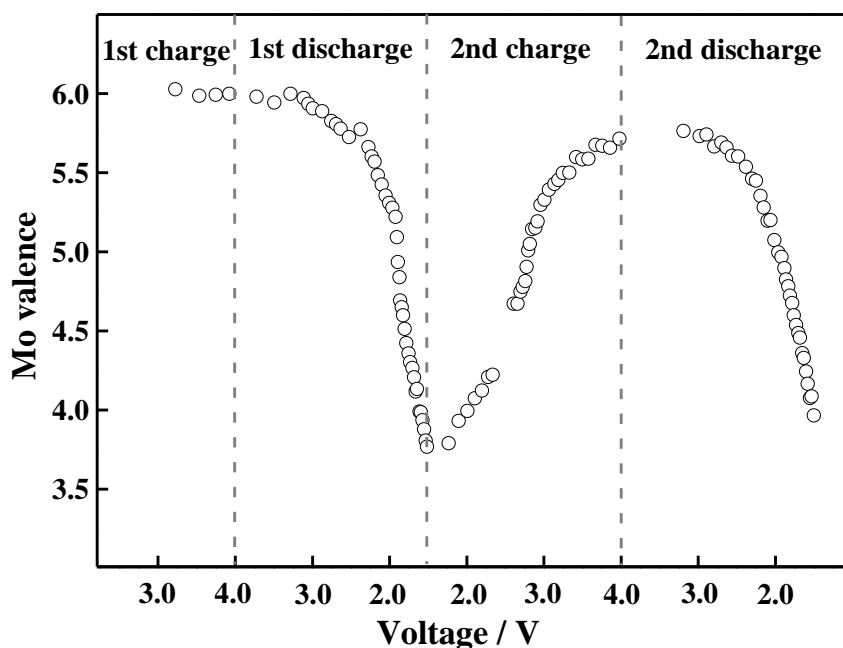


Figure 2.19 Averaged Mo valence of PMo12 in the PMo12 MCBs as a function of cell voltage V (V).

decreases it reversibly. The N_v value change by 2.0 in the first discharging indicates that all of the twelve Mo^{6+} ions in PMo12 are reduced to Mo^{4+} . In the other words, one PMo12 molecule can store twenty four electrons. This value is consistent with the observed battery capacity of ca. 270 Ah/kg (see Fig. 2.15).

2.4.3. *In situ* EXAFS analyses

EXAFS analyses were performed in order to obtain the structural information of the PMo12 molecule during charging/discharging. Figure 2.20 shows the Fourier transform (FT) spectra of the k^3 -weighted data (k range is around 2.0 – 12.0 \AA^{-1}) for the samples denoted by **O**, **1C**, **1D**, **2C**, and **2D** in Fig. 2.15. These spectra indicate the radial atomic distribution around Mo. The as-prepared sample **O** exhibits four main peaks at 1.1, 1.6, 2.3, and 3.2 \AA , as indicated by the arrows. In the previous EXAFS studies of PMo12,^[36] these four peaks were assigned to Mo=O (1.7 \AA) and two kinds of Mo-O (ca. 1.9 and 2.4 \AA) bonds, and Mo-Mo (3.4 \AA) distance, respectively, as indicated in the local structure of $[\text{PMo12}]^{3-}$ (see Fig. 2.24).^[37] The curve of **1C** is nearly the same as that of **O**. After the first discharging, **1D** exhibits a different spectrum; the peaks at 1.1 and 3.2 \AA become

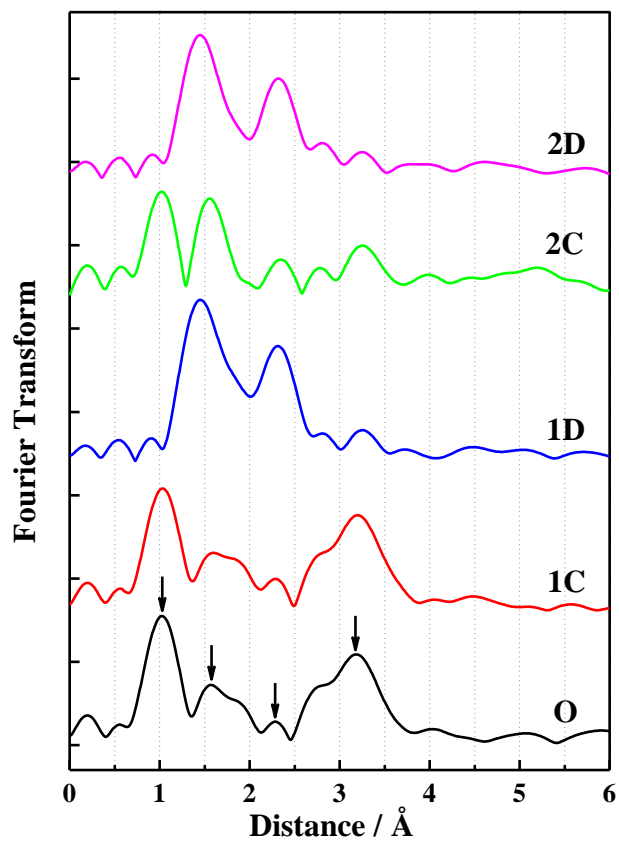


Figure 2.20 The Fourier transforms of the Mo *K*-edge EXAFS spectra for O, 1C, 1D, 2C and 2D.

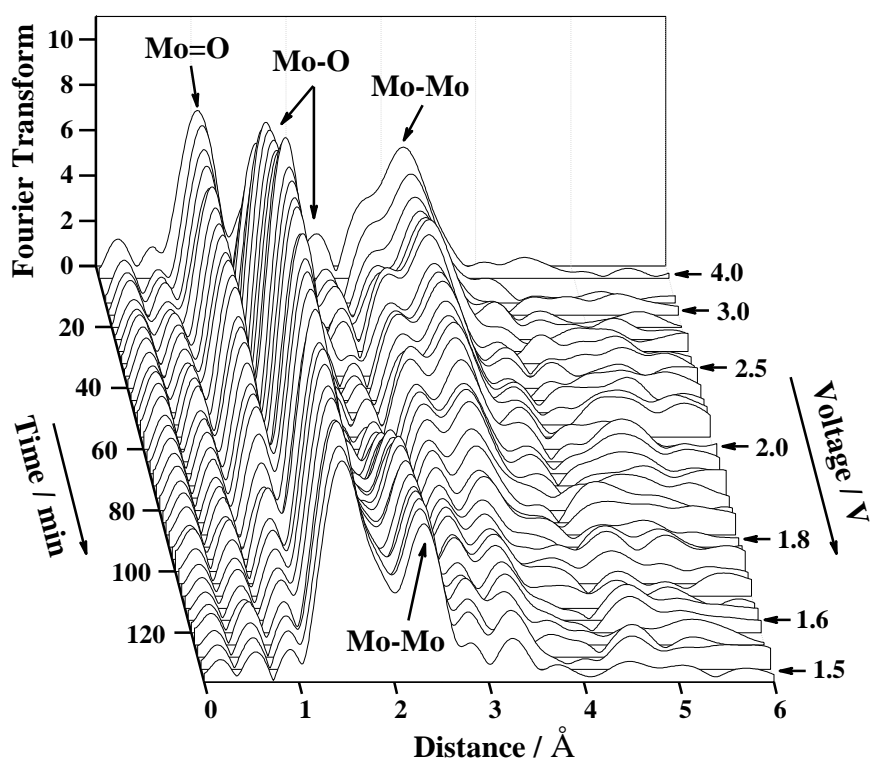


Figure 2.21 Evolution of the fourier transforms of the Mo *K*-edge EXAFS spectra in the first discharging.

very small, and those at 1.6 and 2.3 Å significantly increase. After the second charging, the sample **2C** exhibits the initial four peaks, though the peak intensity at 3.2 Å becomes slightly smaller, and the peak at 1.6 Å becomes narrower, compared with those in **1C**. After the second discharging, the curve of **2D** is nearly the same as that of **1D**. This indicates a nearly reversible structural change of the PMo12 molecule during the charging/discharging processes.

Figure 2.21 shows the evolution of the FT spectra in this first discharging (reduction) process from **1C** to **1D**. It is clear that the peaks at 1.1 and 3.2 Å swap the intensities at 1.6 and 2.3 Å, as the voltage V decreases from 4.0 V. The decrease of the peak at 1.1 Å, and increase of that at 1.6 Å are ascribed to the transformation from Mo=O double- to Mo-O single-bond, as also indicated by the XANES results in the discharging process (see Fig. 2.16). The other intensity swapping between the peaks at 3.2 and 2.3 Å is probably caused by a shortening of Mo-Mo distance, as described later.

We carried out curve-fitting for the *in situ* EXAFS spectra, using the parameters of the backscattering amplitudes and the phase shifts of the appropriate Mo-O and

Table 2.1 Interatomic distances and coordination numbers for Mo-O and Mo-Mo shells in **O**, **1C**, **1D**, **2C**, and **2D**.

Shell		O	1C	1D	2C	2D
Mo=O (1.1 Å)	R / Å	1.71	1.71	1.66	1.71	1.68
	CN	1.02	1.01	0.31	0.83	0.30
Mo-O 1 (1.6 Å)	R / Å	1.86	1.87	1.92	1.87	1.95
	CN	1.99	2.12	1.35	1.63	1.84
Mo-O 2 (1.6 Å)	R / Å	2.01	2.02	2.06	2.00	2.10
	CN	1.96	2.12	3.17	1.95	2.41
Mo-O (2.3 Å)	R / Å	2.43	2.40	-	2.45	-
	CN	0.81	1.18	-	0.51	-
Mo-Mo (2.3 Å)	R / Å	-	-	2.63	2.58	2.62
	CN	-	-	0.88	0.16	0.75
Mo-Mo (3.2 Å)	R / Å	3.49	3.49	3.53	3.49	3.59
	CN	3.59	3.59	0.46	1.96	0.16

Distance values in the column of shell correspond to curve-fitted peaks in EXAFS spectra. Two shell analyses were used for Mo-O (1.6 Å), denoted as Mo-O 1 and Mo-O 2. R: interatomic distance, CN: coordination number.

Table 2.2 Energy shifts ΔE and Debye-Waller factors σ^2 for Mo-O and Mo-Mo shells in **O**, **1C**, **1D**, **2C**, and **2D**.

	Mo=O (1.1 Å)	Mo-O 1 (1.6 Å)	Mo-O 2 (1.6 Å)	Mo-O (2.3 Å)	Mo-Mo (2.3 Å)	Mo-Mo (3.2 Å)
ΔE / eV	0	8	8	8	3.4	0
$\sigma^2 / 10^{-2} \text{Å}^2$	-0.967	-0.326	-0.046	0.627	0.155	-0.014

Distance values in the column of shell correspond to curve-fitted peaks in the EXAFS spectra. Two shell analyses were used for Mo-O (1.6 Å), denoted as Mo-O 1 and Mo-O 2.

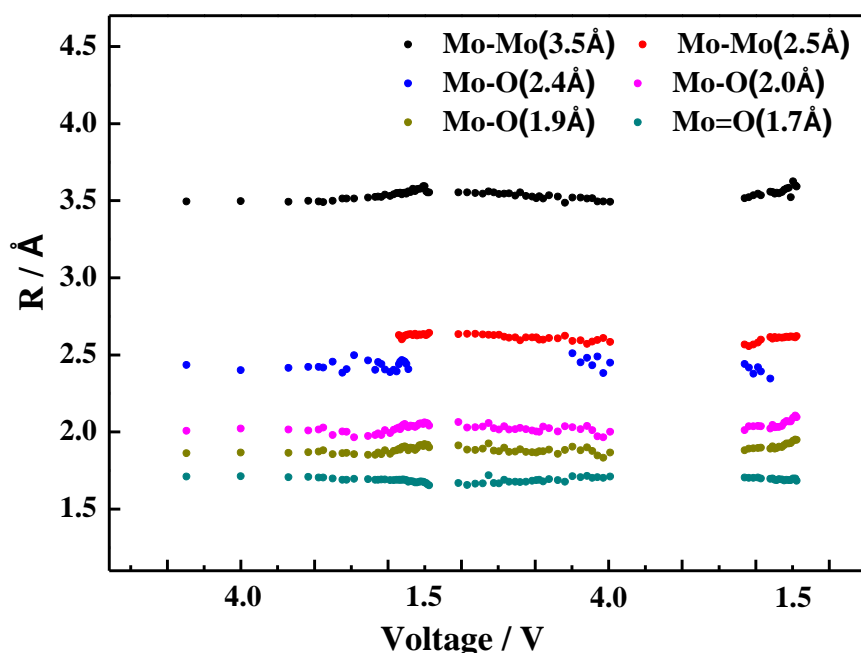


Figure 2.22 Interatomic distances in the EXAFS curve-fitting of PMo12 in the PMo12 MCBs as a function of cell voltage (V).

Mo-Mo shells, which were obtained for the reference materials, MoO₂ and TBA₃PMo₁₂. The Mo-O peak at 1.6 Å was analyzed by using two Mo-O shells with the distances of 1.9 and 2.0 Å (see Table 2.1), while the other peaks were analyzed by the one-shell model. The coordination numbers and interatomic distances were obtained as fitting variables for all the shells used in the curve-fittings, while the Debye-Waller factors σ and the energy shifts ΔE were fixed (Table 2.2). The results are shown in Table 2.1 for **O**, **1C**, **1D**, **2C** and **2D**. Figure 2.22 shows the evolution of all the interatomic distances used in the curve-fitting. These interatomic distances exhibit no significant changes. Figure 2.23 shows the evolution of the coordination

numbers for the shells in the first discharging and second charging. The data are rather scattered, because the data quality of some EXAFS spectra were not good, due to inhomogeneous reactions. Coordination number is an indicator for the number of neighboring atoms. Actually, the summation of the coordination numbers for all the M=O and M-O shells in **O** and **1C** becomes ca. 6, which is consistent with six-coordinated Mo (see Table 2.1). As shown in Figs. 2.23(a) and (b), the summation of the coordination numbers for the Mo-O shells (1.9 and 2.0 Å) slightly increases during the discharging, while those for Mo=O (1.7 Å) and Mo-O (2.4 Å) approach to zero. These tendencies imply that all the Mo-O interatomic distances become ca. 2.0 Å, accompanied with the disappearance of Mo=O. Figure 2.22(c) indicates the evolution of the coordination numbers for two kinds of the Mo-Mo distances. In the discharging process, the coordination number for the Mo-Mo distance of 3.4 Å decreases, while that for 2.6 Å increases. These results suggest that the Mo-Mo distance shortens from 3.4 to 2.6 Å, that is, the Mo-Mo bond is formed during discharging.

2.4.4. Model structure of the reduced PMo12

The EXAFS analysis suggested that the distances of Mo-O and Mo-Mo become ca. 2.0 and 2.6 Å, respectively, after discharging. Using this information, we estimated a local structure of the 24-electron reduced PMo12 molecule (denoted as [PMo12]²⁷⁻), as shown in Fig. 2.24(b). In this structure, all the Mo-O distances are set to be 1.9 – 2.0 Å, and the nearest Mo-Mo are 2.6 Å to make a single metal-metal bond. Assuming that the [PMo12]²⁷⁻ molecule has the highest symmetry, we constructed a model structure by assembling the local structure (see Fig. 2.24 (b)), as shown in Fig. 2.24 (c). This structure is slightly reduced in size from the original one, and this feature is similar to a partial structure of MoO₂ including a single Mo-Mo bond.^[19] Then, using the expected structure of [PMo12]²⁷⁻, we simulated the EXAFS spectra of this molecule by using the backscattering amplitudes and the phase shifts for appropriate Mo-O and Mo-Mo shells. They are calculated from the model structure in Fig. 2.24 (c) using the *ab initio* multiple scattering code FEFF 8.4.^[20] The simulated EXAFS spectrum is shown in Fig. 2.25 with the experimental spectra for the fully-discharged

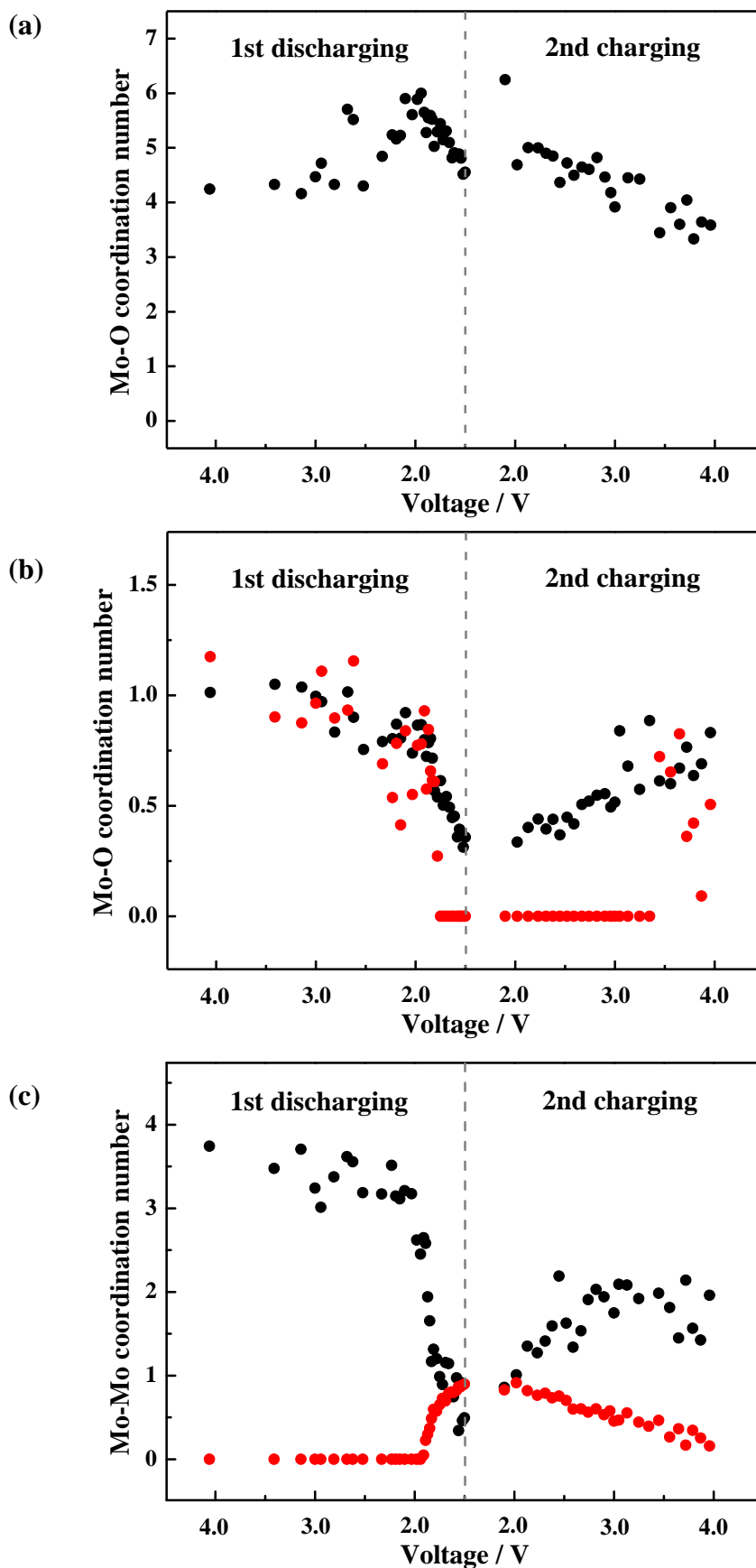


Figure 2.23 Evolution of coordination numbers for (a) the summation of two Mo-O shells (1.9 and 2.0 Å), (b) Mo=O (1.7 Å, black) and Mo-O (2.4 Å, red) shells, and (c) Mo-Mo (2.4 Å, red) and Mo-Mo (3.5 Å, black) shells used in EXAFS.

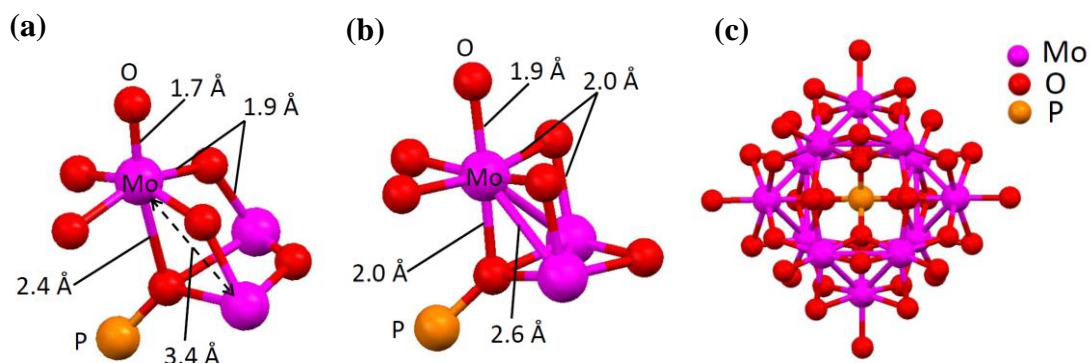


Figure 2.24 Local structures of (a) $[\text{PMo}_{12}]^{3-}$, (b) $[\text{PMo}_{12}]^{27-}$, and model structures of (c) $[\text{PMo}_{12}]^{27-}$.

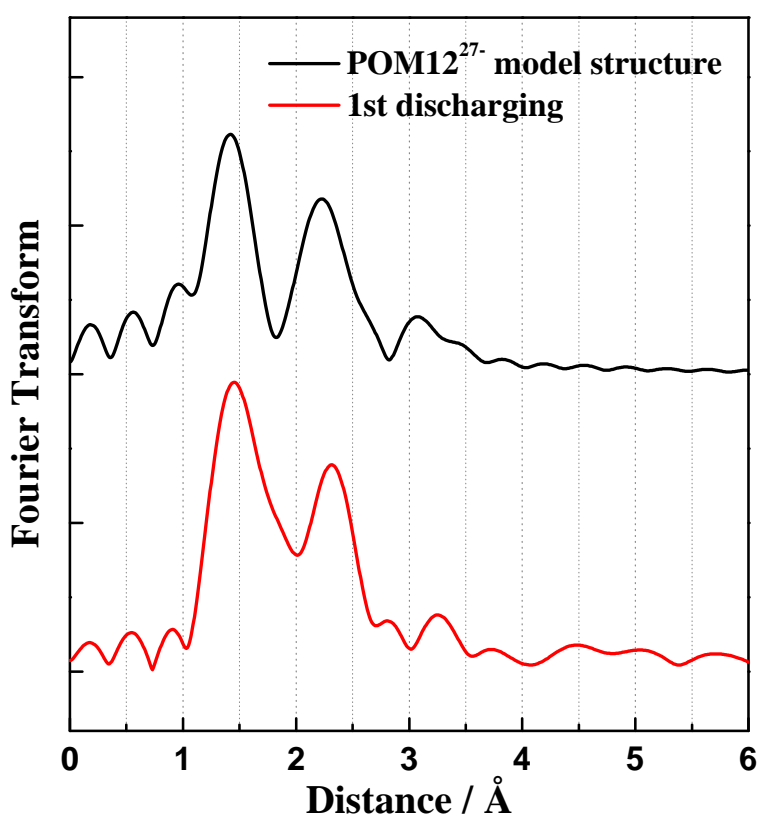


Figure 2.25 Simulated Mo K -edge EXAFS spectra for $[\text{PMo}_{12}]^{27-}$ model structure (black) and experimental Mo K -edge EXAFS spectra for **1D** (red).

state (**1D**). The simulation can reproduce the features of the experimental spectra very well. It is reasonable to conclude that the model structure is highly possible to explain the structure of $[\text{PMo}_{12}]^{27-}$.

2.4.5. Electron sponge behavior of PMo12

The XANES analysis indicates that the highly-reduced species, $[\text{PMo}_{12}]^{27-}$, which is reduced from $[\text{PMo}_{12}]^{3-}$ by twenty four electrons, is obtained after

discharging. In the range of 3.0 – 1.5 V, the reduction from Mo^{6+} to Mo^{4+} takes place at twelve Mo^{6+} sites, though it is well-known that only two- or three-electron reductions occur for PMo12 in this voltage range in the solution electrochemistry.^[35] The present solid-state electrochemical reaction of PMo12 means that the reduction of one Mo^{6+} site does not affect the other Mo ion sites in the solid state, probably due to close contacts between the reduced sites and the counter cations (Li^+), and that the highly-reduced species are stabilized in the dielectric field of the solid.^[26] PMo12 can be regarded as a molecular electron-sponge with the volume change suggested by the EXAFS analyses.^[38, 39] This kind of electron-sponge behavior may be common in the solid-state electrochemistry, such as in the battery reactions, as ten-electron redox reactions also take place for the Mn12 clusters in the Mn12 MCBs.

Besides the 10 wt% PMo12 MCBs, the charging-discharging performances were tested for the coin cell batteries, in which the cathode includes a 30 wt% of the active material, $\text{TBA}_3\text{PMo12}$. The charging/discharging curves for the 30 wt% POM MCBs show that the first discharging capacity becomes less than one-third of that in the 10 wt% battery (Fig. 2.26). We measured *in situ* XAFS of the 30 wt% POM MCBs to reveal this active-material ratio dependence on the battery performances. Figure 2.27 shows the charging/discharging curves during *in situ* XAFS measurements. This behaviour is almost similar to that of the coin cell battery, although the capacity decreases in the second discharging. Normalized *in situ* Mo *K*-edge XANES spectra exhibit slight spectral changes between charged and discharged states (Fig. 2.28). This behavior is very different from that of 10 wt% POM MCBs (see Fig. 2.16). As shown in Fig. 2.29, the values of the averaged Mo valences N_v , which are calculated from the edge energies in Fig. 2.28, decrease from ca. 6.0 to 5.0 in the discharging process, and then return back to the original value of 6.0 in the charging process. These results indicate an approximately 11-electron reduction per one PMo12 molecule in discharging, and the obtained theoretical capacity of 115 Ah/kg is comparable to a small battery capacity of ca. 70 Ah/kg (Fig. 2.27). Impedance measurements on both the 10 and 30 wt% POM-MCBs (Fig. 2.30) demonstrate that the charge-transfer resistance for the 30 wt% MCBs is higher than that for the 10 wt% ones. Since the

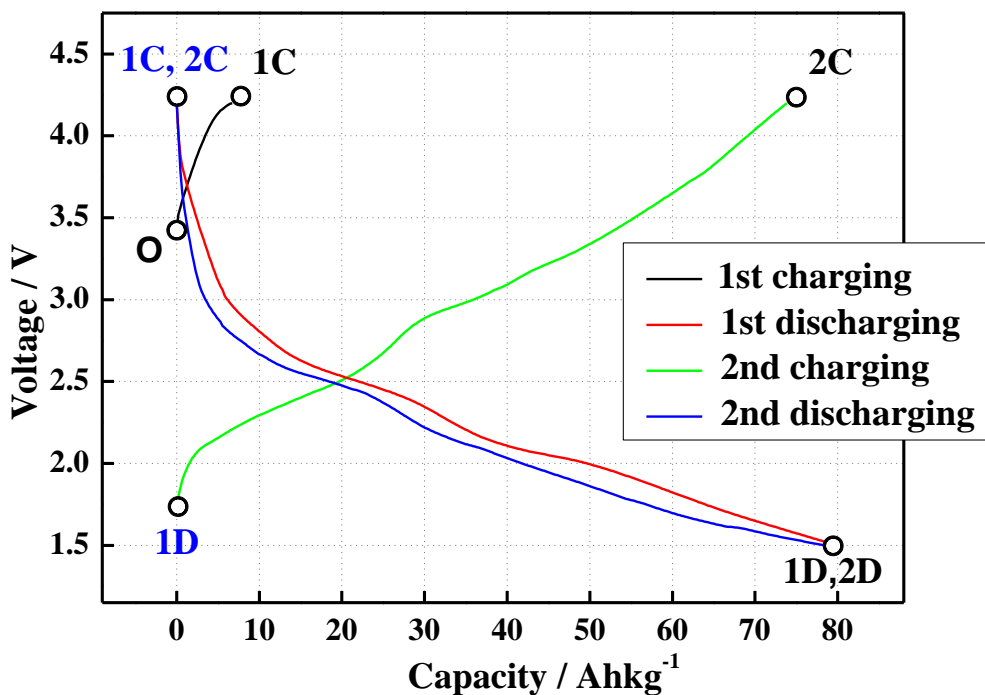


Figure 2.26 Charging and discharging curves for the first two cycles of 30 wt% PMo₁₂/Li MCBs using the coin cell battery.

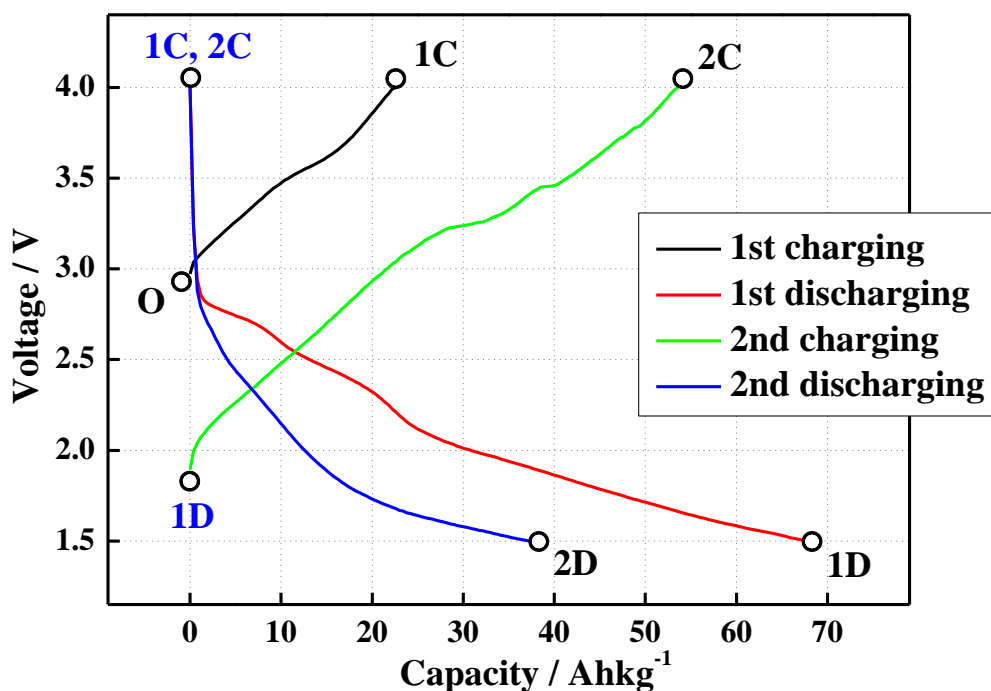


Figure 2.27 Charging and discharging curves of 30 wt% PMo₁₂/Li MCBs during XAFS measurements.

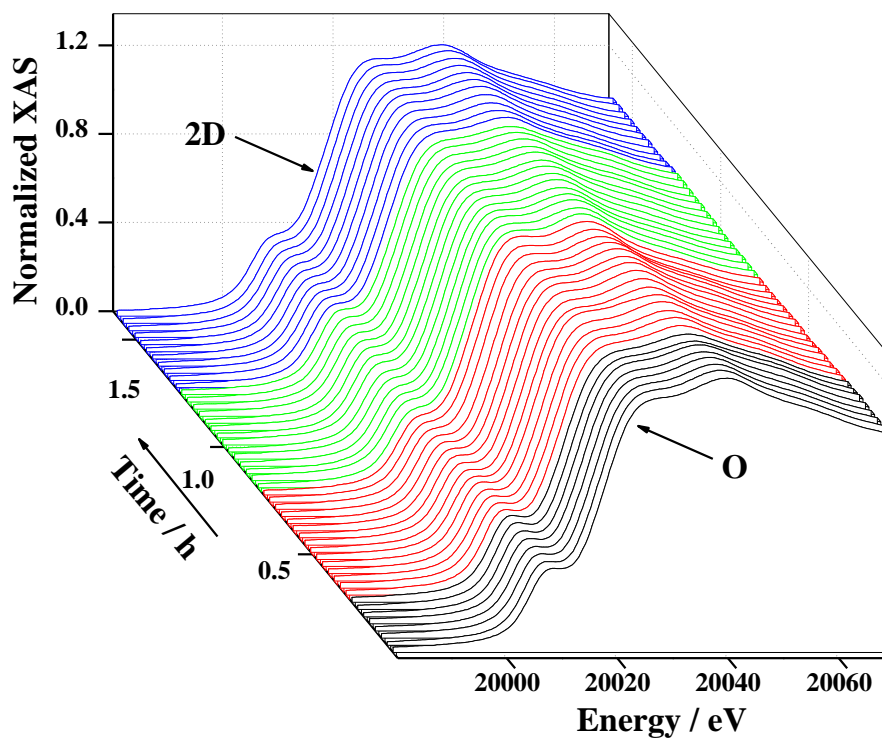


Figure 2.28 Evolution of the normalized *in situ* Mo K-edge XANES spectra for 30 wt% PMo12 MCBs during the first two cycles.

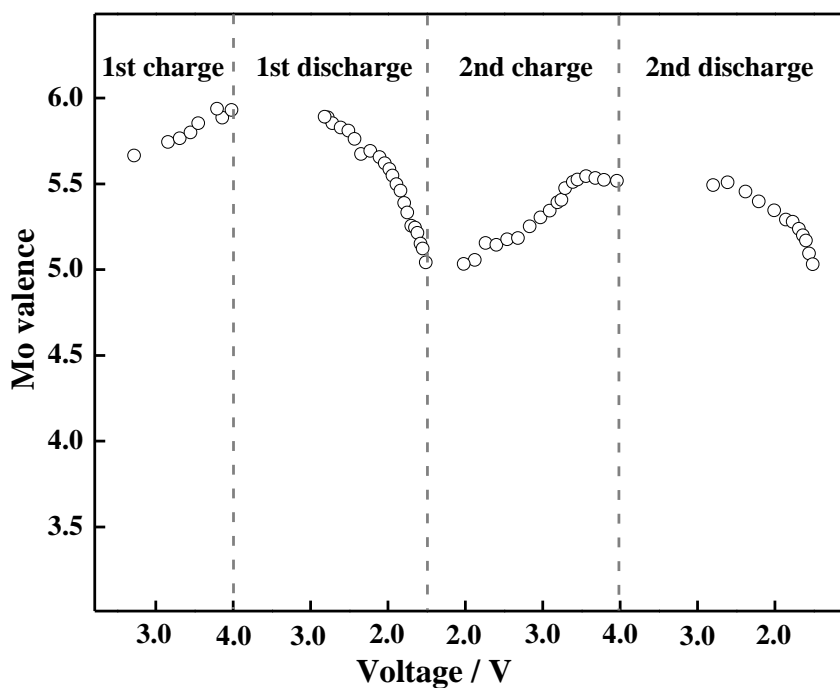


Figure 2.29 Averaged Mo valence of PMo12 in the 30 wt% PMo12 MCBs as a function of cell voltage (V).

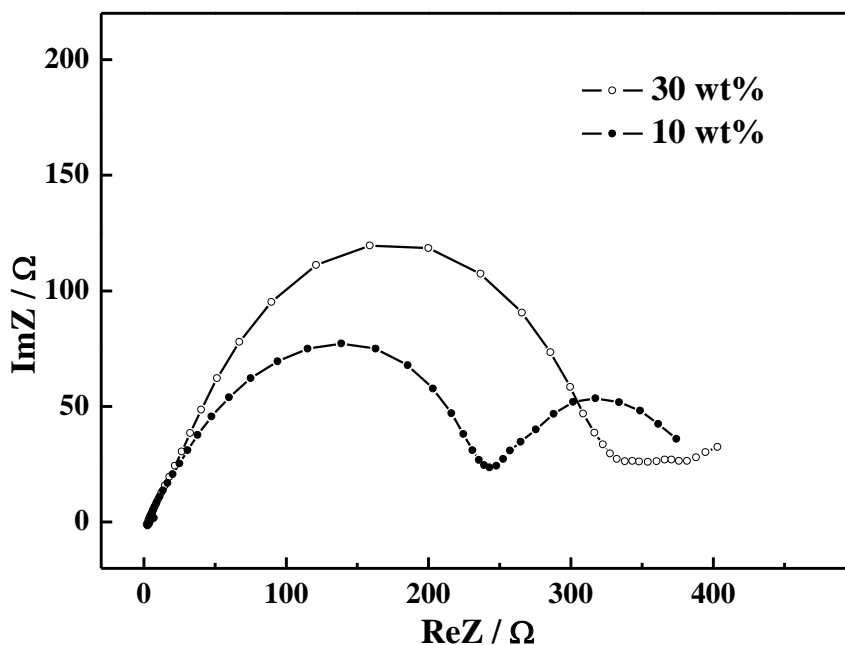


Figure 2.30 Impedance spectra of the 10 and 30 wt% PMo12/Li MCBs using the coin cell batteries. (Frequency range: 200 kHz – 10 mHz)

PMo12 is an insulator, the small capacity of the 30 wt% one is caused by a poor electron transfer between the PMo12 and the carbon electrode due to a ratio increase of the PMo12. To achieve a high capacity in MCBs with high ratios of active materials, it is necessary to develop a system with effective/smooth electron transfer between the cluster molecules and the electrode.

2.4.6. Conclusions

In situ Mo *K*-edge XAFS measurements on POM-MCBs revealed the evolution of the oxidation state and the local structure of Mo ions of the PMo12 molecule in the battery reaction. The large discharging capacity is explained by twenty-four electron reductions of the PMo12 molecule, in which the reduction from Mo⁶⁺ to Mo⁴⁺ takes place at twelve Mo⁶⁺ sites, accompanied by a shrinking in molecular size. These results suggest that POMs are promising cathode active materials for high-performance rechargeable batteries.

2.5. Summary

In situ XAFS studies of both Mn12Pe^t and PMo12 MCBs were carried out to investigate the reaction mechanism of MCBs comprehensively. The ten-electron

reduction of Mn₁₂ clusters in Mn₁₂Pe^t MCBs takes place in the limited voltage range, indicating that a half of the whole capacity is from the redox reaction of the Mn ions and the other comes from a physical effect. In contrast, the 24-electron reduction of PMo₁₂ can explain the whole capacity of this battery.

The *in situ* XAFS analysis suggested that reversible structural changes and super-reduction of molecular clusters occurred both in Mn₁₂Pe^t and PMo₁₂ MCBs. The super-reduction behavior can be rationalized by close contacts between the reduced metal ions and Li⁺ ions, and the presence of a dielectric field, which stabilizes the reduced metal ion sites in the molecular clusters. Using solid-state electrochemistry, we succeeded in preparing super-reduced molecular clusters, which cannot be obtained in conventional solution electrochemistry.

References

- [1] M. S. Islame, B. Ammundsen, D. J. Jones, J. Roziere, *Materials for Lithium-Ion Batteries*, eds. Julien, C.; Stoyanov, Z. Academic Publisher, Netherlands, **2000**, 279.
- [2] J. E. Penner-Hahn, *Coord. Chem. Rev.* **1999**, 190-192, 1101-1123.
- [3] S. Gross, M. Bauer, *Adv. Funct. Mater.* **2010**, 20, 4026-4047.
- [4] G. Bunker, *Introduction to XAFS*, Cambridge, **2010**.
- [5] J. J. Rehr, R. C. Albers, C. R. Natoli, E. A. Stern, *Phys. Rev. B* **1986**, 34, 4350-4353.
- [6] D. C. Koningsberger, B. L. Mojet, G. E. van Dorssen, D. E. Ramaker, *Top. Catal.* **2000**, 10, 143-155.
- [7] J. J. Rehr, R. C. Albers, *Rev. Mod. Phys.* **2000**, 72, 621-654.
- [8] H. Yoshikawa, S. Hamanaka, Y. Miyoshi, Y. Kondo, S. Shigematsu, N. Akutagawa, M. Sato, T. Yokoyama, K. Awaga, *Inorg. Chem.* **2009**, 48, 9057-9059.
- [9] N. E. Sung, Y. K. Sun, S. K. Kim, M. S. Jang, *J. Electrochem. Soc.* **2008**, 155, A845-A850.

- [10] A. Braun, S. ShROUT, A. C. Fowlks, B. A. Osaisai, S. Seifert, E. Granlund, J. Cairns, *J. Synchrotron Radiat.* **2003**, *10*, 320-325.
- [11] K. W. Nam, W. S. Yoon, K. Zaghbi, K. Y. Chung, X. Q. Yang, *Electrochem. Commun.* **2009**, *11*, 2023-2026.
- [12] N. E. Chakov, L. N. Zakharov, A. L. Rheingold, K. A. Abboud, G. Christou, *Inorg. Chem.* **2005**, *44*, 4555-4567.
- [13] T. Lis, *Acta Crystallogr. Sect. B* **1980**, *36*, 2041-2046.
- [14] C. Sanchez, J. Livage, J. P. Launay, M. Fournier, Y. Jeannin, *J. Am. Chem. Soc.* **1982**, *104*, 3194-3202.
- [15] A. Braun, S. ShROUT, A. C. Fowlks, B. A. Osaisai, S. Seifert, E. Granlund, J. Cairns, *J. Synchrotron. Rad.* **2003**, *10*, 320-325.
- [16] T. Taguchi, T. Ozawa, H. Yashiro, *Physica Scripta*, **2005**, *T115*, 205-206.
- [17] A. Ankudinov, B. Ravel, J. Rehr, S. Conradson, *Phys. Rev. B* **1998**, *58*, 7565-7576.
- [18] EXAFSH Version 2.1, *EXAFS Analysis Program*, T. Yokoyama, H. Hamamitsu, T. Ohta, The University of Tokyo, **1994**.
- [19] V. Eyert, R. Horny, K. H. Hock, S. Horn, *J. Phys.: Condens. Matter.* **2000**, *12*, 4923-4946.
- [20] A.L. Ankudinov, B. Ravel, J. J. Rehr, S. D. Conradson, *Phys. Rev. B* **1998**, *58*, 7565-7576.
- [21] Ibarra-Palos, P. Strobel, O. Proux, J. L. Hazemann, M. Anne, M. Morcrette, *Electrochem. Acta.* **2002**, *47*, 3171-3178.
- [22] H. Yoshikawa, C. Kazama, K. Awaga, M. Sato, J. Wada, *Chem. Commun.* **2007**, *30*, 3169-3170.
- [23] A. Manceau, A. I. Gorshkov, V. A. Drits, *Am. Miner.* **1992**, *77*, 1113-1143.
- [24] R. Bagai, G. Christou, *Inorg. Chem.* **2007**, *46*, 10810-10818.
- [25] M. Soler, W. Wernsdorfer, K. A. Abboud, J. C. Huffman, E. R. Davidson, D. N. Hendrickson, G. Christou, *J. Am. Chem. Soc.* **2003**, *125*, 3576-3588.
- [26] L. Zhao, Z. Q. Xu, H. Grove, V. A. Milway, L. N. Dawe, T. S. M. Abedin, L. K. Thompson, T. L. Kelly, R. G. Harvey, D. O. Miller, L. Weeks, J. G. Shapter, K.

- J. Pope, *Inorg. Chem.* **2004**, *43*, 3812-3824.
- [27] M. L. Cantu, P. G. Romero, *Chem. Mater.* **1998**, *10*, 698-704.
- [28] B. M. Azumi, T. Ishihara, H. Nishiguchi, Y. Takita, *Electrochemistry* **2002**, *70*, 869-874.
- [29] F. Jalilehvand, B. S. Lim, R. H. Holm, B. Hedman, K. O. Hodgson, *Inorg. Chem.* **2003**, *42*, 5531-5536.
- [30] N. T. Shiju, A. J. Rondinone, D. R. Mullins, V. Schwartz, S. H. Overbury, V. V. Guliants, *Chem. Mater.* **2008**, *20*, 6611-6616.
- [31] J. Berry, G. M. Yaxley, A. B. Woodland, G. J. Foran, *Chemical Geology* **2010**, *278*, 31-37.
- [32] Macias, P. Malet, R. Paradinas, V. Rives, M. V. Villa, *Inorg. Chim. Acta.* **1999**, *288*, 127-133.
- [33] V. Safonova, B. Deniau, J.-M. M. Millet, *J. Phys. Chem. B* **2006**, *110*, 23962-23967.
- [34] J. Wienold, O. Timpe, T. Ressler, *Chem. Eur. J.* **2003**, *9*, 6007-6017.
- [35] K. Maeda, S. Himeno, T. Osakai, A. Saito, T. Hori, *J. Electroanal. Chem.* **1994**, *364*, 149-154.
- [36] J. Wienold, O. Timpe, T. Ressler, *Chem. Eur. J.* **2003**, *9*, 6007-6017.
- [37] S. Liu, C. Wang, H. Zhai, D. Li, *J. Mol. Struct.* **2003**, *654*, 215-221.
- [38] H. Brunner, H. Cattey, W. Meier, Y. Mugnier, A. C. Stückl, J. Wachter, R. Wanninger, M. Zabel, *Chem. Eur. J.* **2003**, *9*, 3796-3802.
- [39] M. Bencharif, O. Cador, O.H. Cattey, A. Ebner, J. F. Halet, S. Kahlal, W. Meier, Y. Mugnier, J. Y. Saillard, P. Schwarz, F. Z. Trodi, J. Wachter, M. Zabel, *Eur. J. Inorg. Chem.* **2008**, *12*, 1959-1968.

Chapter 3

Electrical double layer effect of Mn12 MCBs studied by cyclic voltammetry and solid-state ^7Li NMR

3.1. Introduction

Electrical double layer capacitors (EDLCs), so-called supercapacitors, have recently attracted a considerable amount of attention as promising energy storage devices, due to a large energy density and a long life cycle.^[1-5] An electrical double layer (EDL) is usually formed at an electrode/electrolyte interface, where electric charges are accumulated on the electrode surface, and ions with opposite charges are arranged on the surface of the electrolyte side (Fig. 3.1).^[6]

As described in Chapter 2, the capacity of ca. 100 Ah/kg in 2.8 – 4.0 V of the Mn12 MCB is assigned to a multi-electron redox of Mn ions of Mn12, while the origin of ca. 100 Ah/kg in the range of 2.0 – 2.8 V remained unclear. In this chapter, we tried to investigate the capacity between 2.0 and 2.8 V, which is probably caused by the formation of EDL, using cyclic voltammetry (CV) measurements and nuclear magnetic resonance (NMR) spectroscopy.

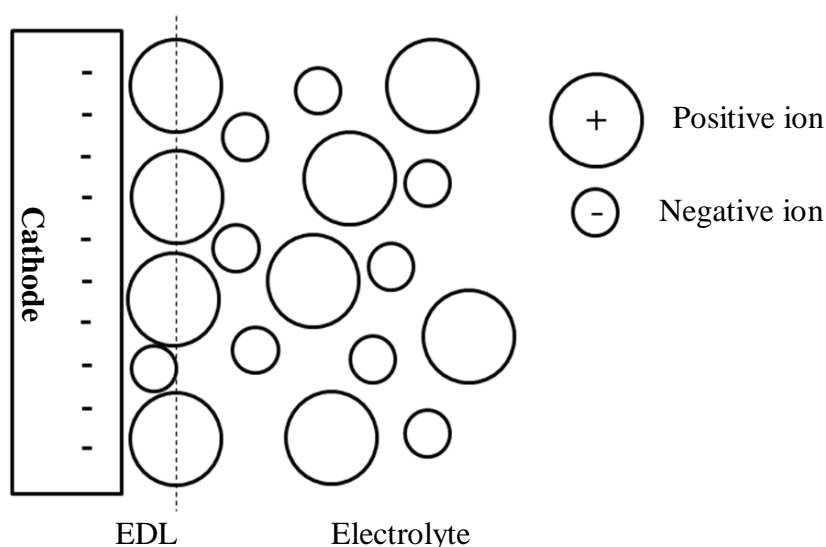


Figure 3.1 Depiction of the EDL at the surface of the cathode.

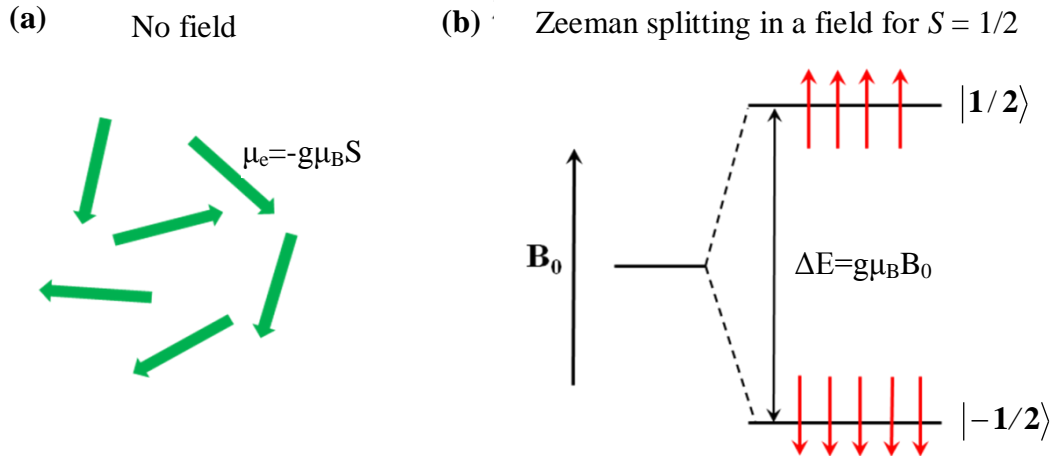


Figure 3.2 Paramagnet with magnetic moment μ_e , and electronic spin $S = 1/2$ (a) and the effect of a static magnetic field (b). (from Ref. 4)

CV measurements are usually performed to study EDLCs. An idealized EDLC with a good charge retention exhibits a rectangular shaped voltammogram, which indicates no redox reaction.^[7] The value of the capacitance can be estimated from CV curves using the following equation:

$$C = \frac{dQ/dE}{dE/dt} = \frac{I}{dE/dt} \quad (3.1)$$

where I is the current, dE/dt is the potential sweep rate used in the CV measurements.

To form an EDL in a Li^+ ion electrolyte, the physisorption of Li^+ ions onto electrode/electrolyte interfaces is required. This suggests that it is important to investigate the behavior of Li^+ ions in the battery system.^[8] ^7Li magic angle spinning (MAS) NMR spectroscopy has been widely used to study the environments and motions of the Li^+ ions in electrode materials. ^7Li nuclei has a high natural abundance (93%), and a large quadrupolar moment ($I=3/2$), so that NMR is sensitive to detect a small amount of Li^+ ions.^[9-11] Since cathode materials such as LiMn_2O_4 are paramagnetic, the lithium NMR spectra are affected by the interactions between lithium nuclear spins and unpaired electron spins in the cathode (Fig. 3.2). These interactions offer valuable information concerning the local environments around Li^+

ions.^[12, 13]

In this chapter, comprehensive discussion will be given on the unknown capacity of ca. 100 Ah/kg in 2.8 – 2.0 V in the Mn12 MCBs, based on solid-state ⁷Li MAS NMR on the *ex situ* cathode samples, and CV measurements. It is proposed that Li⁺ ions play an important role in the formation of EDL below 2.8 V in the discharging process.

3.2. CV measurements of Mn12 MCBs

3.2.1. Experimental

The coin cell batteries are fabricated for CV measurements (see the experimental section of Chapter 2). The cathodes are prepared by mixing Mn12Pe^f, carbon black and PTFE in the weight ratio of 10: 70: 20. The coin cells are assembled in an Argon glovebox with Li foil as an anode, polypropylene as a separator, and 1 M LiPF₆ EC/DEC solution as an electrolyte. The CV measurements of the Mn12 MCBs are carried out using a Biologic SP-150 potentiostat. The current density is calculated based on the weight of Mn12Pe^f in the cathode. Since it is well-known that carbon materials exhibit EDLCs, CV measurements are also performed on the coin cell using carbon black as a cathode, Li metal as an anode, 1 M LiPF₆ EC/DEC solution as an electrolyte to obtain an EDL capacitance of only carbon black.

3.2.2. Results and discussion

Figure 3.3 shows a CV curve for the Mn12 MCBs measured at a scan rate of 1.0 mV/s in a potential window of 1.8 – 4.0 V, which is nearly consistent with that of the charging/discharging test (see Chapter 2). The current obviously shows an increase in the voltage range of 3.0 – 4.0 V, indicating electrochemical reactions, which are ascribed to the redox of Mn ions, as described in Chapter 2. However, the current depends little on the voltage in the range of 1.8 – 3.0 V, indicating no oxidation and reduction. To investigate the electrochemical behavior below 3.0 V, CV curves of the Mn12 MCBs were measured between 1.8 and 3.0 V at scan rates of 0.5, 1.0, and 3.0 mV/s. As shown in Fig. 3.4, the curves at 0.5 and 1.0 mV/s exhibit nearly rectangular shapes, indicating a typical EDL behavior, as reported for carbon nanomaterial-based

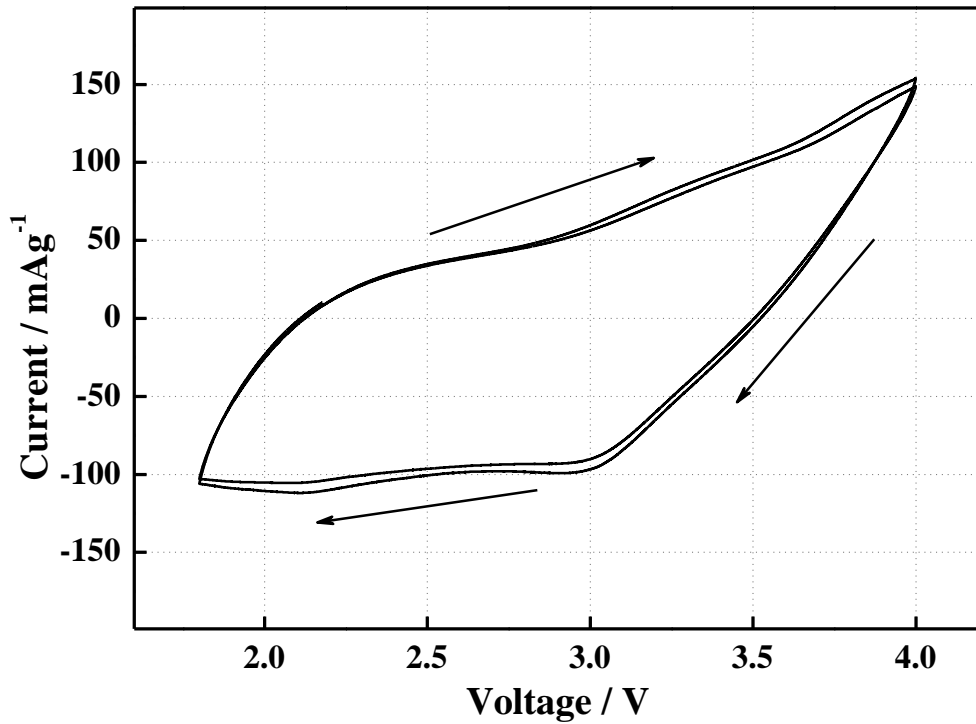


Figure 3.3 Cyclic voltammograms of Mn12 MCBs in the range of 1.8 – 4.0 V at scan rate of 1.0 mV/s.

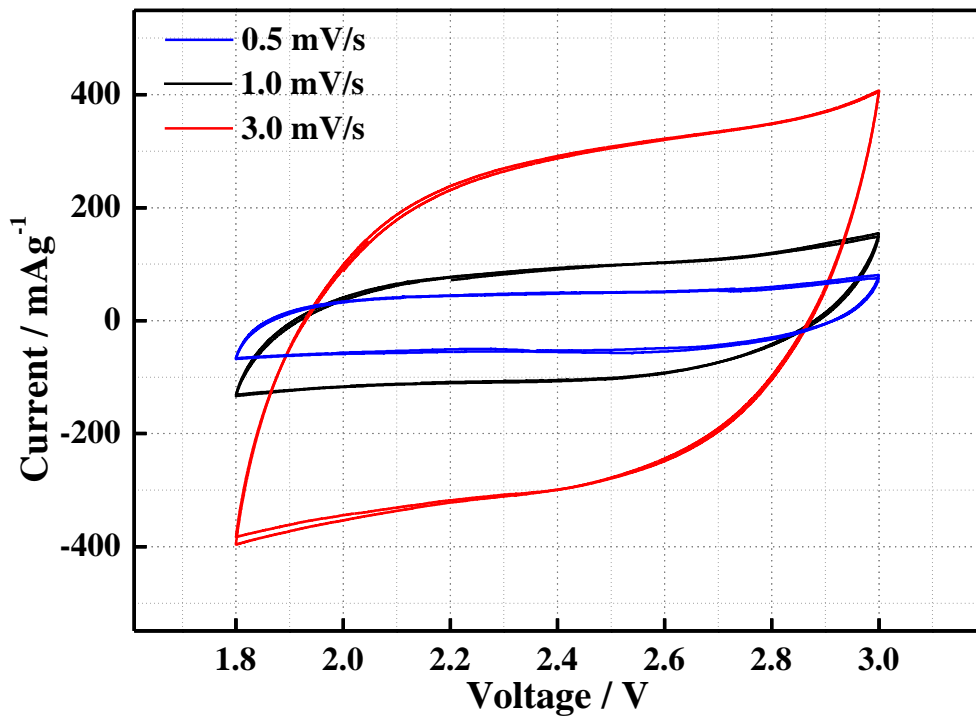


Figure 3.4 Cyclic voltammograms of Mn12 MCBs in the range of 1.8 – 3.0 V at scan rates of 0.5, 1.0, 3.0 mV/s.

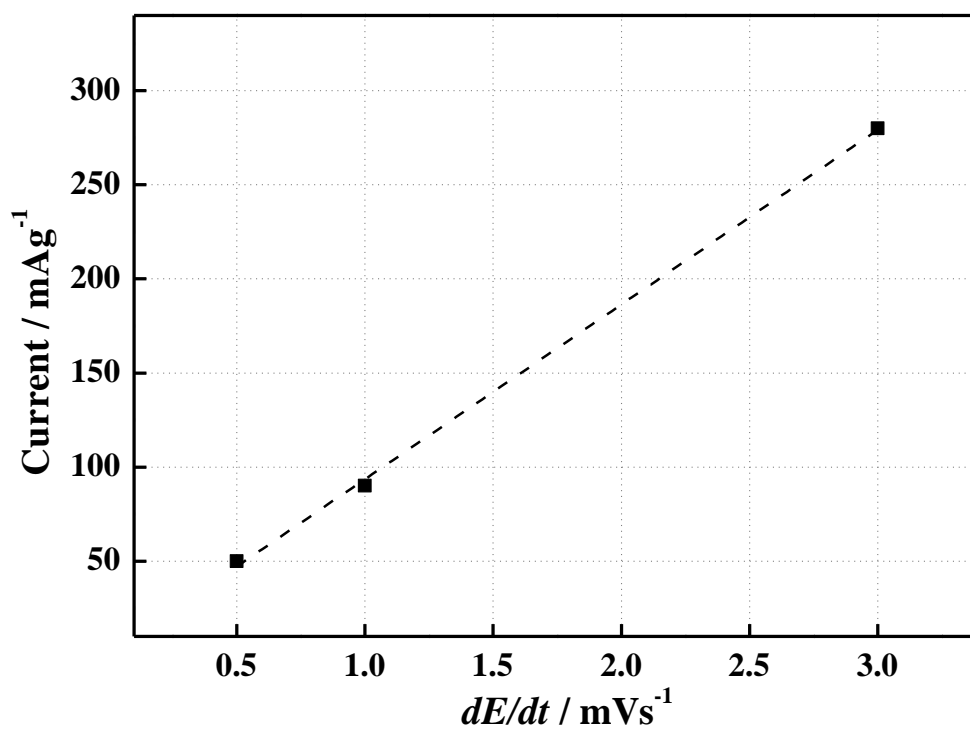


Figure 3.5 Plot of the current in the EDL as a function of scan rate of Mn12 MCBs.

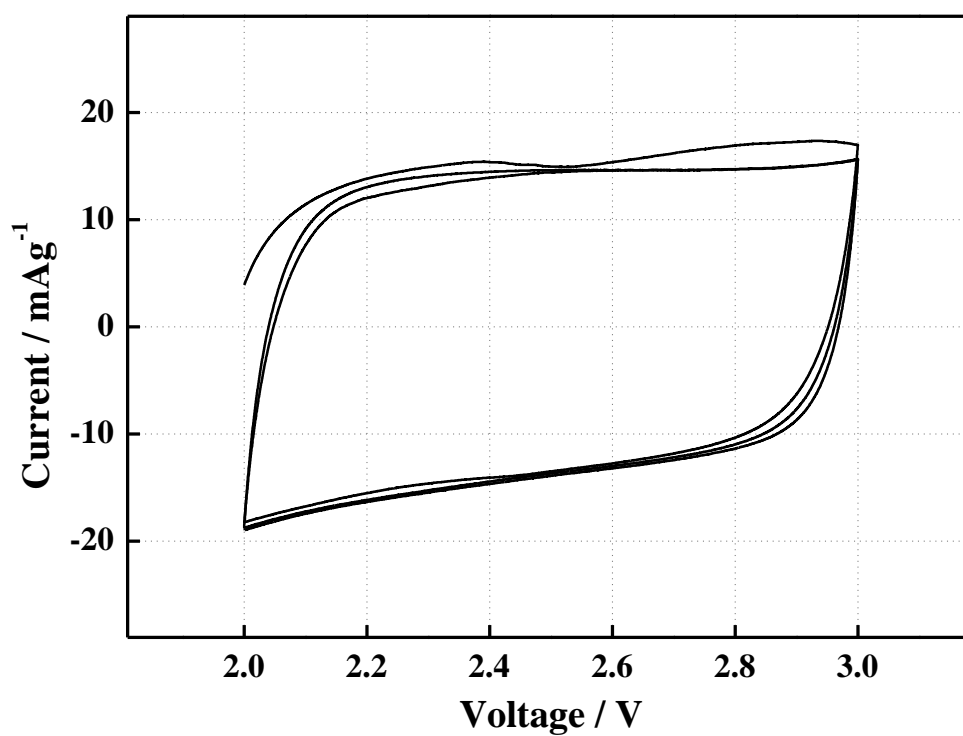


Figure 3.6 Cyclic voltammograms of carbon black in the range of 2.0 – 3.0 V at scan rate of 1.0 mV/s.

capacitors.^[14, 15] The absolute value of the current increases with increasing scan rate, suggesting that it is capacitive in nature. At the high scan rate of 3.0 mV/s, the curve deviates from a regular rectangular shape, suggesting imperfect reversibility perhaps at the separator-electrode interface, due to an ohmic drop, which is a usual characteristic of EDLC.^[16-19] In Fig. 3.5, the anodic currents at 2.4 V in the rectangular shaped CVs are plotted as a function of scan rate. The linear relation between them indicates that the EDL capacitance is stable and constant, being independent of the scan rate, since the capacitance is defined by Eq. 3.1. Using these results, the value of the EDL capacitance is estimated as ca. 100 F/g, which is comparable to those of high-performance carbon material-based capacitors. This value can be converted to a battery capacity, ca. 70 Ah/kg, by assuming that the working voltage V of the capacitance is 2.4 V. Note that the relationship between the units of F/g (capacitance) and Ah/kg (capacity) is as follows:

$$A \cdot h \cdot kg^{-1} = \frac{F \cdot g^{-1}}{3.6} \cdot V \quad (3.2)$$

Figure 3.6 shows a CV curve for carbon black measured at a scan rate of 1.0 mV/s between 2.0 and 3.0 V, where the current is about 15 mA/g, and then the EDLC capacity is calculated as ca. 10 Ah/kg. These results mean that the contribution from carbon black can be neglected. Although the value of the EDLC, ca. 70 Ah/kg, is smaller than the actual battery capacity, 100 Ah/kg, it is due to a fast scan rate in CV measurements.

The CV measurements of the Mn12 MCBs indicate that the capacity of 100 Ah/kg in 2.0 – 2.8 V can be explained by the EDL capacitance. Since the operating voltage of usual EDLCs using organic electrolyte does not exceed 3.0 V, this working voltage is quite reasonable.^[4] The value of the EDLC observed in the present battery is as high as those of high performance capacitors recently reported in carbon nanomaterials.^[5] Combination of the EDL capacitance and the redox behavior of the Mn ions brings about the high capacity of the Mn12 MCBs.

3.3. Solid-state ^7Li NMR measurements of Mn12 MCBs

3.3.1. Experimental

To prepare the *ex situ* NMR samples, the coin cell batteries were fabricated using a standard assembly procedure. The cathodes were prepared by mixing Mn12Pe^t, carbon black and PTFE in the weight ratio of 10: 70: 20. The coin cells were assembled in an Argon glovebox with Li foil as an anode, polypropylene as a separator, and 1 M LiPF₆ EC/DEC solution as an electrolyte. The cells were cycled galvanostatically at 0.1 mA in the voltage range of 2.0 – 4.0 V. The cathode samples for NMR studies were taken out from coin cells stopped at various voltages during charging/discharging. After drying, the cathodes (5 mg) were crushed, and then were inserted into zirconia rotors with a diameter of 4.0 mm for MAS NMR measurements. The samples were not washed in order to prevent the decomposition of solid electrolyte interface (SEI) and any loss of active materials.

The NMR spectra were acquired at 194.38 MHz using a Bruker-500 MHz spectrometer, with a 4.0 mm probe at a 10 kHz spinning speed. All the spectra were referenced to a ^7Li peak of 1 M LiCl aqueous solution. A rotor-synchronized spin echo sequence ($90^\circ - \tau - 180^\circ - \tau - \text{acq.}$) was used to collect a total of 256 scans for each spectrum. A recycle delay of 5 seconds was used to avoid a saturation of the ^7Li signal.

3.3.2. Results and discussion

Battery performance of Mn12 MCBs

Figure 3.7(a) shows the charging/discharging curves of the first two cycles for the Mn12 MCBs at a constant current of 0.1 mA in the voltage range of 2.0 – 4.0 V. A large capacity of ca. 210 Ah/kg is obtained in the first discharging, but the capacity slightly decreases in the second cycle. The behavior is similar to that of the *in situ* XAFS batteries (Fig. 2.7). The charging/discharging voltage vs. time plots are shown in Fig. 3.7(b). The voltages, at which the NMR spectra were measured (Fig. 3.8), are marked as black dots.

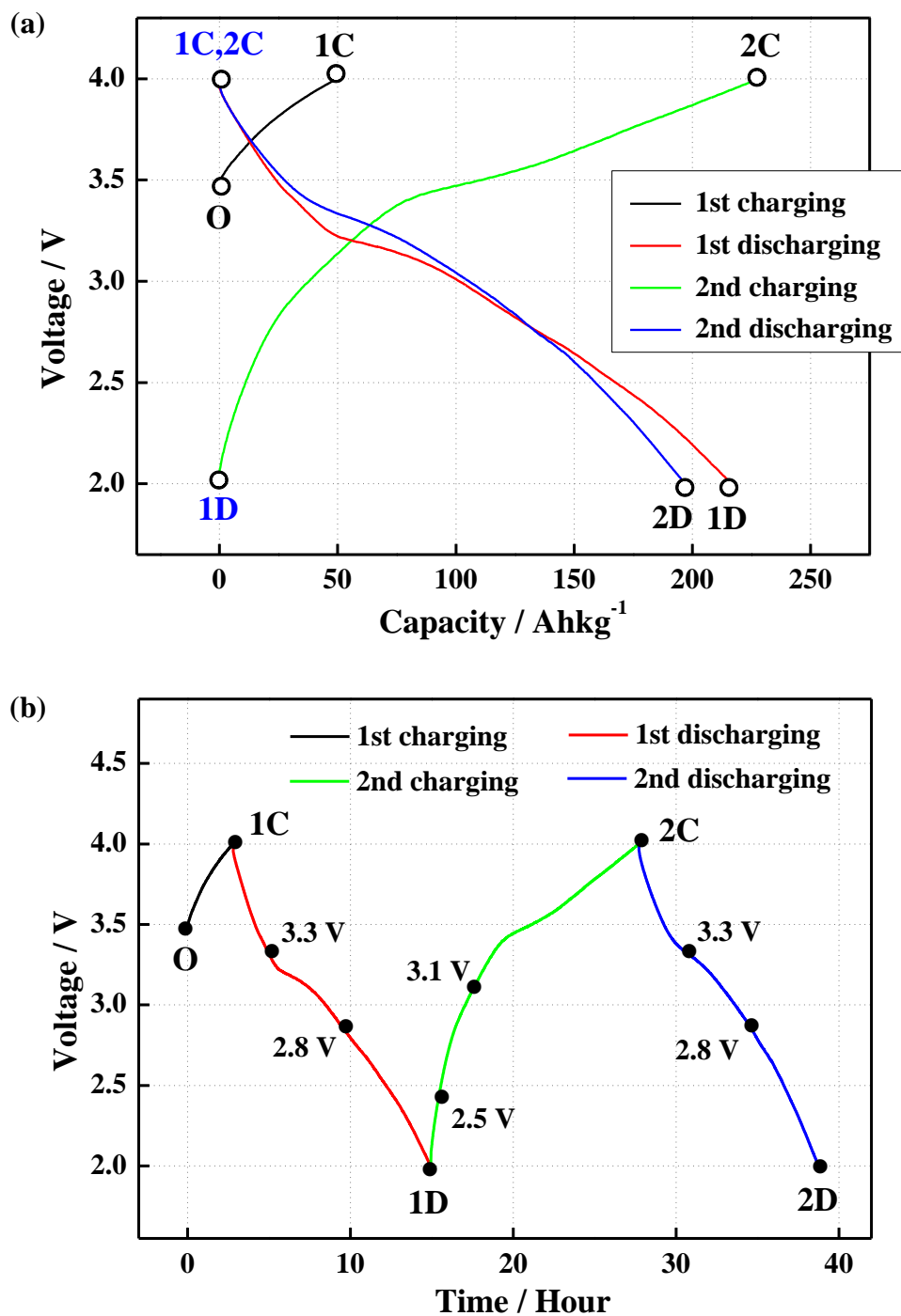


Figure 3.7 (a) Charging/discharging curves of a coin cell of Mn₁₂Pe' MCBs. The labels, O, 1C, 1D, 2C and 2D, indicate the characteristic samples in the first two cycles of the battery reaction. (b) Charging/discharging voltage vs. time curves for coin cell. Black dots show the different voltage states at which NMR spectra were collected.

⁷Li MAS NMR studies

Figure 3.8 shows the ⁷Li MAS NMR spectra of the cathodes obtained at various voltages during charging/discharging. A major resonance at 0 ppm in the NMR spectra was observed for every sample. In order to obtain the values of the line width and the chemical shift, we carried out a Lorentzian fitting of the NMR spectra using the software DMFIT 2008.^[20] Figure 3.9 shows the curve fittings for the spectra denoted by **O**, **1C**, **1D**, **2C**, and **2D**. The spectra can be divided into three components: a rather narrow peak at -0.5 ppm or -1 ppm (blue curve), a very broad central peak at about 0 ppm (gray curve), and a sharp and weak peak at -0.3 ppm (green curve). These green-curve resonances at -0.3 ppm can be ascribed to the Li⁺ ions in a diamagnetic environment in the solid-electrolyte interphase (SEI) or in the residual electrolyte, while the gray-curve peaks are due to the contribution of the Li⁺ ions randomly dispersed in carbon.^[21-23] Then, the blue-curve peaks are assignable to the mobile Li⁺ ions in the batteries, which are affected by the surrounding environment of the Li⁺ ions in the cathode.^[24] We analyzed the blue curves in detail, to reveal the dependence on the charging/discharging.

Figure 3.10 shows the evolution of the line width of the blue curves as a function of the voltage. After the first charging, the line width shows only a slight decrease. The first discharging increases the line width from 200 Hz to 1350 Hz after a plateau in the range of 4.0 – 3.3 V. The line width becomes constant in the range of 2.0 – 3.1 V during the second charging, then the value quickly decreases, and reaches 400 Hz at $V = 4.0$ V. The second discharging exhibits similar behavior to that of the first discharging. It is well known that the broad and narrow line widths indicate low and high mobilities of Li⁺ ions, respectively.^[24] The line width becomes broader during the discharging process, which means that the mobility of the Li⁺ ions decreases, while it becomes narrower during charging, which suggests a mobility increase. It is thought that the Li⁺ ions would come closer to the active material, Mn12, resulting in a strong electrostatic interaction between reduced Mn12 molecules and Li⁺ ions, and a low mobility of Li⁺ ions in the discharging process, while they leave from the Mn12

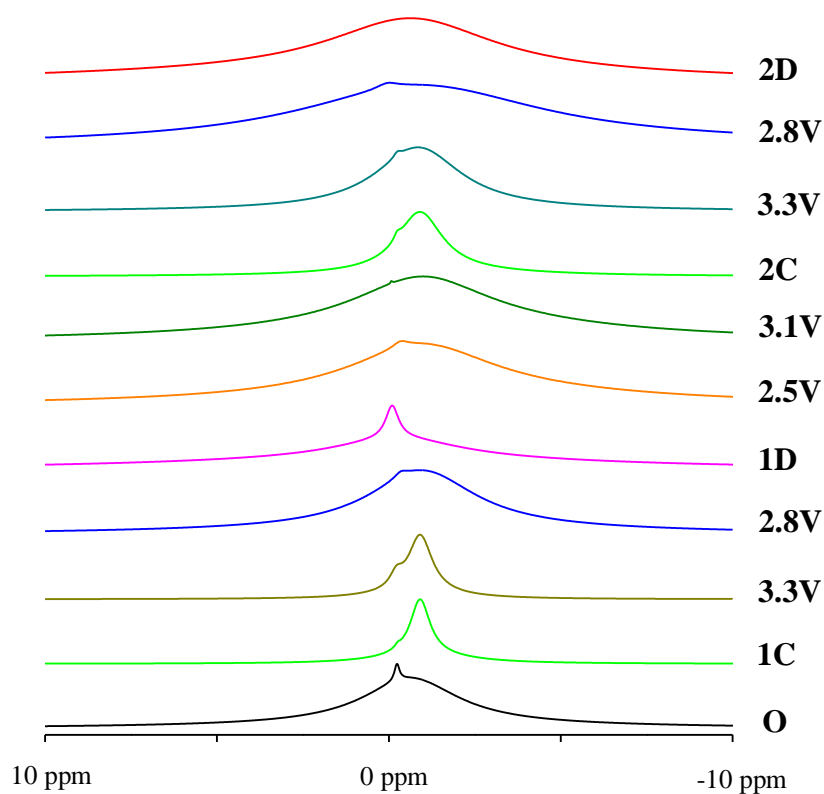


Figure 3.8 ^7Li MAS NMR spectra of $\text{Mn}_{12}\text{Pe}^t$ cathodes at various charging/discharging voltages during the first two cycles.

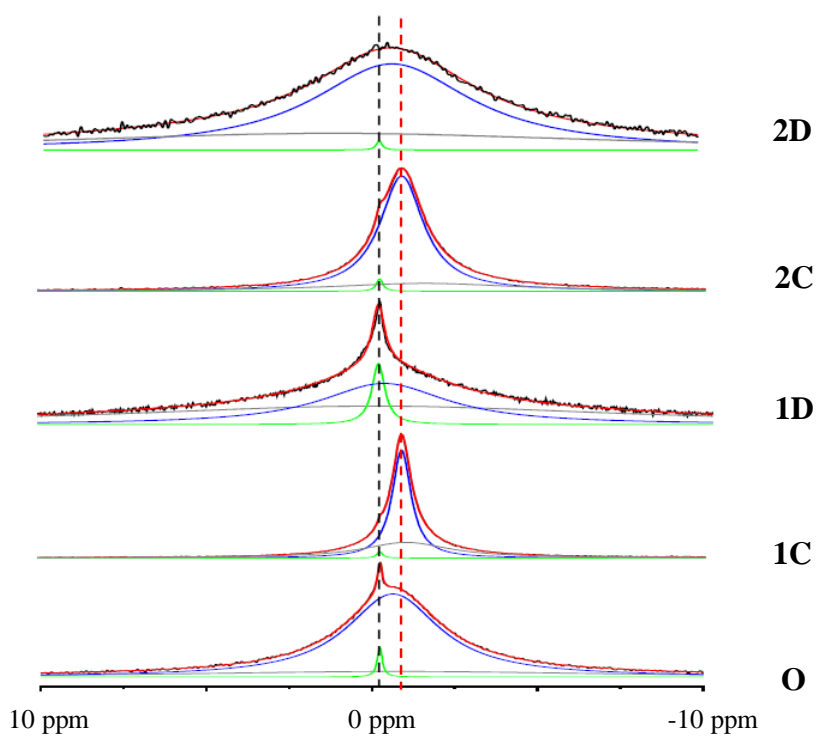


Figure 3.9 Curve fitting results of ^7Li NMR spectra for **O**, **1C**, **1D**, **2C** and **2D**. (Black line is experimental curve; red line is simulated curve; the assignments of blue, green and gray components are described in the text.)

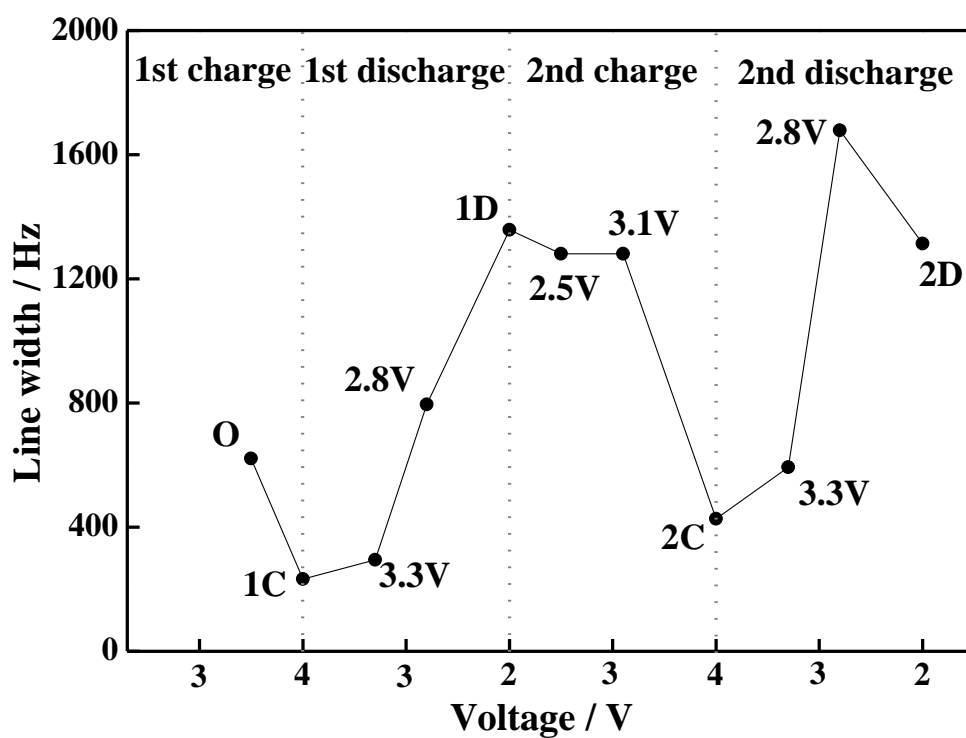


Figure 3.10 ^7Li MAS NMR line width evolution as a function of cell voltage.

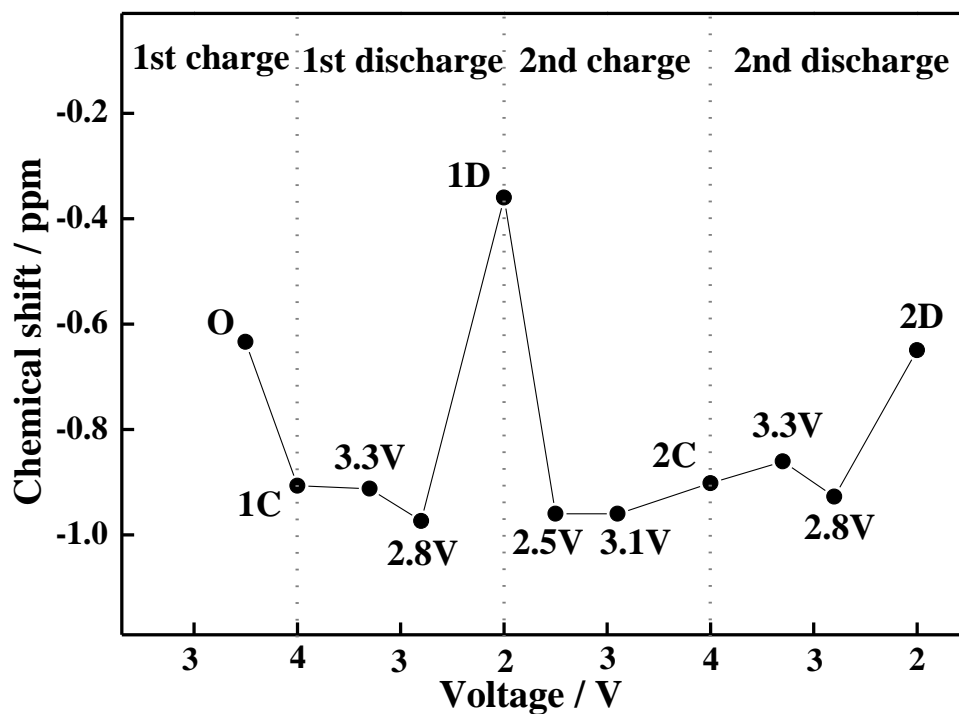


Figure 3.11 ^7Li MAS NMR chemical shift as a function of cell voltage.

molecules and become free during charging.

Figure 3.11 shows the chemical shift change during charging/discharging processes. During the first discharging, the chemical shift exhibits a quick increase to higher fields after passing through a plateau in the range of 4.0 – 2.8 V. In the second charging, the chemical shift shows a quick decrease in the range of 2.0 – 2.5 V, and then becomes constant at 2.5 – 4.0 V. The second discharging exhibits a similar dependence of the chemical shift as that in the first discharging.

It is well known that the chemical shifts of NMR spectra are governed by the secondary magnetic field, due to the electronic current induced by the applied field. For the small nucleus with only 1s electron such as H and Li^+ , the chemical shifts result from the neighbor anisotropy effect.^[25, 26] Namely, negative shifts indicate the decrease of local paramagnetic moments on the neighboring atoms, while positive shifts mean the increase. The negative/positive change of the chemical shifts observed in the charging/discharging would correspond to the decrease/increase of the paramagnetic moments of Mn12 clusters. The *in situ* XAFS study (Chapter 2) revealed that the oxidation/reduction reaction is caused by the redox change between Mn^{3+} ($S = 2$) and Mn^{2+} ($S = 5/2$) ions during the charging/discharging processes. These results suggest that the paramagnetic moment of the Mn12 cluster decreases/increases during charging/discharging, which is consistent with those from the solid-state ^7Li NMR studies.

^7Li NMR spectra for layered materials (e.g. LiCoO_2) usually exhibit a large positive change in the chemical shift, due to a close contact between Li^+ and Co ions when Li^+ ions are inserted into the interlayer.^[27] However, only a small positive shift was observed in ^7Li NMR spectra of Mn12 cathode. This means that Li^+ ions have a weak interaction with the core Mn ions of the Mn12 molecule, since the carboxylate ligand moiety of Mn12 prevent a contact of Li^+ ions with Mn ions, even after discharging.

Ex situ solid-state ^7Li MAS NMR revealed the evolution of the mobility and the local environment of Li^+ ions in the battery reaction of the Mn12 MCBs. It is concluded that the Li^+ ions leave from the Mn12 molecule during charging, while they

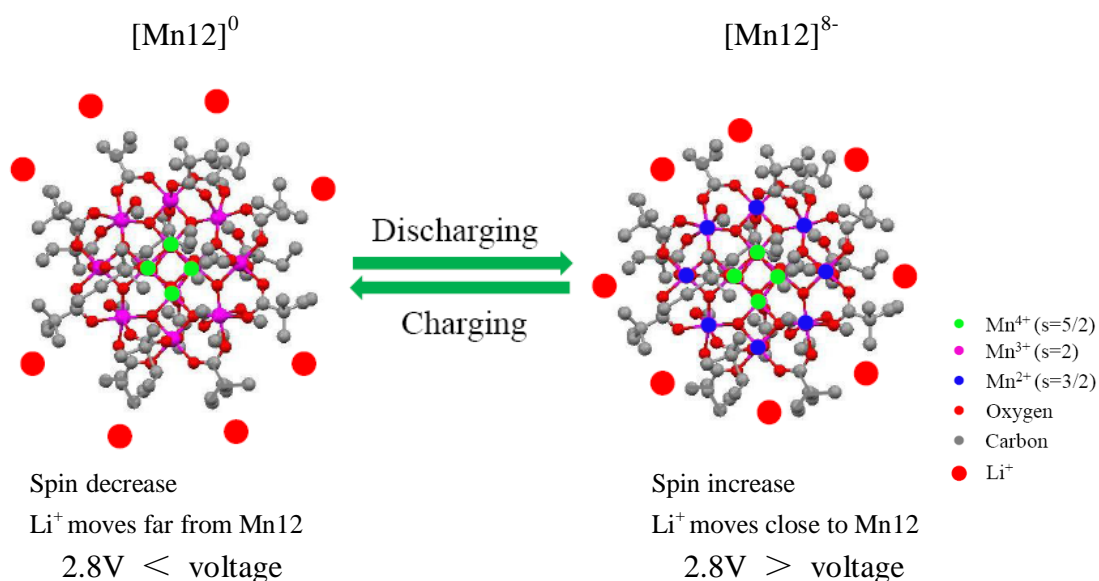


Figure 3.12 Evolution of Li^+ ions position during charging/discharging.

come closer to the Mn12 molecules during discharging (Fig. 3.12).

3.4. Discussions on the EDL formation in Mn12 MCBs

Based on the CV and NMR results, the formation of an EDL in the discharging process of the Mn12 MCBs is schematically shown in Fig. 3.13. In the first step of discharging, the $[\text{Mn12}]^0$ clusters are reduced to $[\text{Mn12}]^{8-}$ in the voltage range of 4.0 to 2.8 V (Fig. 3.13(a)). Then, the Li^+ ions move to the Mn12 clusters, and are trapped on the surfaces of the Mn12 clusters. In the range of 2.8 – 2.0 V, the surface of the carbon black electrodes is charged negatively (Fig. 3.13(b), (c)), and an EDL is formed at the interface of the carbon black electrode and the active material. This process is reversible in the charging process. The value of ca. 100 Ah/kg in 2.8 – 2.0 V can be explained by this EDL capacitance (supercapacitance) effect. So the Mn12 MCBs exhibit a higher capacity than the theoretical one estimated from only the redox of the Mn ions in Mn12. This is an advantage of the Mn12 MCBs, although a combination of the redox reactions and the EDL capacitance is not usual.

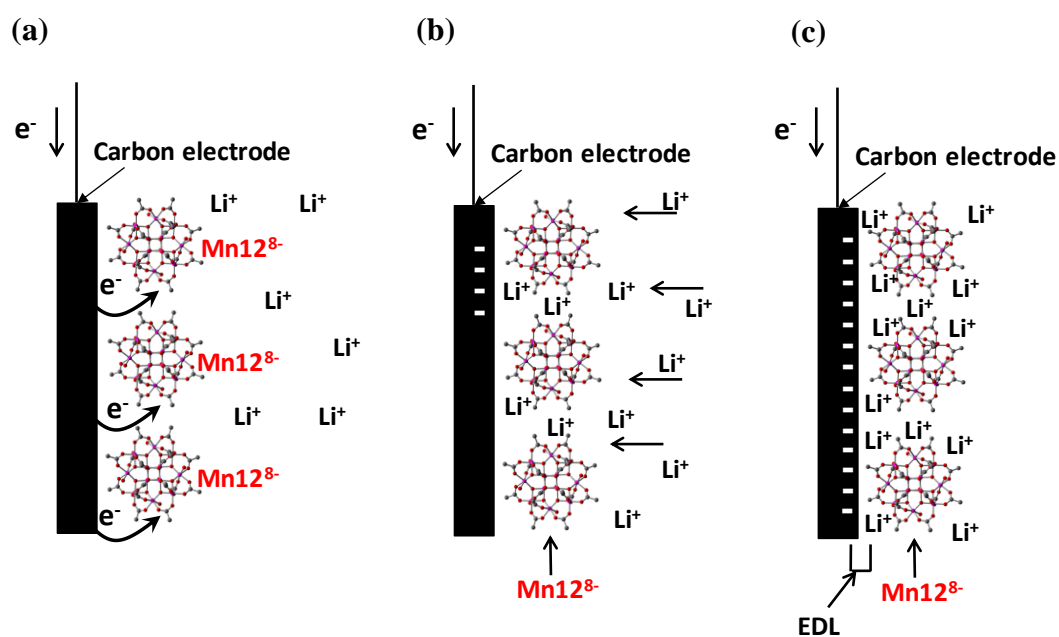


Figure 3.13 Procedure of EDL formation (a) Mn12 clusters are reduced to $[Mn12]^{8-}$ (b) Li ions accumulate on the surface of Mn12 clusters (c) EDL forms at the interface between carbon and Mn12 clusters.

References

- [1] H. Itoi, H. Nishihara, T. Kogure, T. Kyotani, *J. Am. Chem. Soc.* **2011**, *133*, 1165-1167.
- [2] Y. W. Zhu, S. Murali, M. D. Stoller, K. J. Ganesh, W. W. Cai, P. J. Ferreira, A. Pirkle, R. M. Wallace, K. A. Cychosz, M. Thommes, D. Su, E. A. Stach, R. S. Ruoff, *Science* **2011**, *332*, 1537-1541.
- [3] M. D. Stoller, S. Park, Y. W. Zhu, J. H. An, R. S. Ruoff, *Nano Lett.* **2008**, *8*, 3498-3502.
- [4] E. Frackowiak, *Phys. Chem. Chem. Phys.* **2007**, *9*, 1774-1785.
- [5] P. Simon, Y. Gogotsi, *Nat. Mater.* **2008**, *7*, 845-854.
- [6] M. Winter, R. J. Brodd, *Chem. Rev.* **2004**, *104*, 4245-4269.
- [7] C. H. Hamann, A. Hamnett, W. Vielstich, *Electrochemistry* (2nd Edition), Wiley-VCH, **2007**, 121.
- [8] G. Salitra, A. Soffer, L. Eliad, Y. Cohen, D. Aurbach, *J. Electrochem. Soc.* **2000**,

- 147, 2486-2493.
- [9] C. P. Grey, N. Dupre, *Chem. Rev.* **2004**, *104*, 4493-4512.
- [10] P. kempgens, R. K. Harris, D. P. Thompson, *Solid State Nucl Mag* **1999**, *15*, 109-118.
- [11] C. P. Grey, Y. J. Lee, *Solid state Science* **2003**, *5*, 883-894.
- [12] W. S. Yoon, N. Kim, X. Q. Yang, J. M. Breen, C. P. Grey, *J. Power. Sources.* **2003**, *5*, 649-653.
- [13] D. L. Zeng, J. Cabana, J. Breger, W. S. Yoon, C. P. Gray, *Chem. Mater.* **2007**, *19*, 6277-6289.
- [14] E. Frackowiak, F. Beguin, *Carbon* **2011**, *39*, 937-950.
- [15] J.H. Chen, W.Z. Li, D. Z. Wang, S. X. Yang, J. G. Wen, Z. F. Ren, *Carbon* **2002**, *40*, 1193-1197.
- [16] M. D. Ingram, A. J. Pappin, F. Delalande, D. Poupard, G. Terzulli, *Electrochem. Acta.* **1998**, *43*, 1601-1605.
- [17] R. Chandrasekaran, Y. Soneda, J. Yamashita, M. Kodama, H. Hatori, *J. Solid.State. Electrochem.* **2008**, *12*, 1349-1355.
- [18] A. K. Arof, N. E. A. Shuhaini, N. A. Alias, M. Z. Kufian, S. R. Majid, *J. Solid. State. Electrochem.* **2010**, *14*, 2145-2152
- [19] S. -B. Ma, K. W. Nam, W. S. Yoon, X. Q. Yang, K. Y. Ahn, K. H. Oh, K. -B. Kim, *J. Power. Sources.* **2008**, *178*, 483-489.
- [20] D. Massiot, F. Fayon, M. Capron, I. King, S. Le Calvé B. Alonso, J. -O. Durand, B. Bujoli, Z. Gan, G. Hoatson, *Magn. Reson. Chem.* **2002**, *40*, 70-76.
- [21] B. Key, R. Bhattacharyya, M. Morcrette, V. sezner, J. -M. Tarascon, C. P. Grey, *J. Am. Chem. Soc.* **2009**, *131*, 9239-9249.
- [22] R. E. Gerald, J. Sanchez, C. S. Johnson, R. J. Klingler, J. W. Rathke, *J. Phys.: Condens. Mater.* **2001**, *13*, 8269-8285
- [23] N. Yamakawa, M. Jiang, B. Key, C. P. Grey, *J. Am. Chem. Soc.* **2009**, *131*, 10525-10536.
- [24] J. D. Jeon, S. Y. Kwak, *Macromolecules* **2008**, *39*, 8027-8034.
- [25] Y. Zou, N. Inoue, *Ionics* **2005**, *11*, 333-342.

- [26] M. Menetrier, I. Saadoune, S. Levasseur, C. Delmas, *J. Mater. Chem.* **1999**, *9*, 1135-1140.
- [27] M. Kerlau, J. A. Reimer, E. J. Cairns, *Electrochem. Comm.* **2005**, *7*, 1249-1251.

Chapter 4

In situ magnetic studies of Mn12 MCBs

4.1. Introduction

A family of Mn12 cluster exhibits exotic magnetic properties, such as a single-molecule magnet (SMM) behavior, due to a strong magnetic anisotropy, and a large ground-state spin ($S = 10$).^[1-5] As well as neutral Mn12 clusters, one- or two-electron reduced Mn12 clusters, which can be prepared by chemical reduction methods, are isolated, and their magnetic properties have been investigated.^[6-11]

Magnetic studies of these anions suggest that their ground spin states change due to the variation of Mn-Mn spin exchange interactions in the Mn12 core structure resulting from the valence change of the Mn^{3+} to Mn^{2+} .^[7, 12] $[\text{Mn12}]^-$ salts have an $S = 19/2$ ground state, while two electron reduced $[\text{Mn12}]^{2-}$ anions exhibit a ground state spin of 10, the same as that of the neutral Mn12. More recently, Christou's group has reported $[\text{Mn12}]^{3-}$ possessing a half integer $S = 17/2$ ground state.^[13] These reduced Mn12 derivatives maintain a SMM behavior, although the blocking temperature, and total spin moment are tuned.

As described in Chapter 2, XAFS studies indicate that $[\text{Mn12}]^{8-}$ is formed in the discharging process of the Mn12 MCBs. Since this kind of super-reduced Mn12 clusters could not be obtained by usual chemical and solution electrochemical methods, it is expected that they exhibit novel and exotic magnetic properties.

In the present study, *in situ* magnetic analysis of the Mn12 MCBs are carried out to investigate the magnetic properties of $[\text{Mn12}]^{8-}$. Such *in situ* measurements are useful, because $[\text{Mn12}]^{8-}$ is probably unstable, and its magnetic properties couldn't be evaluated exactly by *ex situ* methods. In addition, this method is also useful to understand the intermediate reduced states between $[\text{Mn12}]^0$ and $[\text{Mn12}]^{8-}$.

4.2. Experimental

4.2.1. Battery cells for *in situ* magnetic measurements.

A reusable battery cell is developed for *in situ* magnetic studies. A sketch of the *in situ* cell is illustrated in Fig. 4.1. In order to investigate magnetic properties using a SQUID device with a 9mm diameter sample chamber, a small diamagnetic battery is made from two quartz glass cells. Both quartz glass parts are held together to form a battery space. The cathode is prepared by the same procedure for the coin cell battery described in Chapter 3, and it contains ca. 2 mg of Mn12Pe^t. The anode material is a lithium metal foil (0.1 mm thickness). The electrolyte used in this study is a EC/DEC (7:3) solution of 1 M LiPF₆. A porous glass fiber (Whatman) is used as a separator. The final dimensions of the *in situ* cell are 5 mm (width) × 5 mm (height) × 15 mm (length). This *in situ* electrochemical cell allows us to investigate the magnetic properties of Mn12 MCBs without disassembling the battery.

4.2.2. *In situ* magnetic measurements

In situ magnetic measurements of Mn12 MCBs were carried out with a Quantum Design SQUID magnetometer (MPMS XL-5). The *in situ* cell was fixed onto the probe rod and inserted into the sample chamber (Fig. 4.2). The *in situ* cell was cycled galvanostatically at room temperature (300 K) until the second charging. The charging/discharging cycles were stopped at various voltages, and then the temperature was decreased to 1.8 K. Then, the field dependence of the magnetization

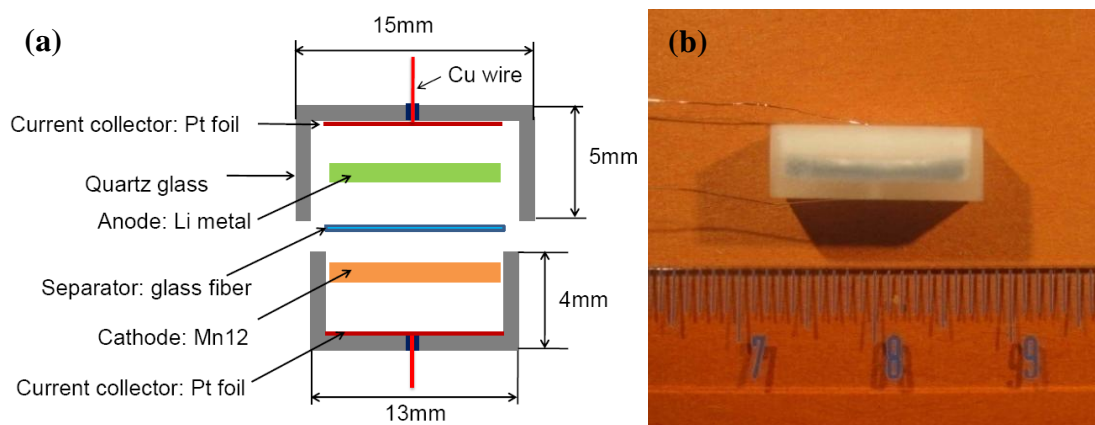


Figure 4.1 (a) Schematic sketch of the *in situ* cell, (b) Photograph of the *in situ* cell.

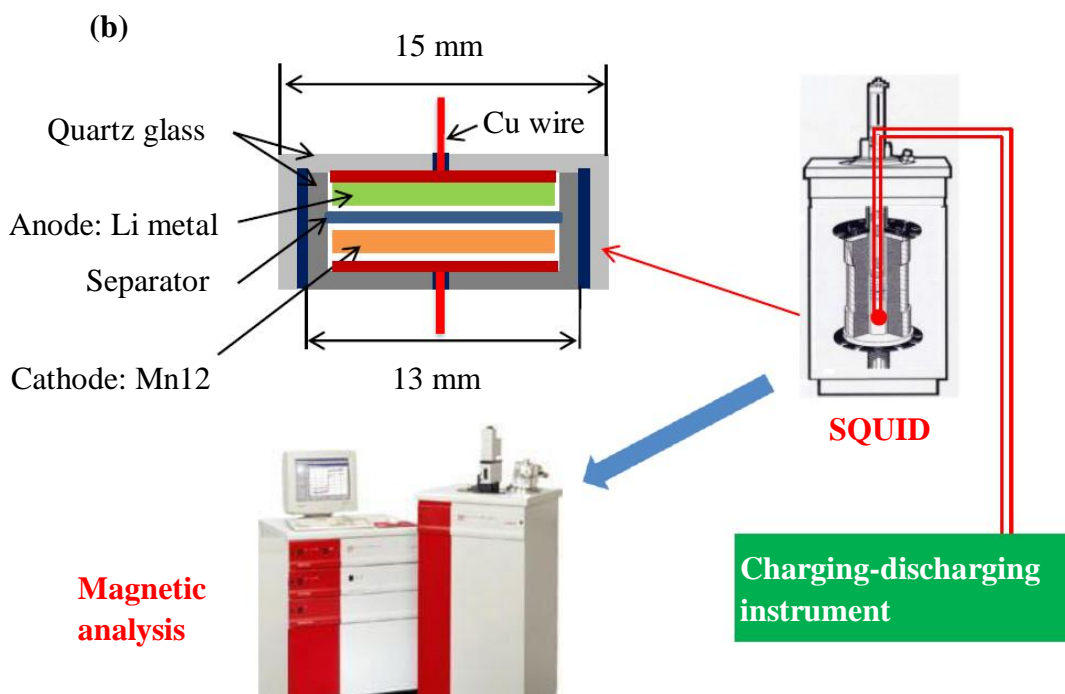
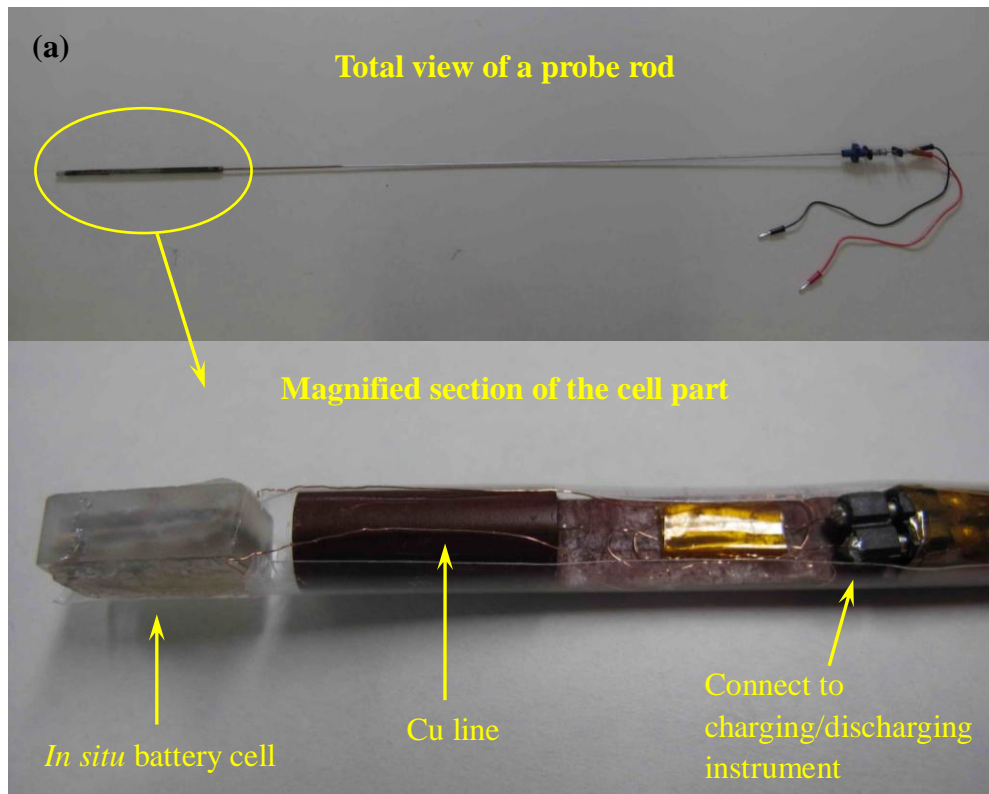


Figure 4.2 (a) Photograph of the *in situ* cell fixed on the probe rod, (b) Schematic sketch of the *in situ* magnetic measurement setup.

measurements were carried out, applying the field up to 5 T. The battery cells include carbon materials, PTFE binder, Li metal, platinum current collectors, and quartz glass boxes. Magnetic compensation for these materials was done by measuring the magnetization of the cell including other components except Mn12.

4.3. Results and discussion

Figure 4.3(a) shows the charging/discharging curves of the first cycle for an *in situ* magnetic battery cell at a constant current of 0.1 mA/cm² in the voltage range of 2.0 – 4.0 V. A capacity of ca.165 Ah/kg is obtained in the first discharging. Although this value is smaller than that of the coin cell battery (210 Ah/kg), it is probably caused by a loose contact between the cathode and the anode. The evolution of voltage as a function of time is shown in Fig. 4.3(b). The voltage of the samples, at which the magnetic measurements were performed, are marked with black dots.

The field dependence of the magnetization was examined at 1.8 K, increasing the magnetic field up to 5 T. Figure 4.4 shows the magnetization curves for the samples marked by black dots in Fig. 4.3(b). Since Mn12 in the cathode is a powder sample, the coercive field H_c for the present samples is smaller than that of a single crystalline sample of Mn12 reported in the literature.^[3] After the first charging, the magnetization curve of **1C** shows a saturation magnetization, similar to that of **O**. During the first discharging process, the value of the saturated magnetization gradually increases, as seen in the samples at 3.2 and 3.0 V. Then, the value becomes almost constant. The magnetizations are not saturated, even at 5 T, for the samples **O**, **2.8V**, **2.3V** and **1D**, indicating that the field is not enough to turn the magnetic domains completely along the field direction.

Mn12 molecule possesses a large ground state spin of $S = 10$, which can be rationalized on the basis of the sign and relative magnitude of the exchange interactions within the Mn12 core structure: the four central Mn⁴⁺ ions are weakly ferromagnetically coupled, and the remaining Mn³⁺-Mn⁴⁺ and Mn³⁺-Mn³⁺ interaction are all antiferromagnetic, with the former much stronger than the latter. As a result, the stronger Mn³⁺-Mn⁴⁺ interactions over the weaker Mn³⁺-Mn³⁺ ones, aligning the

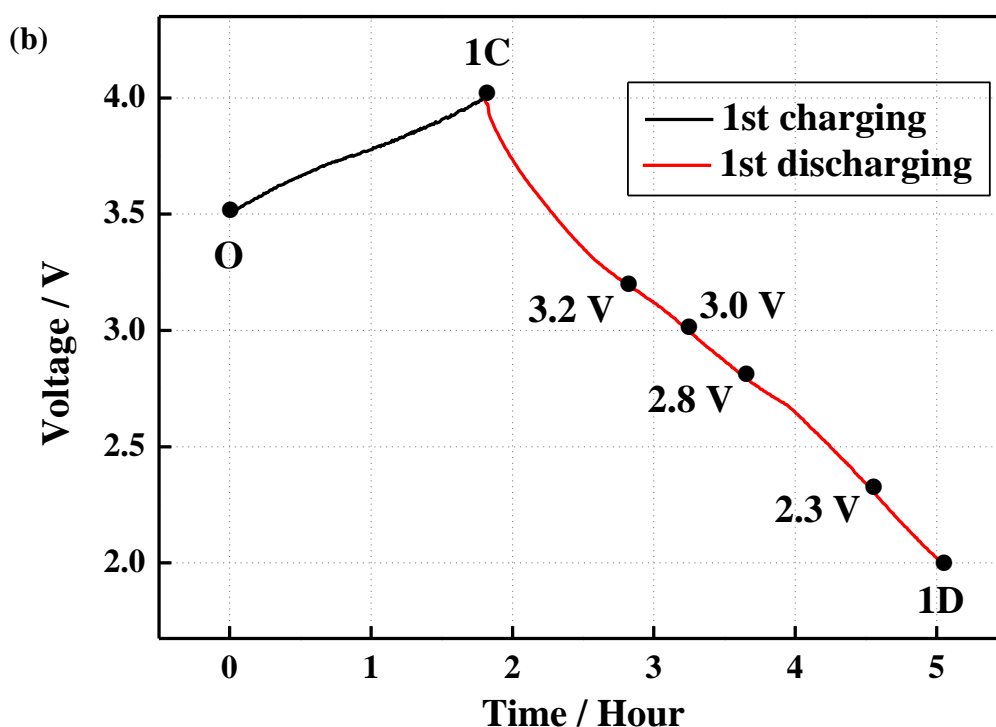
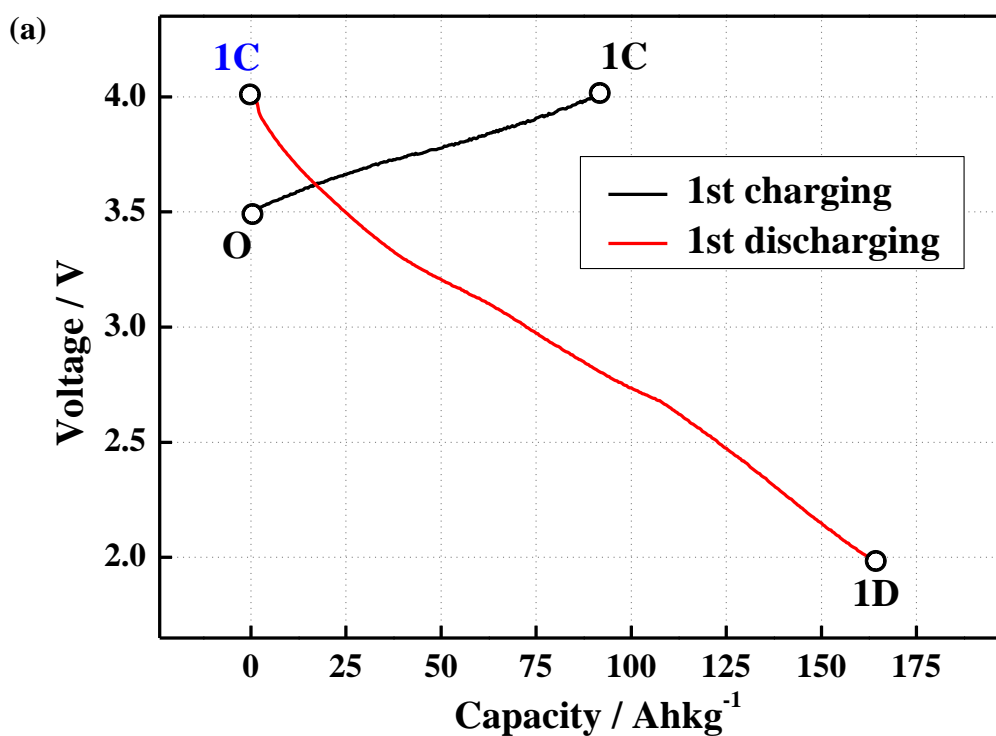


Figure 4.3 (a) Charging/discharging curves of *in situ* magnetic Mn12 MCBs. The labels, **O**, **1C**, **1D**, **2C** and **2D**, indicate the characteristic samples in the first two cycles of the battery reaction. (b) Charging/discharging voltage vs. time curves for *in situ* magnetic battery cell. Black dots show the different voltage states at which magnetic experiments were performed.

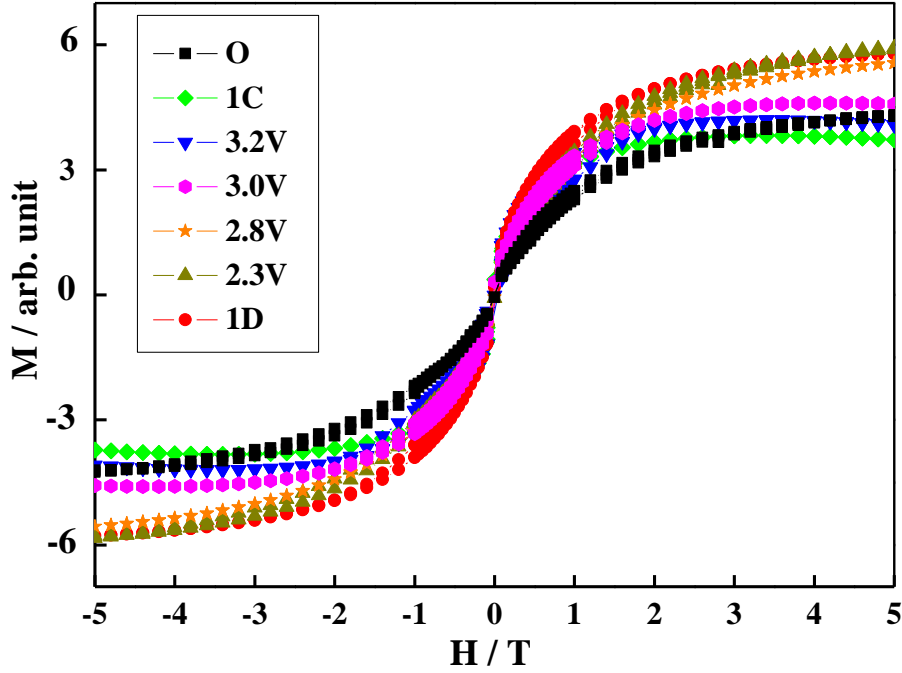


Figure 4.4 Magnetization curves for the *in situ* Mn12 MCBs at various voltage states.

spins of the outer Mn^{3+} ions all parallel and thus antiparallel to the central Mn^{4+} ions. This suggests that $[\text{Mn12}]^0$ has an $S = 16 - 6 = 10$ ground state,^[14-16] as described in details later. It is well known that magnetization for a powder sample tends to approach the saturation value M_{sat} at a low temperature and a high enough field, as in the following equation:^[1]

$$M_{sat} = Ng\mu_B S \quad (4.1)$$

where N is Avogadro's constant, g is Lande's factor, μ_B is the Bohr magneton, S is the spin number. The spin numbers of the Mn12 molecule during charging/discharging are estimated by inputting the magnetic moment at 5T into this equation. The results are summarized in Table 4.1.

The ground spin states of reduced Mn12 molecules could not be estimated exactly due to a change in the competing exchange interactions when the oxidation state of Mn ions is modified. In $[\text{Mn12}]^{8-}$ salts, the interactions between Mn^{2+} and Mn^{4+} ions overcome those between Mn^{2+} and Mn^{2+} ions. So all spins of the outer Mn^{2+} ions are aligned parallel, while they are antiparallel to those of the central Mn^{4+} ions. This means that the theoretical magnetizations of reduced Mn12 molecules can be simply calculated by assuming the antiferromagnetic interactions between Mn^{2+} ($S =$

Table 4.1 Magnetic parameters for each charging/discharging state.

Sample name	O	1C	3.2V	3.0V	2.8V	2.3V	1D
Experimental spin	10	8.7	9.5	10.7	13	13.8	13.5
Theoretical spin	10	10	10	12	14	14	14
Mn12 reduced state	[Mn12] ⁰	[Mn12] ⁰	[Mn12] ⁰	[Mn12] ⁴⁺	[Mn12] ⁸⁻	[Mn12] ⁸⁻	[Mn12] ⁸⁻

Theoretical spin numbers are calculated by assuming Mn²⁺ ($S = 5/2$), Mn³⁺ ($S = 2$), and Mn⁴⁺ ($S = 3/2$).

$5/2$ (HS), $g = 2$) (or Mn³⁺ ($S = 2$ (HS), $g = 2$)) and Mn⁴⁺ ($S = 3/2$ (HS), $g = 2$), and by ignoring the Jahn-teller effect of Mn³⁺. As described in Chapter 2, the reduction of Mn³⁺ to Mn²⁺ takes place at the eight Mn³⁺ sites in the narrow voltage range of 3.3 – 2.8 V of the discharging process. In this range, the Mn12 core is regarded as a formula of Mn⁴⁺₄Mn³⁺_{8-x}Mn²⁺_x ($x = 0 \sim 8$). The S values for [Mn12]^{x-} were calculated as follows:

$$S = [(8-x) \times 2 + x \cdot (\frac{5}{2}) - 4 \times (\frac{3}{2})] = 10 + \frac{x}{2} \quad (4.2)$$

$$\text{For example: } [\text{Mn}^{4+}_4\text{Mn}^{3+}_8]^0 : S = 2 \times 8 - \frac{3}{2} \times 4 = 10$$

$$[\text{Mn}^{4+}_5\text{Mn}^{3+}_7]^+ : S = 2 \times 7 - \frac{3}{2} \times 5 = 6.5$$

$$[\text{Mn}^{4+}_4\text{Mn}^{3+}_4\text{Mn}^{2+}_4]^{4-} : S = 2 \times 4 + \frac{5}{2} \times 4 - \frac{3}{2} \times 4 = 12$$

$$[\text{Mn}^{4+}_4\text{Mn}^{2+}_8]^{8-} : S = \frac{5}{2} \times 8 - \frac{3}{2} \times 4 = 14$$

The experimental and theoretical spin numbers for each discharging state are summarized in Table 4.1. Figure 4.5 shows the evolution of the spin number in the Mn12 cluster as a function of the battery voltage during the first discharging. The red curve exhibits the theoretical spin number, while the black curve indicates the experimental results. Experimental and theoretical analyses agree fairly well with each other. This confirms that [Mn12]⁸⁻ has a larger ground state spin number ($S = 14$) than that of [Mn12]⁰ ($S = 10$). Although a significant spin change was observed above 2.8 V, it is consistent with the voltage range in which eight electron reductions occur, as indicated by *in situ* XAFS analysis.

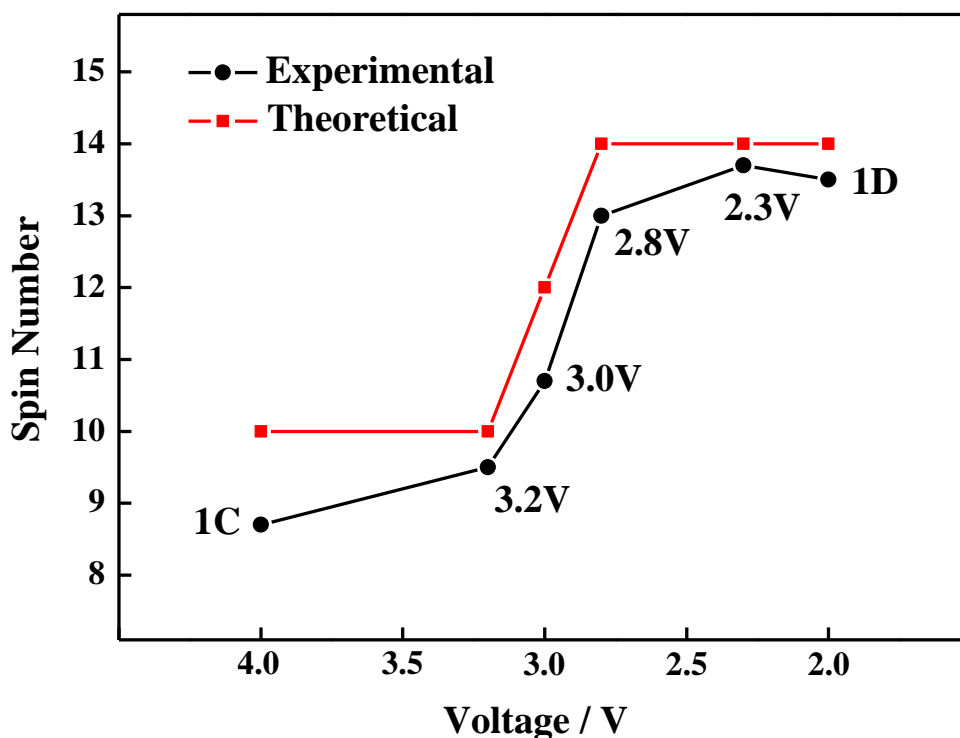


Figure 4.5 Voltage evolution of spin number in Mn12 MCBs during the first discharge.

4.4. Conclusions

In situ magnetic analysis on Mn12 MCBs was carried out to investigate the magnetic properties of super reduced Mn12. It is suggested that $[\text{Mn12}]^{8-}$ possesses a high-spin state of $S = 14$, which is higher than that of $[\text{Mn12}]^0$ ($S = 10$). This means that super reduced Mn12 species, with higher ground spin states were prepared by solid-state electrochemistry. These results also confirm that the valence of Mn ions change by above 2.8V, which agrees with those of the *in situ* XAFS analysis. This *in situ* magnetic measurement method is useful to elucidate novel magnetic properties of metal complexes with unusual oxidation states, obtained by a solid-state electrochemistry.

References

- [1] R. Bagai, G. Christou, *Chem. Soc. Rev.* **2009**, *38*, 1011-1026.
- [2] R. Sessoli, H.-L. Tsai, A. R. Schake, S. Wang, J. B. Vincent, K. Folting, D. Gatteschi, G. Christou and D. N. Hendrickson, *J. Am. Chem. Soc.* **1993**, *115*, 1804-1816.
- [3] R. Sessoli, D. Gatteschi, A. Caneschi and M. A. Novak, *Nature* **1993**, *365*, 141-143.
- [4] G. Christou, D. Gatteschi, D. N. Hendrickson and R. Sessoli, *MRS Bull.* **2000**, *25*, 66-71.
- [5] G. Christou, *Polyhedron* **2005**, *24*, 2065-2075.
- [6] R. Bagai, G. Christou, *Inorg. Chem.* **2007**, *46*, 10810-10818.
- [7] M. Soler, W. Wernsdorfer, K. A. Abboud, J. C. Huffman, E. R. Davidson, D. N. Hendrickson, G. Christou, *J. Am. Chem. Soc.* **2003**, *125*, 3576-3588.
- [8] H. J. Eppley, H.-L. Tsai, N. de Vries, K. Folting, G. Christou and D. N. Hendrickson, *J. Am. Chem. Soc.* **1995**, *117*, 301-317.
- [9] M. Soler, S. K. Chandra, D. Ruiz, E. R. Davidson, D. N. Hendrickson and G. Christou, *Chem. Commun.* **2000**, 2417-2418.
- [10] T. Kuroda-Sowa, M. Lam, A. L. Rheingold, C. Frommen, W. M. Reiff, M. Nakano, J. Yoo, A. L. Maniero, L. C. Brunel, G. Christou and D. N. Hendrickson, *Inorg. Chem.* **2001**, *40*, 6469-6480.
- [11] R. Basler, A. Sieber, G. Chaboussant, H.U. Gudel, N.E. Chakov, M. Soler, G. Christou, A. Desmedt, R. Lechner, *Inorg. Chem.* **2005**, *44*, 649-653.
- [12] N. E. Chakov, M. Soler, W. Wernsdorfer, K. A. Abboud and G. Christou, *Inorg. Chem.* **2005**, *44*, 5304-5321.
- [13] R. Bagai, G. Christou, *Inorg. Chem.* **2007**, *46*, 10810-10818.
- [14] N. Regnault, T. Jolicoeur, R. Sessoli, D. Gatteschi and M. Verdaguer, *Phys. Rev. B* **2002**, *66*, 054409-054414.

- [15] T. C. Stamatatos and G. Christou, *Philos. Trans. R. Soc. London*, **2008**, 366, 113-125.
- [16] R. A. Robinson, P. J. Brown, D. N. Argyriou, D. N. Hendrickson and S. M. J. Aubin, *J. Phys.: Condens. Matter*. **2000**, 12, 2805-2810.

Chapter 5

Conclusions and perspectives

In this thesis, the reaction mechanism of molecular cluster batteries (MCBs) was investigated by *in situ* XAFS (Chapter 2), NMR and cyclic voltammetry (Chapter 3), and *in situ* magnetic analyses (Chapter 4). The fundamental understanding of the reaction mechanism of MCBs is a key step to develop high-performance MCBs, in which a high capacity, rapid charging, and long life cycle can be achieved for real applications. Elucidations of structural and electronic-state changes of the molecular species in the battery reactions are also important in the fields of fundamental sciences, because their behavior in solid-state electrochemistry is probably different from that in solution electrochemistry. In this chapter, results documented in this thesis are summarized, and future studies on MCBs are suggested.

Discovery of super-reduced molecular clusters

In situ XAFS studies of the Mn₁₂ and PMo₁₂ MCBs have revealed the formation of super-reduced molecular clusters, such as eight-electron reduced [Mn₁₂]⁸⁻, and twenty-four-electron reduced [PMo₁₂]²⁷⁻ in the discharging processes, with reversible structural changes. These super-reduced molecular clusters in the solid-state electrochemistry of their battery reactions have been observed for the first time in this work. Note that they could not be obtained by conventional solution electrochemistry. These results show that the large capacity of the PMo₁₂ MCBs is caused by the twenty-four-electron reduction of Mo ions in PMo₁₂, while eight-electron reduction of Mn ions in Mn₁₂ can explain only a half of the whole capacity of the Mn₁₂ MCBs.

EDL effects in the Mn₁₂ MCBs

In the Mn₁₂ MCBs, the other half of the capacity cannot be explained by the multi-electron redox of the Mn ions in Mn₁₂. In Chapter 3, the origin of this

additional capacity was investigated by using cyclic voltammetry, and NMR analyses. The results suggested the formation of EDLs in the discharging processes, which were probably formed between the negatively charged carbon black electrodes and Li^+ ions trapped on the surface of Mn12. In fact, the value of this EDL capacitance corresponded to a half of the observed capacity. Combination of the EDL capacitance and the redox reactions is advantageous for realizing high capacity rechargeable batteries.

Difference between the Mn12 and PMo12 MCBs

The reaction mechanisms of Mn12 and PMo12 MCBs were demonstrated to be different from each other. In the former, the capacity is explained by a combination of the EDL capacitance, and the redox reactions. In the latter, only the redox reaction of PMo12 is involved in the battery reaction. This means that the contribution of the EDLs to the Mn12 MCBs is rather large, compared to that of the PMo12. From a structural point view, there is a significant difference between the two clusters. Namely, Mn12 has carboxylate ligands, while PMo12 is formed only by the metals and O^{2-} . As indicated in Chapter 3, trapping of Li ions between the molecular clusters and the carbon electrodes probably forms the EDLs, so that organic ligands in the Mn12 would play an important role in this supercapacitor effect.

Applications of *in situ* magnetic analyses

An *in situ* magnetic analysis method was developed to investigate the magnetic properties of the super-reduced $[\text{Mn}_{12}]^{8-}$ in the Mn12 MCBs. It is suggested that $[\text{Mn}_{12}]^{8-}$ possesses a high-spin state of $S = 14$, which is higher than that of $[\text{Mn}_{12}]^0$ ($S = 10$). This means that Mn12 species with a higher spin ground state can be prepared by solid-state electrochemistry. The change in the spin quantum numbers of the Mn ions, determined from these results, is consistent with the results from the Mn valence changes obtained by the XAFS. This kind of *in situ* magnetic measurement is a useful method to elucidate novel magnetic properties of metal complexes with unusual oxidation state obtained by a solid-state electrochemistry.

Perspectives on MCBs

Based on the reaction mechanisms of MCBs described in this thesis, the following strategies are proposed to develop MCBs with high capacity, rapid charging, and excellent cycle performance:

1. Stable molecular clusters including a large number of redox-active metal ions enable a rapid charging and long life cycle, as well as a high capacity, as the performance of the PMo₁₂ MCBs is better than that of the Mn₁₂ MCBs.

2. Organic ligands included molecular clusters enhance the EDL capacitance effects, resulting in an additional capacity.

3. To obtain a rapid charging and a large plateau voltage, it is necessary to develop effective/smooth electron transfers between the cluster molecules and the electrode, and quick Li ion diffusion. Nanohybridization between molecular clusters and single walled carbon nanotubes would be useful, since at present the cathodes are made by only mixing microcrystals of the molecular clusters and carbon black particles.

We are now at the point of realizing high-performance MCBs along these strategic paths. The author hopes that this thesis on the fundamental understanding of the reaction mechanisms of MCBs will be useful to develop them for practical applications.

Acknowledgements

First and foremost, this Ph.D. was accomplished by the generous funding from the Global-COE, and for that I am very grateful. This support from the G-COE project also allowed me to present the results of this research at a number of domestic and international conferences. Thanks go to the G-COE office, Mr. Kato and so on.

I am very grateful to my supervisor, Prof. K. Awaga, who picked me up three years ago from China and gave me this precious chance to study in his laboratory. He has taught me too many things to list here, and I thank him for his advice, patience and understanding. This three year experience in his group will benefit me the rest of my life.

I would like to thank my co-supervisor Assistant Prof. H. Yoshikawa. His constant guidance and invaluable discussions always motivate me to do my research. His wealth of scientific and social knowledge provided me a great learning experience. His exact teaching enabled me to complete my Ph.D. work.

I also acknowledge Prof. H. Shinohara and Prof. K. Tanaka, for their time and efforts to my dissertation and defense.

Much of this work has been achieved thanks to collaborators. I appreciate a support from Prof. T. Yokoyama, who pioneered the XAFS measurements and taught me how to measure and analyze XAFS data. I am grateful to Prof. S. Irlle and Mr. Y. Nishimoto for the theoretical studies.

I thank some members in Awaga laboratory, particularly Mr. S. Hamanaka for his help on synthesis of samples and *in situ* XAFS measurements, and Dr. S. Dalgleish for his help on English correction, and Mr. N. Kawasaki, Mr. Y. Kondo, Mr. Y. Miyoshi, Ms. Handa, ... also helped me a lot.

Finally, I would like to thank my family for their support of all my life choices and their love, which is a constant source of strength for everything I do. My parents have never limited my dreams. And my sister has and will always be a significant source of moral supports.

Main Publication

In-situ XAFS Studies of Mn₁₂ Molecular-Cluster Batteries: Super-Reduced Mn₁₂ Clusters in Solid-State Electrochemistry

H. Wang, S. Hamanaka, T. Yokoyama, H. Yoshikawa, and K. Awaga

Chem. Asian J. 6, 1074–1079 (2011)